TOLERANCE LEVEL DETERMINATION FOR AUTOMATED EPID-BASED DEEP INSPIRATION BREATH-HOLD (DIBH) INSTABILITY EVALUATION IN BREAST CANCER PATIENTS

APHISARA DEEHARING

A THESIS SUBMITTED IN PARTIAL FULFILLMENT
OF THE REQUIREMENTS FOR THE DEGREE OF
MASTER OF SCIENCE (MEDICAL PHYSICS)
FACULTY OF GRADUATE STUDIES
MAHIDOL UNIVERSITY
2020

Thesis
entitled

TOLERANCE LEVEL DETERMINATION FOR AUTOMATED EPID-BASED DEEP INSPIRATION BREATH-HOLD (DIBH) INSTABILITY EVALUATION IN BREAST CANCER PATIENTS

Aphisara Deeharing
....
Miss Aphisara Deeharing
Candidate

Puangpen T.
....
Puangpen Tangboonduangjit,
Ph.D. (Medical Radiation Physics)
Major advisor

....
Todsaporn Fuangrod,
Ph.D. (Electrical Engineering) (Ph.D. (Electrical Engineering))
Co-advisor

....
Prof. Patcharee Lertrit,
M.D., Ph.D. (Biochemistry)
Dean
Faculty of Graduate Studies
Mahidol University

Sawwanee Asavaphatiboon
....
Asst. Prof. Sawwanee Asavaphatiboon,
D.Eng. (Nuclear Engineering)
Program Director
Master of Science Program in Medical Physics
Faculty of Medicine Ramathibodi Hospital
Mahidol University

Thesis
entitled
TOLERANCE LEVEL DETERMINATION FOR AUTOMATED EPID-BASED DEEP INSPIRATION BREATH-HOLD (DIBH) INSTABILITY EVALUATION IN BREAST CANCER PATIENTS

was submitted to the Faculty of Graduate Studies, Mahidol University
for the degree of Master of Science(Medical Physics)
on
October 05, 2020

APHISARA DEEHARING
....
Miss Aphisara Deeharing
Candidate

Sornjarod Oonsiri
....
Sornjarod Oonsiri,
Ph.D. (Biomedical Engineering) (Ph.D. (Biomedical Engineering))
Chair

Puangpen T.
....
Puangpen Tangboonduangjit,
Ph.D. (Medical Radiation Physics)
Member

....
Todsaporn Fuangrod,
Ph.D. (Electrical Engineering) (Ph.D. (Electrical Engineering))
Member

....
Prof. Patcharee Lertrit,
M.D., Ph.D. (Biochemistry)
Dean
Faculty of Graduate Studies
Mahidol University

....
Prof. Piyamitr Sritara,
MD., FRCP, FACP, FRCP (T)
Dean
Faculty of Medicine Ramathibodi Hospital
Mahidol University

ACKNOWLEDGEMENTS

Firstly, I would like to express my very great appreciation to Dr.Todsaporn Fuangrod for his valuable and constructive suggestions during the planning and development of this research work. His willingness to give his time so generously has been very much appreciated.

I sincerely thank Assist. Prof. Chirapha Tannanonta for valuable advice, suggestion, and guidance in my thesis.

I would like to thank Dr. Puangpen Tangboonduangjit, my advisor, and Asst.Prof. Sawwanee Asavaphatiboon, Program Director Master of Science Program in Medical Physics Faculty of Medicine Ramathibodi Hospital for valuable advice and encouragement.

I would like to deeply thank my external committee, Dr. Sornjarod Oonsiri and Dr. Thiansin Liamsuwan.

I would also like to extend my thanks to the staff at Radiation Oncology Unit, Chulabhorn Hospital, for their help in offering me the resources.

I would like to thanks friend, Medical Physics student in Medical Physics School, Faculty of Medicine Ramathibodi Hospital for friendship and their help in studying in this course.

Finally, I wish to thank my parents for their support and encouragement throughout my study.

Aphisara Deeharing

TOLERANCE LEVEL DETERMINATION FOR AUTOMATED EPID-BASED DEEP INSPIRATION BREATH-HOLD (DIBH) INSTABILITY EVALUATION IN BREAST CANCER PATIENTS

APHISARA DEEHARING 6036158 RAMP/M

M.Sc.(MEDICAL PHYSICS)

THESIS ADVISORY COMMITTEE : PUANGPEN TANGBOONDUANGJIT, Ph.D., TODSAPORN FUANGROD, Ph.D. (Electrical Engineering)

ABSTRACT

Breast cancer is the most common cancer in women. Radiation therapy (RT) is the most recommended treatment to reduce local recurrence and improves the overall survival rate. However, RT has limitations regarding the patient's respiratory motion, especially in the left side breast. The irradiated field through the left side breast is projected near the heart, leading to cardiac morbidity and mortality. Currently, a deep inspiration breath-hold (DIBH) technique becomes standard respiratory motion management to reduce the cardiac dose during tangential field left breast radiotherapy. However, there is no current system to evaluate the patient's breath-hold capability towards DIBH accuracy in real-time. The cine images from an electronic portal imaging device (EPID) were acquired and analyzed to find the stability of the breath-hold during treatment delivery by using in-house MATLAB program. The Canny's edge detection is applied to find and track the lung depth, which represents the stability of the patient breath-hold. The system performance was tested from the three experimental setups with phantom to simulate the motion for test accuracy, reproducibility, and capability. For the clinical tests, there were randomly three patients for evaluating the breath-hold capability for multiple fractions during the treatment course. In addition, the tolerance level of breath-hold based on cardiac toxicity was determined using the dose calculation of various simulated organ motions using a RayStation system. For phantom studies, the maximum difference of accuracy test was -0.994 mm, the reproducibility showed a promising system, and the system can handle image blurring well (< 1mm maximum difference) but very sensitive to image noise (maximum difference was -73.2 mm). For clinical tests, the system was able to evaluate the patients' breath-hold capabilities corresponding to the amplitude setting from the treatment room. The tolerance level to switch from DIBH to free-breath (FB) delivery should be less than 11.00 mm in AP direction from the reference position. To sum up, the proposed system showed high accuracy (with less than a millimeter error) of detecting breath-hold capability that can be applied clinically.

KEY WORDS: DEEP INSPIRATION BREATH-HOLD, LEFT BREAST CANCER, RESPIRATORY MOTION, CINE IMAGE, IN HOUSE MATLAB

83 pages

การพัฒนาระบบการประเมินความสามารถการกลั้นหายใจระหว่างการฉายรังสีผู้ป่วยมะเร็งเต้านม โดยใช้อุปกรณ์รับภาพรังสีอิเล็กทรอนิกส์

TOLERANCE LEVEL DETERMINATION FOR AUTOMATED EPID-BASED DEEP INSPIRATION BREATH-HOLD (DIBH) INSTABILITY EVALUATION IN BREAST CANCER PATIENTS

อภิสรา ดีหะริง 6036158 RAMP/M

วท.ม.(ฟิสิกส์การแพทย์)

คณะกรรมการที่ปรึกษาวิทยานิพนธ์: พวงเพ็ญ ตั้งบุญดวงจิตร, Ph.D., ทศพร เฟื่องรอด, Ph.D. (Electrical Engineering)

บทคัดย่อ

มะเร็งเต้านมเป็นมะเร็งที่พบมากที่สุดในผู้หญิง การรักษาด้วยการฉายรังสีเป็นวิธีที่ได้รับการแนะนำเพื่อลดการกลับมาเป็นซ้ำ และช่วยเพิ่มอัตราการรอดชีวิต อย่างไรก็ตามการฉายรังสีมีข้อจำกัดเกี่ยวกับการหายใจของผู้ป่วยโดยเฉพาะที่เต้านมด้านซ้าย เนื่องจากรังสีที่ผ่านเต้านมด้านซ้ายเข้าใกล้หัวใจ ซึ่งนำไปสู่การเจ็บป่วย และการเสียชีวิตด้วยโรคหัวใจ ปัจจุบันเทคนิคการหายใจเข้าลึกแล้วกลั้นใจนิ่งขณะฉายรังสี กลายเป็นวิธีมาตรฐานในการจัดการการเคลื่อนไหวของระบบทางเดินหายใจ เพื่อลดปริมาณรังสีที่หัวใจได้รับในระหว่างการฉายรังสีบริเวณทรวงอกด้านซ้าย อย่างไรก็ตามเทคนิคดังกล่าวยังไม่มีระบบที่นำมาประเมินความถูกต้องของความสามารถในการกลั้นหายใจของผู้ป่วยในขณะฉายรังสี ในการศึกษานี้ภาพถ่ายขณะฉายรังสีจากอุปกรณ์รับภาพรังสีอิเล็กทรอนิกส์ถูกนำมาใช้วิเคราะห์ผลเพื่อหาความเสถียรของการกลั้นหายใจระหว่างการรักษาโดยการใช้โปรแกรมแมทแลป และอัลกอริทึมแคนนี่ในการตรวจจับลักษณะขอบเขตของภาพเพื่อหาระยะความลึกของปอดซึ่งแสดงถึงความเสถียรของการกลั้นหายใจของผู้ป่วย ทั้งนี้มีการทดสอบประสิทธิภาพของระบบสามด้านจากหุ่นจำลองเสมือนมนุษย์ ได้แก่ ความถูกต้อง ความสามารถในการทำซ้ำ และความสามารถในการวิเคราะห์ผล สำหรับการทดสอบทางคลินิกมีผู้ป่วยที่ได้รับการคัดเลือกแบบสุ่ม 3 รายเพื่อประเมินความสามารถในการกลั้นหายใจในระหว่างการรักษา นอกจากนี้มีการศึกษาการกำหนดระดับความทนต่อการกลั้นหายใจตามความเป็นพิษของหัวใจ โดยการคำนวณจากการจำลองการเคลื่อนไหวของอวัยวะในระยะต่างๆจากระบบวางแผนการรักษาเรย์เสิร์ช และเทียบกับปริมาณรังสีที่หัวใจได้รับ ผลการศึกษาประสิทธิภาพของระบบในหุ่นจำลองเสมือนมนุษย์ พบว่าความแตกต่างสูงสุดของการทดสอบความแม่นยำคือ -0.994 มม. และความสามารถในการทำซ้ำแสดงให้เห็นถึงแนวโน้มระบบที่ดีและระบบสามารถจัดการความเบลอของภาพได้ดี (ความแตกต่างสูงสุด <1 มม.) แต่ระบบยังคงไวต่อสัญญาณรบกวนของภาพมาก (ความแตกต่างสูงสุดคือ -73.2 มม.) สำหรับการทดสอบทางคลินิกระบบสามารถประเมินความสามารถในการกลั้นหายใจของผู้ป่วยที่สอดคล้องกับการตั้งค่าแอมพลิจูดจากห้องฉายรังสี ระดับความอดทนในการเปลี่ยนจากเทคนิคกลั้นใจนิ่งเป็นการแบบหายใจแบบปกติควรน้อยกว่า 11.00 มม. ในทิศทางหน้าหลังจากตำแหน่งอ้างอิง สรุปได้ว่าระบบที่นำเสนอแสดงความแม่นยำสูง (โดยมีข้อผิดพลาดน้อยกว่ามิลลิเมตร) ในการตรวจวัดความสามารถในการกลั้นหายใจที่สามารถนำไปใช้งานในทางการแพทย์ได้

83 หน้า

CONTENTS

LIST OF TABLES

LIST OF FIGURES

LIST OF FIGURES (cont.)

LIST OF FIGURES (cont.)

LIST OF FIGURES (cont.)

LIST OF FIGURES (cont.)

LIST OF ABBREVIATIONS

Abbreviations	**Term**
4DCT	Four-dimensional computed tomography
AAPM	American Association of Physicists in Medicine
ABC	Active breathing coordinator
ABS	American brachytherapy society
AP	Anteroposterior
APBI	Accelerated partial breast irradiation
a-Si	Amorphous silicon
ASTRO	American Society for Radiation Oncology
Ax	Axilla nodes
BEV	Beam's-eye-view
BH	Breath-hold
BT	Brachytherapy
CA	Central axis
CBD	Central breast distance
CBESD	Central Beam Edge to Skin Distance
CCD	Charge-coupled-device
CCD	Crania caudal distance
CFD	Central flash distance
cine	Cinematographic
CIW	Central irradiated width
CLD	Central lung distance
CT	Computed tomography
DIBH	Deep inspiration breath-hold
DNA	Deoxyribonucleic acid
DRR	Digitally reconstructed radiograph
DVH	Dose-volume histograms

LIST OF ABBREVIATIONS (cont.)

EBRT	External beam radiation therapy
EPID	Electronic portal imaging device
FB	Free breath
FL	Field length
FW	Field width
Gy	Gray
HDR	High-dose-rate
ICM	Inferior central margin
ICW	Internal chest wall
IGRT	Image-guided radiotherapy
IMN	Internal mammary nodes
kV	Kilovoltage
LA	Lung area
LAD	Left anterior descending coronary artery
LDR	Low-dose-rate
LoG	Laplacian of Gaussian
LPO	Left posterior oblique field
MHD	Mean heart dose
MLC	Multileaf collimator
MV	Megavoltage
OAR	Organs at Risk
OBI	On-board imager
PSF	Point spread function
QA	Quality assurance
QOL	Quality of life
QUANTEC	Quantitative Analyses of Normal Tissue Effects in the Clinic
RAO	Right anterior oblique field

LIST OF ABBREVIATIONS (cont.)

RPM	Real-time position management system
RT	Radiotherapy
RTOG	Radiation therapy oncology group
RTWM	Full range of thoracic wall motion
SCV	Supraclavicular fossa
SDD	Source-detector distances
SPC	Supraclavicular
TV	Target volumes
VCU	Virginia commonwealth university
WBRT	Whole-breast radiation therapy

CHAPTER I
INTRODUCTION AND LITERATURE REVIEWS

In women, breast cancer is the most common cancer, and also the foremost cause of cancer death, approximately 15.0% [1]. For early-stage breast cancer, surgery with adjuvant radiation therapy is the most recommended treatment to reduce the local recurrence and improves the overall survival rate [2]. When compared with surgery alone, the rate of mortality is a reduction in the case of radiation therapy after surgery [3]. However, respiratory motion is a significant challenging problem in breast radiotherapy, mainly on the left side due to near heart and left anterior descending coronary artery (LAD). Furthermore, the risk of subsequent has been reported to induce relevant cardiac death that is assessed from mean heart dose (MHD) [4-6]. After irradiation in breast cancer showed that the rates of major coronary events are increased at 7.4% per Gray (Gy) of MHD [5]. Currently, deep inspiration breath-hold (DIBH) is used in radiotherapy with left-sided breast cancer to reduce the cardiac and LAD dose in numerous centers. In this technique, patients hold their breath while radiation is delivered, the diaphragm descends, and the heart moves away from the chest wall [7-9]. Though there is a significant reduction of heart dose, this technique is also required monitoring the stability of DIBH during treatment. Besides, several methods have been developed to monitoring the stability of DIBH, such as using a respiratory gating system, electronic portal imaging device (EPID), and surface guided radiotherapy. In this study, the cinematographic image (cine) is selected for DIBH monitoring because it does not add the dose to the patient. Then, it can measure geometrical setup errors in Beam's-Eye-View (BEV) according to the actual field [10-12]. As a result, an in-house automated DIBH stability evaluation tool from cine was developed by using MATLAB software. Thus, the tolerance level of breath-hold capability quantified based on cardiac toxicity was determined to be confident that it can handle in the clinical criteria for using DIBH in the next treatment fraction.

1.1 Radiotherapy in breast cancer

Radiotherapy (RT) is an essential component treatment of the patient with early and local breast cancer by using high energy ionizing radiation such as photon, electron, and proton to annihilate cancer cells. The radiation will destroy cancer by damaging the deoxyribonucleic acid (DNA). In addition, several studies indicated that RT after surgery has a low-risk recurrence that can reduce the local recurrence after surgery by approximately 20% and breast cancer mortality by 5%. Also, reduce the sign from cancer, which is spread to other parts of the body or metastatic breast cancer [7, 13-15]. Breast RT is consists of internal radiation or brachytherapy and external beam radiation or teletherapy.

Furthermore, external beam radiation therapy (EBRT) is the most typical type of radiotherapy used which the delivery of radiation from a treatment machine outside the body at some distance from the treatment area. That may be given as partial breast irradiation, in which radiation is delivered directly to the tumor area shown in Figure 1.1(a). Internal radiotherapy or brachytherapy is treated by a radioactive source in which the device containing radioactive seeds or pellets is put inside the breast tissue for a short time in the area where cancer had been removed, as displayed in Figure 1.1(b) [16].

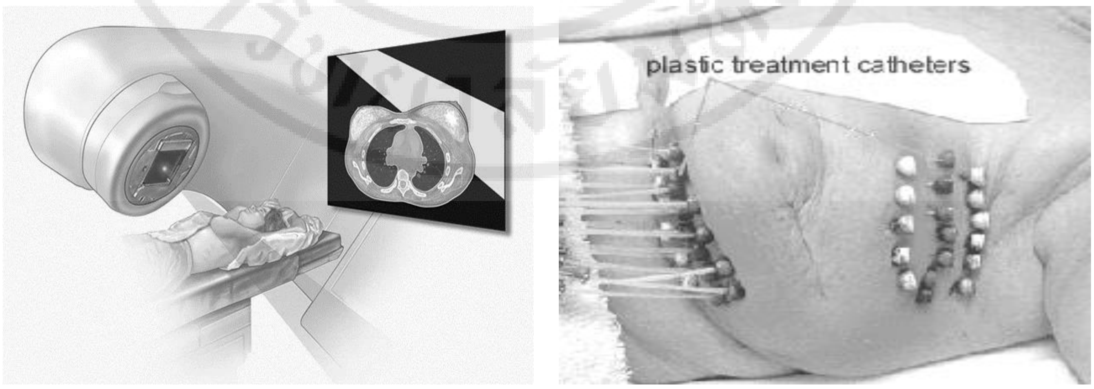

(a) (b)

Figure 1.1 Radiotherapy for breast cancer, (a) external-beam radiation therapy, (b) Internal radiation therapy or brachytherapy [17][18].

1.1.1 Internal radiation (brachytherapy) for breast cancer

Internal radiation therapy or brachytherapy (BT) is a type of treatment by using radiation which radiation source such as seed is put inside the body near a region of cancer. BT was used to cure many types of cancers, for example, head and neck, breast, uterus, cervix, and prostate. The advantage is to deliver the high radiation dose to the tumor while surrounding healthy tissue receives less dose because of characteristics like rapid fall off that radiation dose not provide so far from the target. Also, three types of BT consist of low-dose-rate (LDR), high-dose-rate (HDR), and permanent implants. For LDR, the radiation source stays in place for one to seven days. The catheter or applicator beside the patient needs to admit to the hospital. After treatment is finished, the doctor will remove the radiation source. For HDR, the radiation source is placed around 10 to 20 minutes at a time and then taken out. The plan of the procedure depends on the type of cancer. Sometime, the patient may have treatment twice a day for two to five days or once a week for two to five weeks. Moreover, permanent implants, the implants always stay in the body, but the radiation gets weaker each day [15, 19].

For breast cancer, BT has used for most of the 20th century. In history, that was used to treat the lumpectomy cavity as a boost for unselected tumors after EBRT. The procedure of BT is starting after surgery for removing the tumor of breast cancer. Then a doctor will place a radiation-delivery device near the tumor site and load the radioactive source into the device for short periods over the course depend on treatment planning. The applicator is interstitial needle implants that are various types such as Mammosite balloon and Contoura multi-lumen balloon. Presently, there have several techniques for BT. The first, interstitial brachytherapy. The second, using the balloons. The last, hybrid brachytherapy devices [19].

Nowadays, many centers have adapted using accelerated partial breast irradiation (APBI). The advantage is the high total doses and poor cosmetic results. When compared with EBRT, brachytherapy can be completed in a 4 to 5-day treatment course. However, The American Brachytherapy Society (ABS) identifies which EBRT is the standard radiation modality of treatment the breast cancer. In the present, BT is an alternative that is investigated [15, 20].

1.1.2 External beam radiation for breast cancer

In general, EBRT was given around one month after surgery or after surgical wounds heal. It may be combined with chemotherapy [21]. The radiation should be given the whole breast that maximizing coverage of tumor and breast, whereas minimizing exposure of the heart and ipsilateral lung. Also, radiation is delivered directly to the tumor area from opposite directions as partial breast irradiation or calls tangential fields and maybe compensating with wedges if the nearby lymph nodes are also being treated, as shown in Figure 1.2. The advantages of EBRT for breast cancer patients is a fast, painless, noninvasive technique, and outpatient procedure. Then the targeted of EBRT is the treatment area only that difference from chemotherapy, which circulates throughout the body. Last, there is no risk of radioactivity [15].

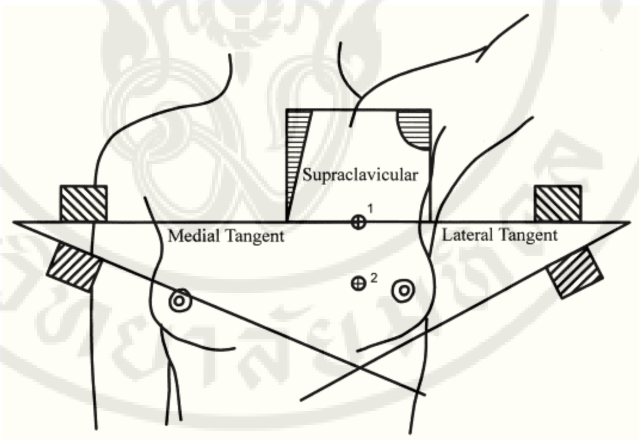

Figure 1.2 AP view of the single isocenter of three field setup. Point 1 is the isocenter, and point 2 indicates the center of the tangential breast fields [22].

1.1.2.1 Dose solutions

In breast cancer planning, commonly use photon energy 6 megavoltage (MV). Nevertheless, in the patient who increased breast volume and separation should be using higher energies such as 10 MV that may produce better homogeneity due to increasing skin sparing. Also, it should ensure that superficial cavity wall margins and scars of reconstructed breasts receive an adequate dose. Moreover, using computed tomography (CT) data to correct lung density, then beams have been optimized and achieved a homogeneous 3D dose distribution. In the left side breast, the dose may be increased cardiac mortality. Recently, using a multileaf collimator (MLC) to shield the heart and LAD illustrated in Figure 1.3. Furthermore, the respiratory motion may affect the dosimetry of dynamic MLC that can use the respiratory gating system and DIBH to cease respiration. Additionally, image-guided radiotherapy (IGRT) and immobilization are also necessary that could help to reduce both inter- and intra-fraction motion [13, 23].

Figure 1.3 Sagittal digitally reconstructed radiograph (DRR) with segmented fields of cardiac shielding [13].

1.1.2.2 Dose-fractionation

Commonly using conventional fraction was on an outpatient basis five days a week, over 5 to 7 weeks, based on the particular situation. The total dose is 50 Gy in 25 fractions or five weeks (2 Gy per fraction). Sometimes 5 to 7 weeks may be stressful for some women instance who lived far away from a treatment center. Thus, several researchers studied increasing doses per fraction but the equal total radiation dose. The accelerated or hypofractionated radiation schedule puts the same radiation dose into a 3 to 5-week program. In 2018, the American Society for Radiation Oncology (ASTRO) modernized guidelines about whole-breast radiation therapy (WBRT). The instruction shows that most women diagnosed with breast cancer who will have radiation therapy after lumpectomy should be treated with accelerated WBRT as the standard of precaution. The chosen hypofractionated dose schedule is 40 Gy in 15 fractions or 42.5 Gy in 16 fractions [21].

1.1.2.3 The organ at risk and radiation tolerance dose

Chest wall and regional lymphatic have nearby importance organs such as heart, coronary arteries, and lung. Besides, there should consider a contralateral breast, contralateral lung, esophagus, brachial plexus, and spinal cord. Further, the optimal delineation of organs at Risk (OAR) carries substantial importance due to its influence on treatment planning evaluation. Poor delineation of OAR results in the misunderstanding of dose-volume histograms (DVH) [15].

DVH is a histogram relating to radiation dose on the x-axis and percent volume of the interesting structure on the y-axis, as shown in Figure 1.4. DVH is generally used as a plan evaluation tool, and compared radiation dose from different plans. The shape and area under the curve are used to ensure that the target is adequately covered with dose and dose to critical structures is in acceptable limits. Also, the beginning of 3D planning is probable to describe the dose certain to a volume of tissue and to correlate with acute and late complication effects that usual description is in the form of a DVH [13, 15, 24].

Therefore, dose constraints are derived primarily from the Radiation Therapy Oncology Group (RTOG) protocols, and the Quantitative Analyses of Normal Tissue Effects in the Clinic (QUANTEC). From RTOG, The primary dose constraint was to cover 95.0% of the target with 95.0% of the prescribed dose for the chest wall or breast, and the dose constraints for target volumes (TV) and OAR are instituted in Table 1.1 and Table 1.2 [13, 15, 24].

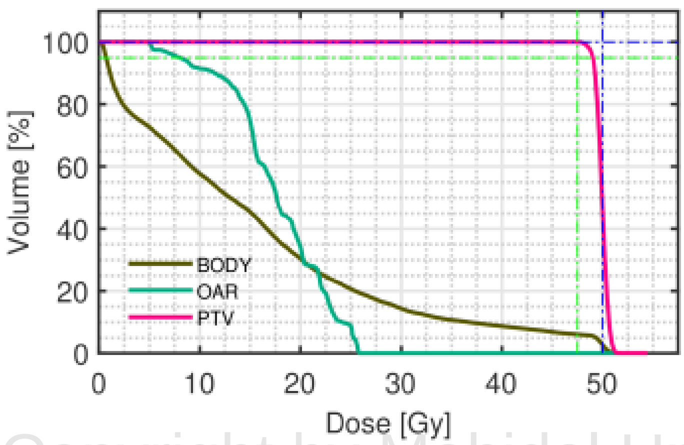

Figure 1.4 DVHs graph for the static case. The x- and y-axis represent to radiation dose and percent volume of the interesting structure, respectively [25].

For dose-volume constraints in heart, RTOG protocols have defined heart dose constraint for left-sided breast cancer as V20Gy less than 5%, V10Gy less than 3%, and MHD of 4 Gy. Besides, the University of Michigan defined the dose-volume constraint of LAD as a maximum dose of less than 15 Gy and a mean dose of less than 5 Gy [15].

Table 1. 1 Dose constraints for TV and OAR in the breast/chest wall [24].

Target volume	Dose Constraint
chest wall	$V90 \geq 90\%$ [a]
Breast	$V100 \geq 90.0\%$
	$V95 \geq 95.0\%$
	$V105 \leq 40.0\%$
	$V110 \leq 10.0\%$
Internal Mammary Nodes (IMN)	$V80 \geq 100.0\%$
Supraclavicular Fossa (SCV)	$V90 \geq 90.0\%$
Axilla nodes (Ax)	$V90 \geq 90.0\%$
Whole lung	$V20Gy \leq 25\%$ [b]
	$V30Gy \leq 20\%$

[a]Vx mentions to the volume of the target volume receiving x% of the dose (for instance, $V95 \geq 95.0\%$ means that greater than 95.0% of the volume was covered by 95.0% of the prescription dose).

[b]VxGy mentions to the volume of the target volume receiving × Gy (for example, $V20Gy \leq 25.0\%$ means that less than 25.0% of the volume was covered by 20 Gy).

Table 1. 2 Summary of dose constraints for OAR used in protocols and published studies.

	Ipsilateral lung	Heart	Esophagus	Contralateral breast	Brachial plexus
RTOG [26]	RTOG 1005[A]	RTOG 1005[A]	RTOG 0623	RTOG 1005[a]	RTOG 0522
			RTOG 0617		Maximum dose 60 Gy
	Ideal	Ideal	Mean dose 34 Gy,	Ideal	RTOG 0619
	V20Gy ≤ 15.0%	V20Gy ≤ 5.0%	60 Gy to 10 cm	Dmax ≤ 3 Gy	Maximum dose 66 Gy
	V10Gy ≤ 35.0%	V10Gy ≤ 30.0%			V60 Gy ≤ 5.0%
	V5Gy ≤ 50.0%	Mean dose ≤ 4 Gy			
	Acceptable	Acceptable		Acceptable	
	V20Gy ≤ 20.0%	V25Gy ≤ 5.0%		Dmax ≤ 3.3 Gy	
	V10Gy ≤ 40.0%	V10Gy ≤ 30.0%			
	V5Gy ≤ 55.0%	Mean dose ≤ 5 Gy			
VUC[B] [27]	V20Gy ≤ 10.0%	V30Gy ≤ 3.0%	V30 ≤ 0	V2.5 ≤ 0	NS
	V5Gy ≤ 30.0%	V20Gy ≤ 10.0%			
	V0Gy ≤ 50.0%	V5Gy ≤ 30.0%			
		V5Gy ≤ 50.0%			

[A]breast tangents only; [b]breast tangents+regional nodes.

[B]VCU Virginia Commonwealth University; NS not stated

1.2 The respiratory motion-related to cardiotoxicity in breast RT

Intra-fraction motion is the motion occurring during the treatment that is related to many factors, such as respiratory, skeletal, muscular, cardiac, and patient movements. Moreover, the respiratory affects all tumor sites in the thorax and abdomen region, such as the breast, lung, and liver [23, 28].

The regular respiratory rate for healthy adults is between 12 and 20 breaths per minute. Also, Quetelet (1842) and Hutchinson (1850) investigated the pattern of breathing observed in adults 300 and 1714 subjects, respectively. These data indicate an extensive frequency range between 6 and 31 breaths per minute, correspondingly. From the data confirm that the human has difference breathing cycle. Therefore, respiratory rates can change based on many factors, for instance, anxiety, fever, heart problems, and obstructive sleep apnea [29].

Accordingly, respiratory motion is one of the main concerns during breast RT. The respiratory motion problem may occur from the simulation until the radiation treatment process. Jensen, et al (2017) studied the displacement of the baseline at the end of each treatment session in breast cancer, as in Figure 1.5, found that the largest was close to 8 mm and 17 out of 357 (5%) larger than 5 mm [30].

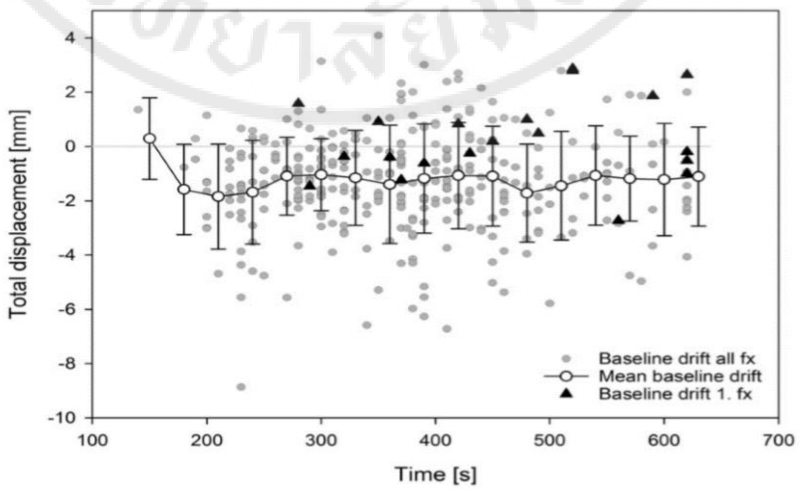

Figure 1.5 The baseline displacement at the end of the treatment session. Solid circles and solid triangles show the baseline drift for all patients, and the total baseline drift of each patient at the first fraction, respectably [30].

As indicated by Tezcanli's research (2011), a study comparing the radiation dose and volume changes during the breathing cycle exposed treatment planning deprived of breath control. That was not capable of compensating the heart and its components volume-dose changes then established that the respiratory organ movement had to be careful when planning treatment. Also, It is significant to mention that respiratory motion is one of the potential factors of error in radiotherapy [31].

Furthermore, RT for breast cancer frequently involves related exposure doses of the heart, which heart injury may become evident as acute or late toxicity. For acute toxicity, pericarditis is often transient but may be chronic. Late toxicity contains congestive heart failure, ischemic heart disease, myocardial infarction, coronary artery disease, and coronary revascularization. In addition, late toxicity expresses from months to decades after RT and can lead to cardiac morbidity or mortality [5, 8, 15, 32].

Besides, the most topical update from the Early Breast Cancer Trialists' Collaborative Group showed a risk of mortality from heart disease increased by 30% that was detected within 10-years after RT. Previous studies have assessed MHD as a measure of radiation exposure presented that MHD was a better predictor for major coronary events than the mean dose to LAD [4, 5]. Women treated for left breast had significantly higher rates of major coronary events than women treated for the right breast. Darby's study showed that the average of MHD was 6.6 Gy for women with the left-sided breast, 2.9 Gy for those with the right-sided breast. Also, the rate of major coronary events was 7.4% per Gy of MHD, as showed in Figure 1.6, with no apparent threshold lower, in which there was no risk [5].

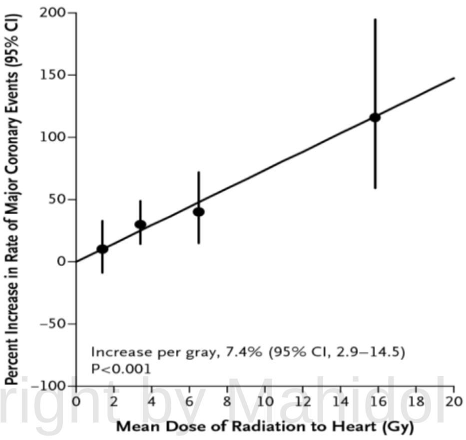

Figure 1.6 Rate of major coronary events according to MHD, as compared with the estimated rate without radiation exposure to the heart [5].

Moreover, QUANTEC guidelines state for partial heart irradiation is V25Gy <10% that will be associated with a <1% probability of cardiac mortality in long-term follow-up after RT approximately 15 years [6, 15]. Most of the research and development to date has been focused on accounting for respiratory motion. The methods are used for the respiratory motion management in radiation oncology consists of the DIBH technique, motion-encompassing technique, forced shallow-breathing technique, and respiratory-gated technique [28].

1.3 DIBH techniques for breast radiation therapy

In left side breast cancer, cardiac morbidity has been the primary concern in WBRT due to radiation exposure of cardiac tissues. DIBH is one recognized method of reduction of cardiac dose with the aid of the decline of long-term side effects [7-9]. In 1987, DIBH was used for reducing the respiratory impact in a part of the lung RT. Besides, DIBH was discussed more than ten years in the American Association of Physicists in Medicine (AAPM) task group 76 report but still not the standard in many clinics due to challenges associate with its implementation. Which techniques, patients hold their breath during radiation delivery. The air is drawn into the thoracic cavity, then diaphragm contract, and descends. Thus, the heart being pushed down and away from the radiation fields. Correspond with Comsa's study (2014), informed maximum linear distances of heart inside tangential breast fields was 1.6 cm for free breath (FB) and 0.4 cm for DIBH [33]. The advantages of DIBH techniques besides separated the heart from the target, still allowing a high dose to be given at the chest wall and breast tissue while the heart dose is reduced [7-9].

Several studies have established the MHD decrease of 37%-75% when using the DIBH technique also has reported reductions in several additional dose-volume metrics, as presented in Table 1. 3. Thus, the outcomes have been confirmed a more massive reduction in heart and LAD dose but a smaller reduction in lung dose [7, 8, 34]. Furthermore, the DIBH techniques for breast RT can divide into four sessions from the AAPM annual meeting in 2016. That involves active breathing control, spirometric motion management, self-held breath control with respiratory monitoring and feedback guidance, and 3D surface image-guided.

Table 1. 3 Overview of DIBH studies that include MHD and dose-volume.

Observers	Dose parameter	techniques			Prescribe dose
		FB	DIBH	p-value	
	Heart V20 (%)	7.82	2.33	<0.0001	
	Heart V40 (%)	3.44	0.3	<0.0001	
Nissen [7]	Mean heart dose (Gy)	5.18	2.69	<0.0001	50Gy/25fx
	lung V20 (%)				
	Periclavicular field	29.65	24.85	0.001	
	No periclavicular field	16.54	14.9	0.0368	
Mast [34]	Mean heart dose (Gy)	3.3	1.8	<0.01	42.56/16fx
	Heart V10 (%)	6	0.9	<0.01	
Comsa [33]	Heart V30 (%)	2	0.04	<0.01	50Gy/25fx
	Mean heart dose (Gy)	3.05	1.16	<0.01	
Czerems-	Heart V20 (%)	3.31	0.28	<0.001	
zynska [35]	Mean heart dose (Gy)	2.57	1.06	<0.001	39.9/15fx
	Left lung V20 (%)	13.06	11.35	0.001	
	Mean heart dose (Gy)	1.79	1.04	<0.001	
Bartlett [36]	ipsilateral lung (Gy)	3.9	4	0.762	40Gy/15fx
	Whole lung (Gy)	1.9	2	0.374	
Bartlett [37]	Mean heart dose (Gy)	0.7	0.4	<0.001	40Gy/15fx
	Heart V25 (%)	8.1	2.4	<0.001	50.4Gy
Sung [8]	Mean heart dose (Gy)	5.9	3	<0.001	/28 fx
	Left lung V25 (%)	16.7	15.7	0.19	
Hjelstuen	Heart V25 (%)	6.7	1.2	<0.001	
[38]	Mean heart dose (Gy)	6.2	3.1	<0.001	50Gy/25fx
	ipsilateral lung V25 (%)	44.5	32.7	<0.001	
Bruzzaniti [9]	Mean heart dose (Gy)	1.68	1.24	0.0106	50Gy/25fx

1.3.1 The Active Breathing Coordinator (ABC)

Active Breathing Coordinator™ device (ABC; Elekta, Stockholm, Sweden) was designed and the prototype tested at William Beaumont Hospital. The component consists of the ABC control module, patient respiratory system, patient control switch, and computer or control software. The patient breaths through a snorkel then a spirometer measures the resulting of airflow that is displayed on a monitor, and the breath-hold (BH) is automatically achieved when the volume of air inhaled exceeds a preset threshold by inflating a balloon valve that stops the airflow. That has limitations by patient compliance, the cost of acquisition, and maintenance equipment. Also, the nose clip used in DIBH may affect claustrophobic [14, 28, 39, 40]. A research article by Nissen (2013) evaluated the effect of DIBH on target coverage and dose to OAR in patients of breast cancer. The results showed a significant reduction in the heart V20Gy from 7.8% to 2.3% and the MHD from 5.2 to 2.7 Gy. Nevertheless, the lung dose showed a small reduction V20Gy from 16.5% to 14.9 % [7]. According to Mast (2013), the result is confirmed that the DIBH can reduce the dose in the heart and the LAD. The MHD was decreased from 2.7 Gy to 1.5 Gy for the IMRT technique and from 3.3 Gy to 1.8 Gy for the three-dimensional conformal radiotherapy (3D-CRT) technique, and then the mean LAD dose was reduced from 14.9 Gy to 6.7 Gy for the IMRT technique and from 18.9 Gy to 9.6 Gy for 3D-CRT technique [34].

1.3.2 Self-held breath control with respiratory monitoring

In this technique, the patients voluntarily breathed into a set of thresholds. Also, the real-time position management system (RPM; Varian Medical Systems, Palo Alto, CA) is an external gating system where both amplitude and phase gating are permitted. The RPM consists of an infrared tracking camera, marker block, and workstation. It is used to senses the breathing motion by tracking this pair of reflective markers on the patient's anterior abdominal surface and monitored by a charge-coupled-device (CCD) video camera mounted on the treatment room wall as demonstrated in Figure 1.7 [15]. In the treatment process, the patients hold their breath using audio coaching from therapists and visual feedback from goggles. The beam will be on when a green band is within a blue band, as shown in Figure 1.8, that the respiratory trace was exported from the CT simulation process [8, 9]. Besides, some study is monitoring the stability of DIBH from lasers and light field by the camera from the treatment room, including to MV cine mode during treatment [40].

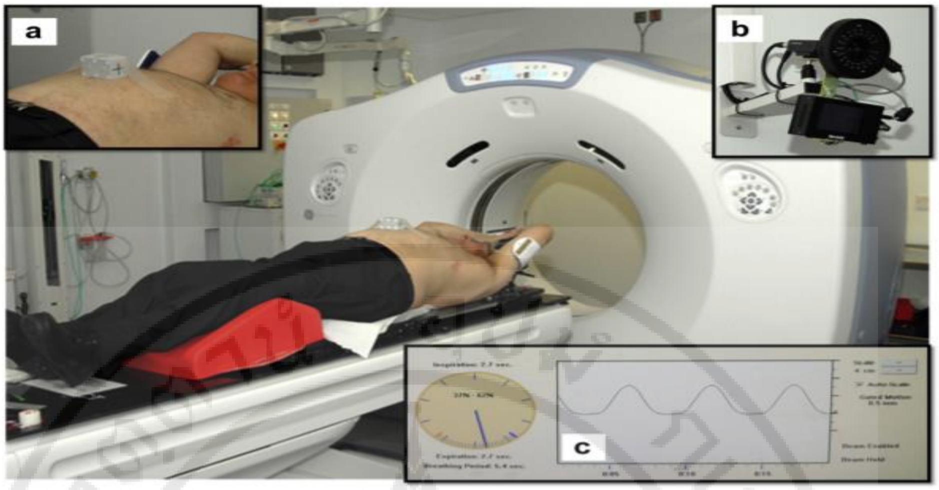

Figure 1.7 Four-dimensional computed tomography (4DCT): patient supine on a couch: (a) reflective marker placed on the chest wall, (b) infrared-sensor and camera, (c) graphical representation of respiratory cycle from Varian RPM system [41].

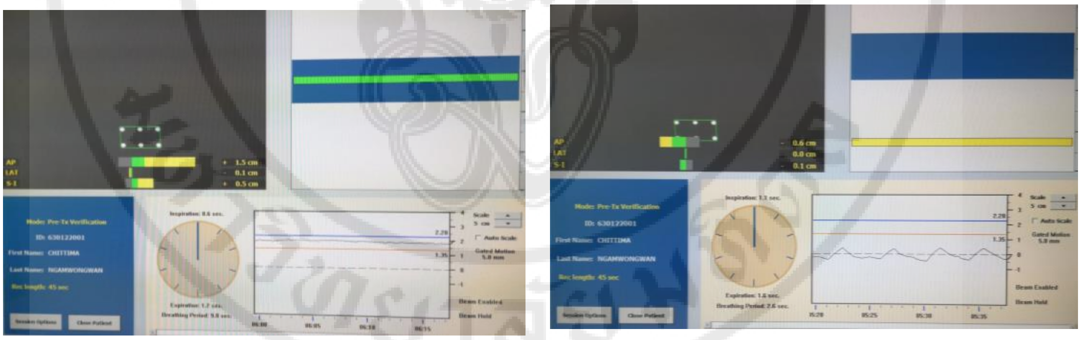

(a) (b)

Figure 1.8 From the treatment room, (a) the radiation will be on when the patient holds the breath in setting limits, and (b) the radiation will be stopped when the patient breath hold out offsetting limits by the radiation therapist.

The benefits are comfortable for the patient, easy, and reproducible. Also, from the UK Heart Spare study established a low-cost alternative using the voluntary DIBH. Conversely, this method is not yet in widespread use, even though interest is increasing [39, 42]. Besides, concerning voluntary DIBH about reproducibility is frequently questioned. The data for voluntary DIBH of left side breast confirmed dosimetric advantages [36, 37, 43] and good reproducibility [14, 39, 44]. In 2013, Bartlett et al., have compared the voluntary DIBH and DIBH with ABC in patients who receive left breast RT, as presented in Figure 1.9. The comparison was made in terms of normal-tissue sparing, positional reproducibility, and feasibility of delivery. Their results show no significant difference in terms of healthy tissue sparing. However, the patients and radiation therapists prefer the voluntary DIBH in terms of positional reproducibility because of taking less time to deliver, being more comfortable, and also cheaper than DIBH with ABC [14].

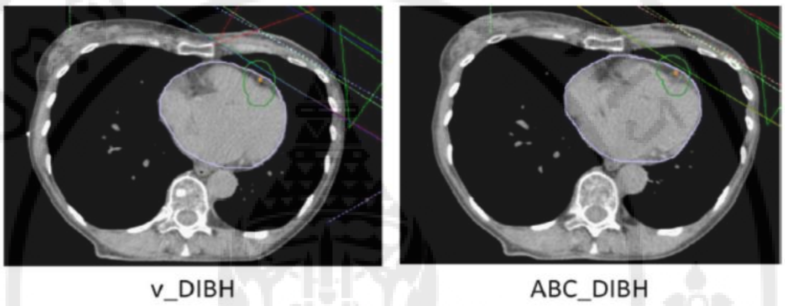

Figure 1.9 Axial CT slices of a patient taken during voluntary DIBH (v_DIBH) and DIBH with ABC (ABC_DIBH) [14].

In 2014, Bartlett compared the cardiac dosimetry for the supine voluntary DIBH and FB prone techniques in the large left breast. The results demonstrate that the voluntary DIBH offered better cardiac sparing and a more favorable reproducibility profile than FB prone. The cardiac doses for both techniques were low, which was 0.4 Gy for supine voluntary DIBH and was 0.7 Gy for FB prone. However, the prone position is difficult to set for several reasons, including the instability of breast and subcutaneous tissue, and the fact that target and organ as risk dosimetry is optimized by rotation of the patient to the treated side [37]. Then, Sung, et al presented a significant reduction in the heart V25Gy, MHD, mean LAD dose when comparing FB and DIBH, from 8.1% to 2.4 %, from 5.9 Gy to 3.0 Gy, and from 26.3 Gy to 13.8 Gy, respectively. That confirmed DIBH can reduce cardiac and LAD dose when comparison with FB. However, V25% of the left lung that no significant reduction as confirmations in Figure 1.10 shown DVH in each organ at risk consists of heart, LAD, and left lung comparing among FB, EIBH, and DIBH plans for the same patient and planning target volume [8].

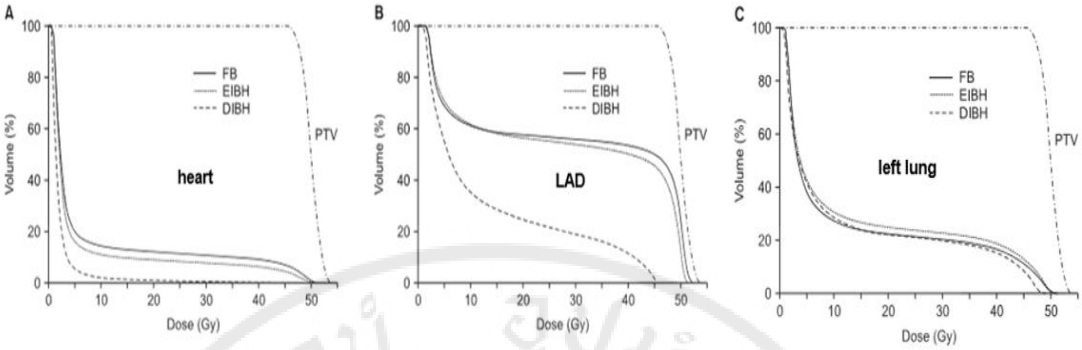

Figure 1.10 The dose-volume histogram in each organ at risk [8]**.**

In 2016, Bartlett also evaluated the feasibility and heart-sparing ability of the voluntary DIBH technique in a multicenter setting. When Compare between voluntary DIBH and FB plan, found that a substantial reduction in MHD and no significant difference in mean lung doses. The dosimetric benefits of voluntary DIBH compared to FB showed that the MHD was reduced from 1.79 Gy to 1.04 Gy for FB and voluntary DIBH, respectively. The mean LAD was decreased from 11.9 Gy with FB to 5.3 Gy with voluntary DIBH. The ipsilateral and whole lung was being reduced from 4.0 Gy to 3.9 Gy and from 2.0 Gy to 1.9 Gy for FB and voluntary DIBH, respectively [36].

In a study by Tamburella (2017), the DVH of voluntary DIBH and FB were analyzed. The dosimetric comparison shows that the PTV coverage is the same both of FB and DIBH then the significant reduction dose at OAR, such as MHD from 3.2 Gy to 1.2 Gy and V20 of cardiac from 1.5% to 0.2% [43]. Besides, in the view of Estoesta et al, studied a comparison between patients of left-sided breast radiotherapy with voluntary DIBH and FB techniques. They concluded that the voluntary DIBH technique is safe, no additional costs, easily implemented, and noninvasive procedure. Also, highly accepted by patients and staff and no increase in daily treatment time [39]. Conversely, the estimated risk of secondary cancer was the same both of FB and DIBH [40].

1.3.3 3D surface image guided based DIBH clinical implementation

In general, the commercial video-based motion management solutions or the 3D optical surface imaging are consist of the AlignRT system (Vision RT Ltd., London, UK) and C-RAD Catalyst (C-RAD Co., Sweden). Both 3D surface imaging was used in breast cancer radiotherapy in many centers that were used for real-time patient motion monitoring and prove the accuracy of patient positioning monitoring. The system noninvasive and non-ionizing radiation-based because AlignRT uses the infrared light, but C-RAD uses a scanning laser. Nevertheless, the limitations are the position of the target where it is deep that can lead to a lack of correlation with the surface and surfaces that easy to movement, such as the abdomen. Also, cost is a disadvantage.

Additionally, Betgen, et al (2013) studied to quantify set up uncertainties during voluntary DIBH of RT in the left breast by using the AlignRT system, from the study showed that patients could perform a very stable and reproducible within a treatment fraction. For inter-fraction, after setup correction in systematic error was 0.09-0.14 cm, and the random error was between 0.2-0.22 cm, respectively. For intra-fraction systematic and random were 0.04 cm in all directions and 0.09-0.14 cm, correspondingly [44].

1.4 Image-guided radiotherapy (IGRT) for breast RT

IGRT has enlarged importance in clinical use, which demanding accurate and precise localization of both target and surrounding tissues during treatment that was used to reduce setup errors from positioning and organ motion immediately before or during treatment. Furthermore, the retrospective review by Claire et al, shows that IGRT can help decrease cardiac irradiation and potentially reduce long-term complications in patients with left-sided breast cancer. After treatment, follow up at three months found that the IGRT group found less fatigue. Then follow up at 26 months, the IGRT group also had a better quality of life (QOL) score than another group [45]. Several researchers have studied the IGRT for breast cancer. Formerly, conventional port films were used in the verification process. Additionally, that was inspired by the idea of EPID systems combined into the gantry. EPID became popular with the use of since the 1990s, which has qualified a more precise and safer treatment [15].

The main groups of IGRT technologies include gantry-mounted, room-mounted, and non-ionizing systems [15]. IGRT based on gantry-mounted is more frequent use both planar MV and kilovoltage (kV) imaging also CBCT for full 3D visualization of the patient anatomy [43, 46]. IGRT based on non-ionizing imaging has been demonstrated with optical imaging such as Align RT [35, 44]. In this study, the description of IGRT used the application for the verification process. While the patient is on the treatment couch, the image is taken before or during the radiation delivery. Then specialized computer software is used, and these images are compared to the reference images that allow the physician to verify the image of the tumor that can be found in Figure 1.11. Any adjustments needed are made to the position of the patient and radiation beams to more precisely target the radiation at the tumor and avoid healthy tissue.

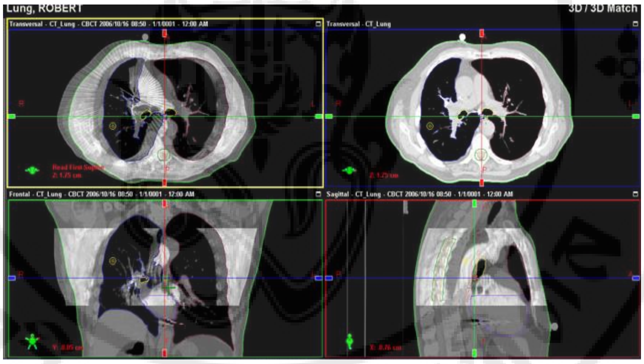

Figure 1.11 Reference and currency images are compared [47].

The IGRT for DIBH monitoring in breast cancer has several techniques such as Align RT, Planar image of kV and MV image, and CBCT. Conversely, IGRT using only orthogonal setup images may be inaccurate for breast cancer patients, exclusively intrafraction motion measurement, because the setup images may capture the patient in a breathing phase that is not representative of the anatomy. In the view of Tomas et al, use a cine mode of EPID to determine intra- and inter-fraction motion in a breast cancer patient undergoing RT. The relation between inter- and intra-fraction variability appears to be independent of each other. So indicating that patient setup and organ motion are independent parameters, as shown in Figure 1.12. Also, Intrafraction variability is smaller than inter-fraction variability to twice. The most considerable variability was detected that is cranio/caudal direction, as displayed in Table 1. 4, and they claim that cine is a quick and easy [48].

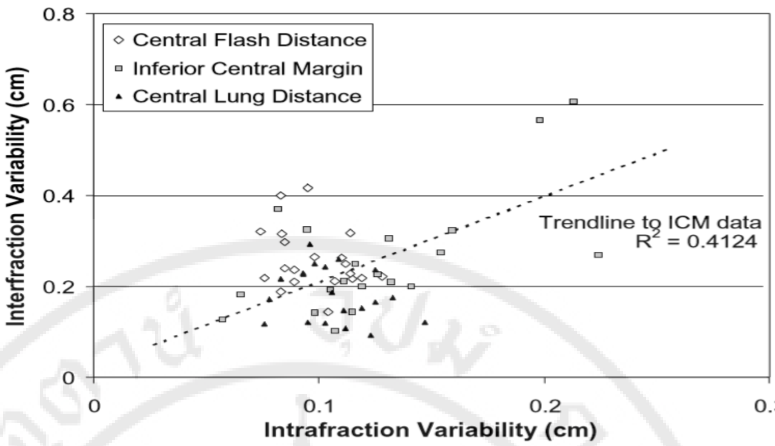

Figure 1.12 The relationship between intra- and inter-fraction variability patients [48].

Table 1. 4 Intra- and inter-fraction variability. The present is the mean and standard deviation in mm unit for all 20 patients in the study [48].

	Infra-fraction variability (mm)		Inter-fraction variability (mm)	
	Mean +/- 1SD	Average	Mean +/- 1SD	Average
Central Flash Distance	0.98 +/- 0.16	3.1	2.59 +/- 0.68	1.4 to 4.2
Inferior Central Margin	1.27 +/- 0.45	5.5	2.62 +/- 1.32	1.0 to 6.1
Central Lung Distance	1.06 +/- 0.19	3.0	1.82 +/- 0.59	0.9 to 2.9

Mette, et al used MV, kV, and cine images in the study. The setup imaging with the chest wall in uncharacteristic breathing. The mean absolute setup error of more than 5 mm in first field was 0.9%. The last field was 1.8% of the treatments, as presented in Figure 1.13 [11]. Besides, Betgen, et al (2013) used the Align RT to monitor the DIBH. The advantage is not using radiation and good agreement CBCT for measured setup error, then that can replace the 2D fluoroscopy, but CBCT remains the gold standard in this study [44]. However, the optical systems should test compare to MV or kV imaging before used; also, it is used in a small number of the hospital and used special equipment [23].

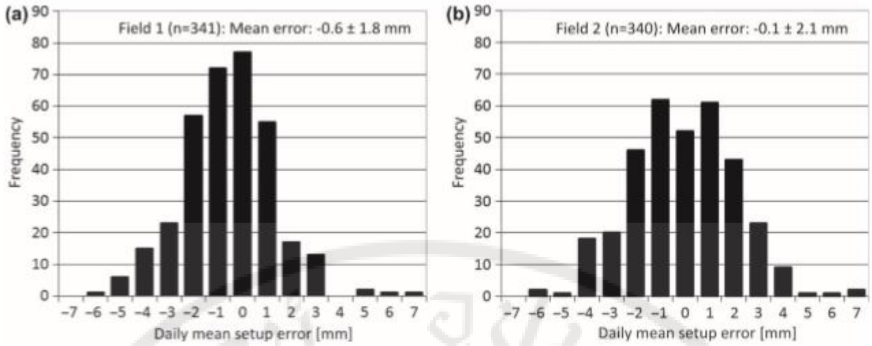

Figure 1.13 Distribution of daily mean setup errors in u direction derived from continuous portal images for (a) field 1 and (b) field 2 [11].

1.4.1 MV imaging system

The EPID produces images using a therapeutic (MV) beam. It not only delivers immediate information to position the patient correctly, but also evades the delays in film processing by port films, and with better accuracy. The standard EPID tools were developed from amorphous silicon (a-Si) bring too quickly. The images are captured and displayed on a screen EPID produced images almost instantaneously and stored the images digitally on a computer that can be acquired daily both single images and cine images. EPID has many advantages; for example, captured image as actual field delivery, quickly, and direct use of the treatment beam. The disadvantage is the contrast reduction relative to kV imaging and dose higher than kV. Also, it was limited by the size of the field width [48].

Additionally, the cine acquisition mode of EPID was used to observe intrafraction motion, as shown in Figure 1.14 [23]. Cine images were easy to acquire during the treatment of breast cancer patients without added dose to the patient. The measurements increased the treatment time by less than 1 minute due to the need to bring out and retract the EPID [48]. The benefits include time-resolved visualization of internal motion during delivery radiation in the optimal view direction without additional imaging dose. Additionally, no extra special equipment is required, except EPID. Besides, the geometrical setup error in BEV can be measured for conformal beams because of the images demonstrating the anatomy relative to the field aperture. However, the limitation of using continuous portal imaging for setup error assessment is anatomy clearly visible inside conformal field apertures [11].

Many investigators using cine mode for monitoring patients during delivery radiation [10-12, 39, 49], as shown in Table 1.5. Mette's (2014) analyze the systematic deviation in chest wall position from cine and an in-house built MATLAB computer program was used for semi-automatic registration of the chest wall position found that the intra-treatment motion of the chest wall quite small [11]. The study by Jensen (2014) used cine imaging to measure the stability of BH combine with two non-commercial surface monitoring techniques, revealed that the cine image could be used for real-time DIBH verification [10]. In 2016, a research article by De Boer used cine for examined the daily stability of a DIBH technique. They developed a fast automatic method to verify DIBH stability in each treatment fraction through a computerized analysis by detected the thoracic wall position and determined the full range of thoracic wall motion (RTWM) [49]. In 2017, Estoesta using cine imaging for detected positional reproducibility during delivery radiation in a left-sided breast cancer patient with DIBH [39].

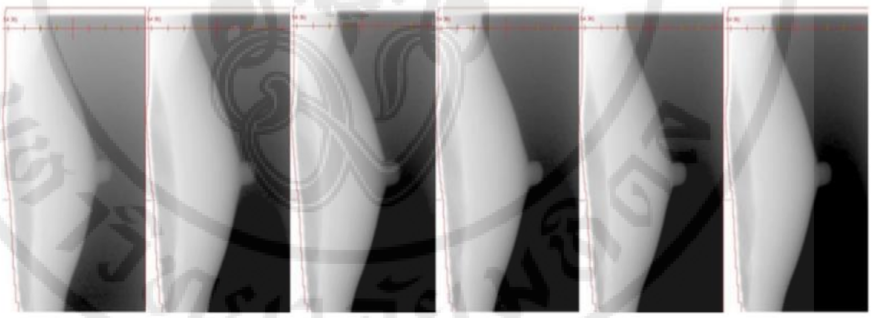

Figure 1.14 The cine segments in a DIBH patient [23].

Table 1. 5 Summary the study using cine image from EPID in breast RT

References	In the formation of the continuous portal image	
	frequency	Pixel length
Mette [11]	7.5 Hz	0.52 mm (AS500)
		0.26 mm (AS1000)
Christina [12]	2 Hz (As500)	0.52 mm (AS500)
	1 Hz (As1000)	0.26 mm (AS1000)
Jensen [10]	2-3 Hz	0.776 mm (AS1000)
Reuben [39]	2 Hz	0.52 mm (AS500)

1.4.2 kV imaging system

A kV imaging system is essential with its capability of radiography, fluoroscopy, and CBCT options. In this system, a kV x-ray tube is integrated with a flat-panel image detector on the linear accelerator. The system used to verify the accuracy of position before treatment and improved tumor targeting with 2D planar imaging and 3D volumetric imaging [15] that help to confirm a match of treatment setup. Therefore, kV imaging is typically used for confirmation of the isocenter, whereas MV imaging is used for field verification. For 2D imaging, there is better image quality and contrast than EPID with producing high-resolution diagnostic quality radiographs while also lesser radiation doses [23]. For 3D-CBCT imaging, it delivers high-resolution imaging of tumors and surrounding soft tissues. This system gains multiple kV projection during gantry rotates, combine with the filter back-projection algorithm to reconstruct the volumetric images. The advantages are more accurate anatomy and proper spatial resolution. On the other hand, there has a limitation about artifacts, cost, and scan time more than 2D imaging [15].

1.4.3 Non-ionizing image systems

Commonly, the non-ionizing-based systems in breast RT consist of ultrasound imaging and 3D surface imaging. For ultrasound, the tumor or close landmarks are overlaid on the planning CT images. It was presented that ultrasound is similar and superior to conventional CT imaging to delineate small lumpectomy cavities in patients with dense breasts. For 3D surface imaging, the shape and volume of target changes can be detected, which can capture the accurate full-surface information of the target area. This feature is particularly important for breast cancer owing to its soft-tissue effectiveness. Nevertheless, it is unable to detect the internal structures where knowledge of the internal data is necessary for accurate dose calculation. Hence, the internal structures are commonly correlated from the simulation CT data and can be verified with portal images of the target. In the view of Gierga et al. (2008) compared the accuracy of different IGRT approaches for accelerated partial breast irradiation treatment and found that kV imaging of implanted surgical clips was superior to surface imaging using 3D surface imaging, kV imaging of the chest wall, or laser alignment of skin surface marker breathing was more critical for breast movement in surface imaging [15, 50]

1.5 Assessment of the intrafraction motion of left side breast RT

The method of detecting the intrafraction motion has many studies. One interesting method is using portal images that can measure by manual or automatic. Table 1.6 explained the various anatomic distances used for assessing the interfraction and intrafraction motion in breast RT.

Table 1. 6 The parameters for measuring the intrafraction motion

Abbreviations	Term	Refer to
CLD	Central Lung Distance	The distance from the inner thoracic wall to the dorsal beam edge in the central plane of the beam
CBESD	Central Beam Edge to Skin Distance	The distance from the ventral beam edge to the skin
CCD	Crania Caudal Distance	The distance from the lower skin edge to the lower field edge at the central plane of the beam
CIW	Central Irradiated Width	The distance from the dorsal beam edge to the skin
FW	Field Width	Field size by the width of collimators
FL	Field Length	Field size by the length of the collimators
CFD	Central Flash Distance	The distance from the breast surface to the anterior field edge along the horizontal axis.
ICM	Inferior Central Margin	The distance from the inferior aspect of the breast to the inferior field edge along the vertical axis of the field
CBD	Central Breast Distance	The distance from the inner chest wall to the breast surface along the horizontal axis.
LA	Lung Area	The projection of the volume of lung irradiated onto the plane of the detector.

In 1995, Lirette, et al used on-line EPID imagery for evaluating precision and reproducibility on six parameters consisted of CLD, CIW, CBESD, CCD, FW, and FL, as shown in Figure 1.15. The parameter CLD, CBESD, and CCD are used for evaluating of intra-fraction variation. Besides, inter-fraction variations and systematic deviations were assessed by all six parameters. The maximum of standard deviations (SD) of intra- and inter-fraction are found in CCD that is 3.2 mm, and 3.4 mm, respectively.

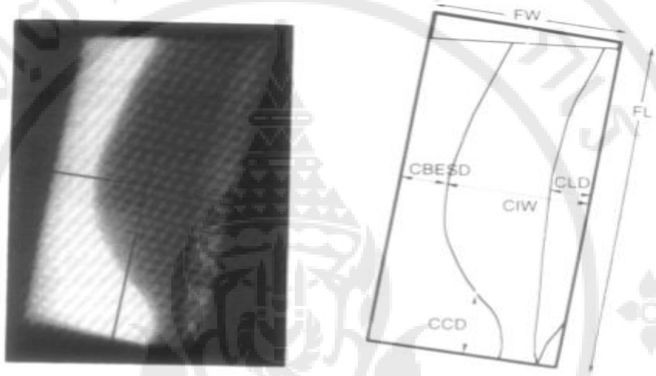

Figure 1.15 (Left) Digital portal image of tangential breast treatment. (Right) Definition of geometrical parameters: FW, FL, CLD, CIW, CBESD, and CCD [51].

Moreover, Fein, et al (1996) using anatomical features including the LA, CLD, CBD, CFD, and ICM presented in Figure 1.16 to measure patient movement during treatment and setup reproducibility from electronic on-line portal imaging. Also, the LA for intrafraction and interfraction is 1.50 cm^2 and 4.19 cm^2. The Intrafractlonal variation for the other variables ranged from 0.85 mm for ICM to 2.1 mm for CBD, while interfractlonal variations ranged from 3.2 for CBD to 6.25 mm for ICM, respectively.

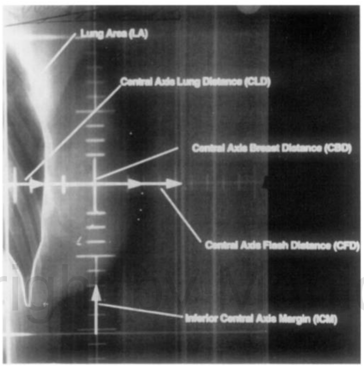

Figure 1.16 Digitize simulation image showing LA, CLD, CBD, CFD, and ICM [52].

In 2004, the study of Kron using a cine image to determine inter- and intrafraction motion in left-sided breast RT. In each image was measured distanced of CFD, CLD, and ICM on computer screening by using a ruler tool in Varis Vision Version 6.1 (Varian Medical Systems, Palo Alto), as shown in Figure 1.17. The largest intra-fraction variability was detected in the cranial/caudal direction of 1.3 +/- 0.4 mm, while the lung involvement varied by 1.1 +/- 0.2 mm. The inter-fraction variability was found larger than intra-fraction variability twice. Generally, the results of inter-fractional variabilities in Kron's study were smaller than by Fein et al. who published 4.4, 6.3, and 4.4 mm for CFD, ICM, and CLD, respectively [52] but Kron's study of 3.1, 5.5, and 3.0, respectively.

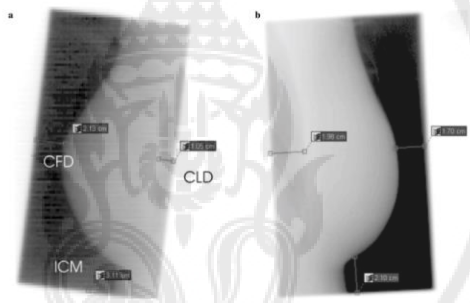

Figure 1.17 The locations of the measurements CFD, ICM, and CLD[48].

In 2012, Michalski, study a systematic review of inter- and intrafraction motion from anatomical landmark to isocenter on MV image, portal film, kV image, or CBCT. Three groups informed on the magnitude of intrafraction motion in breast cancer patients are CLD, CBESD, and CCD, as presented in Table 1.7.

Table 1.7 The magnitude results of intra-fraction motion in breast cancer patients

Observers	Standard deviation (mm)			maximum deviations (mm)		
	CLD	CBESD	CCD	CLD	CBESD	CCD
Lirette [51]	1.8	2.1	3.2	13.1	14.9	25.6
Fein [52]	1.6	1.7	0.85	-	-	-
Kron [48]	3	3.1	5.5	-	-	-

In the view of Jensen (2014), they used a cine image for evaluated BH. The algorithm was written in MATLAB (MATLAB 7.12, The MathWorks Inc., Natick, MA) with a Canny filter for the detect edge of the chest wall. Also, the distance between the chest wall and the image border was measured as Figure 1.18. The median intra-beam chest motion was 0.37 mm, and the maximum exceeded treatment protocol threshold of 3 mm in 1.2%.

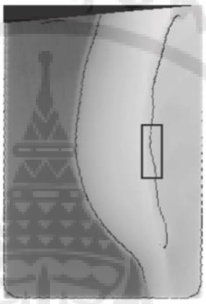

Figure 1.18 The image of the breast and chest wall during DIBH, and the location of the detected edge agrees with the visual estimate of the chest wall location [10].

From the study by Thomsen (2014), the in-house MATLAB program was used for semi-automatic registration in all MV images of the chest wall position. In addition to the field edge in u direction as Figure 1.19. The registration resulted in the intra-treatment chest wall motion in BEV with an offset relative to the arbitrary field edge.

Figure 1.19 Setup procedure and imaging for a breast cancer patient [11].

In 2015, Lutz's study that the cine was analyzed from an in-house developed MATLAB program. This program used the distinct pixel intensity y variations of the chest wall to determine the position in the u-direction in three regions, as Figure 1.20.

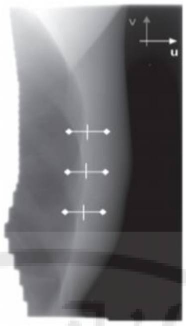

Figure 1.20 The relative deviation of the chest wall was found by comparison of the pixel intensities [12].

In 2016, a research article by De Boer used cine for examined the daily stability of a DIBH technique. They developed a fast automatic method to verify DIBH stability in each treatment fraction through a computerized analysis by detected the thoracic wall position in each frame and determined the RTWM. In these cases, 98% of patients can maintain a stable voluntary moderate DIBH The results; the RTWM averaged over all patients was 0.9 mm. Also, the interpatient variation was 0.5 mm [49].

Table 1.8 The previous study to analyze the stability of BH.

References	Parameter	Analyzed from
Lirette [51]	CLD, CBESD, and CCD	EPID manufacturer's platform
Fein [52]	LA, CLD, CBD, CFD, and ICM	Film and Ethernet connection
Kron [48]	CFD, ICM, and CLD	Computer screening by using a ruler tool in Varis Vision Version 6.1
Jensen [10]	Chest wall	MATLAB
De Boer [49]	RTWM	TNT software (Elekta)
Lutz [12]	Chest wall	MATLAB
Estoesta [39].	CA to ICW	Varian ARIA Offline Review Imaging software

1.6 Edge detection algorithm

Edge detection is a category of image segmentation technique where the image is detected from the edge. Edges are presented as a set of connected points lie on the boundary between two regions, which detect the sharp changes in intensity value or pixel value of the image [53]. The main steps of edge detection are filtering enhancement and detection. Edge detection produces a line drawing scene from the image. Various essential features like corners, lines, curves can be extracted from these lines. Extracted features can be used for recognition as a higher-level computer vision algorithm. The frequently used are Sobel, Robert, Prewitt, Laplacian, LoG (Laplacian of Gaussian), and Canny edge detection technique, as Figure 1.21 displayed the different types of edge detection algorithms [54].

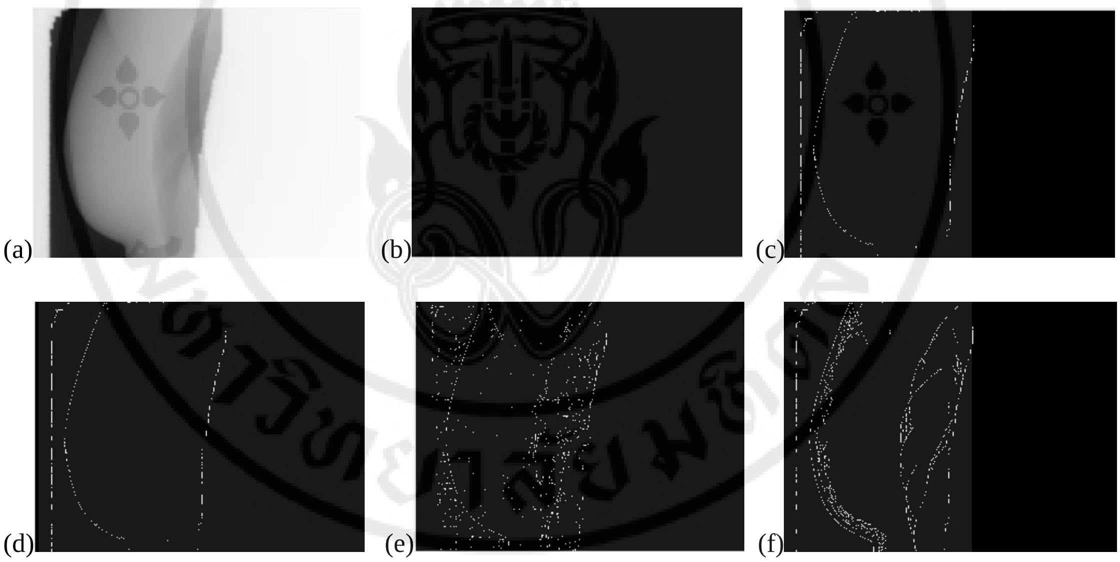

Figure 1.21 The sample images for edge detection (a) Original image (b) Robert (c) Sobel (d) Prewitt (e) Log (f) Canny.

1.6.1 Sobel edge detection algorithm

The Sobel detector is a discrete differential operator that measures a 2D spatial gradient on an image and gives more attention to regions of high spatial gradient corresponding to edges. Also, the Sobel detector is used for finding gradient magnitude at each point in a grayscale image. The Sobel operator involves a pair of 3×3 convolution kernels. Then, one kernel is simply the other rotated by 90º, as presented in Figure 1.22. These kernels are considered to respond maximally to edges, which are vertical and horizontally relative to the pixel grid [53].

-1	0	1
-2	0	2
-1	0	1

G_x

1	2	1
0	0	0
-1	-2	-1

G_y

Figure 1.22 Sobel mask.

1.6.2 Prewitt's edge detection algorithm

Prewitt detector is similar to the Sobel detector that is used for detecting vertical and horizontal edges in images to estimate the magnitude and direction of an edge. The advantage is a fast method for edge detection that is limited to 8 possible directions. Nevertheless, most direction estimates are not much more accurate. This gradient-based edge detector is estimated in the 3x3 the neighborhood for eight directions. All eight convolution masks are calculated. The convolution mask with the most extensive module is then selected. The convolution masks of the Prewitt detector are shown below Figure 1.23 [53].

1	1	1
0	0	0
-1	-1	-1

-1	0	1
-1	0	1
-1	0	1

Figure 1.23 Prewitt Mask.

1.6.3 Canny edge detection algorithm

The Canny edge detection is one of the primary edge recognition operators that use a multi-stage process to detect an extensive range of edges in images. Canny target was to find out the optimal edge detection algorithm. The optimal function in the Canny detector is described in 5 steps, as shown in Figure 1.24. In the first step, apply the Gaussian filter to smooth the image to remove the noise. Second, find the intensity gradients of the image. Then, apply non-maximum suppression to get rid of spurious response to edge detection and double threshold to determine potential edges by hysteresis [54-56].

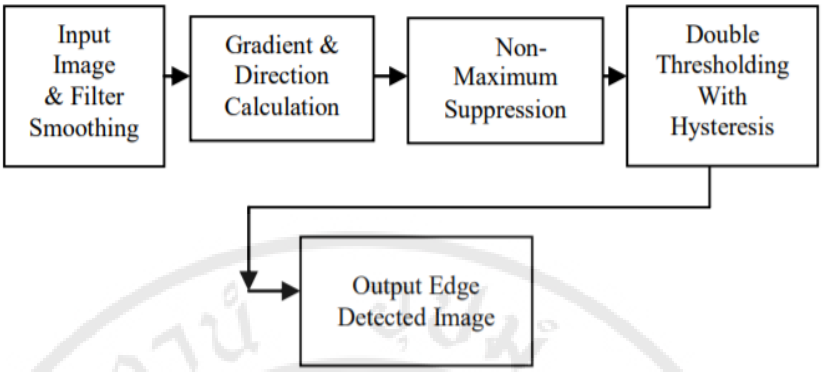

Figure 1.24 Canny edge detection algorithm.

From the study by Joshi shown that both of Sobel and Prewitt edge detector can detect edges, but the performance of the Canny edge detector is better than Sobel and Prewitt edge detector [53]. Table 1.9 shows the overall summary of the operators about the advantages and disadvantages [55, 56]. The study by Anas (2019) is also showed that the Canny algorithm was better in removing most of the noise from medical images while hiding some of the edges of the images when compared with Prewitt and LOG [57].

Table 1.9 Compare the advantages and disadvantages of edge detectors.

Operator	Advantages	Disadvantages	Application area
Sobel Prewitt	- Simplicity and suitable for simple images - Detection of edges and their orientations	- Inaccurate - Sensitive to noise	- Massive data communication and data transfer
Canny	- Smoothing effect to remove noise - Good localization and response - Immune to a noisy environment. - Better detection especially in noise conditions	- Challenging to implement to reach real-time response. - Time-consuming - Complex computations - False zero crossing	- The medical field for X-ray diagnosis and object recognition

CHAPTER II
OBJECTIVES

2.1 To simulate the motion acceptance range of breath-hold in the DIBH technique towards the tolerance level determination.To develop a daily patient DIBH instability assessment as an intra-fractional motion verification tool using a cine-electronic portal imaging device (cine-EPID).

CHAPTER III
MATERIALS AND METHODS

3.1 Materials

3.1.1 Computed tomography (CT) simulation

The Philips Brilliance CT Big Bore (Philips Medical Systems, Madison, WI) was used in this study, as demonstrated in Figure 2.1 that was designed as a CT simulator 16 slices to provide clinical excellence in radiation oncology with 85 cm bore size. Besides, a 60 cm true scan FOV for full anatomic visualization also affords spatial positioning accuracy of less than 2 mm between the lasers marking plane.

Figure 3.1 The Philips Brilliance Big Bore 16-Slice CT scanner [58].

3.1.2 Treatment planning system

The left breast treatment planning in this experiment was created by using the Eclipse treatment planning system version 13.6 (Varian Medical Systems, Palo Alto, CA, USA) in part of test accuracy, and RaySeach version 8B (RaySearch Laboratories AB, Stockholm, Sweden) was used to simulate organ motion for determined the tolerance level of breath-hold capability.

3.1.3 The Linear accelerator machine

A Varian Trilogy™ linear accelerator (Varian Medical Systems, Palo Alto, CA) was experimented in this study, as illustrated in Figure 3.2. This machine has photon output energies at 6 MV and 10 MV and high mechanical performance, including 120 leaves of MLC. The IGRT consists of an On-Board Imager (OBI) controlled by two robotic arms and EPID. Images of the MV beam were acquired using an aSi EPID (Portal Vision MV AS-500) attached to the LINAC. MV source-detector distances (SDD) are set to 150 cm, and the kV imaging was obtained by using OBI located perpendicular to the treatment beam. Both MV and kV detectors have a pixel width of 0.392 mm and a maximum resolution of 1024×768, corresponding to a 40 cm×30 cm effective area of detection [59].

Figure 3.2 The Varian Trilogy with kV and MV imagers in extended positions [60].

3.1.4 MotionSim-XY/4D

The MotionSim XY/4D™ (Sun Nuclear Corporation) is shown in Figure 3.3. The MotionSim-XY/4D is designed for the quality assurance (QA) test of motion effects in radiation therapy imaging and delivery by moving a phantom and is controlled by MapCHECK. The software consists of a programmable 2D moving bed and 1D breathing.

Figure 3.3. The MotionSim-XY/4D [61].

3.1.5 Rando phantom

A female Rando Alderson anthropomorphic phantom (Figure 3.4) was used to represent a breast cancer patient. The phantom is molded by tissue-equivalent material and is designed within highly sophisticated technological constraints that follow the ICRU-44 standard [62]. The phantom is transected-horizontally into 2.5 cm thick slices. Each slice has holes that are plugged with bone-equivalent, soft-tissue-equivalent, or lung tissue equivalent pins. The small size of breasts was used in this study.

Figure 3.4 The Alderson Radiation Therapy Phantom [63].

3.1.6 MATLAB software

MATLAB version R2018a program (MathWorks, Natick, MA) with the Canny edge detection algorithm was used in this study to assess the stability of DIBH.

3.2 Methods

Regarding our retrospective study of left breast radiotherapy with the DIBH technique, the experiment was separated into two parts. The first one is to simulate the patient's motion to determine the breath-hold tolerance level. The second part is the development of intra-fractional patient motion verification of DIBH. The system overview of this experiment is displayed in Figure 3.5.

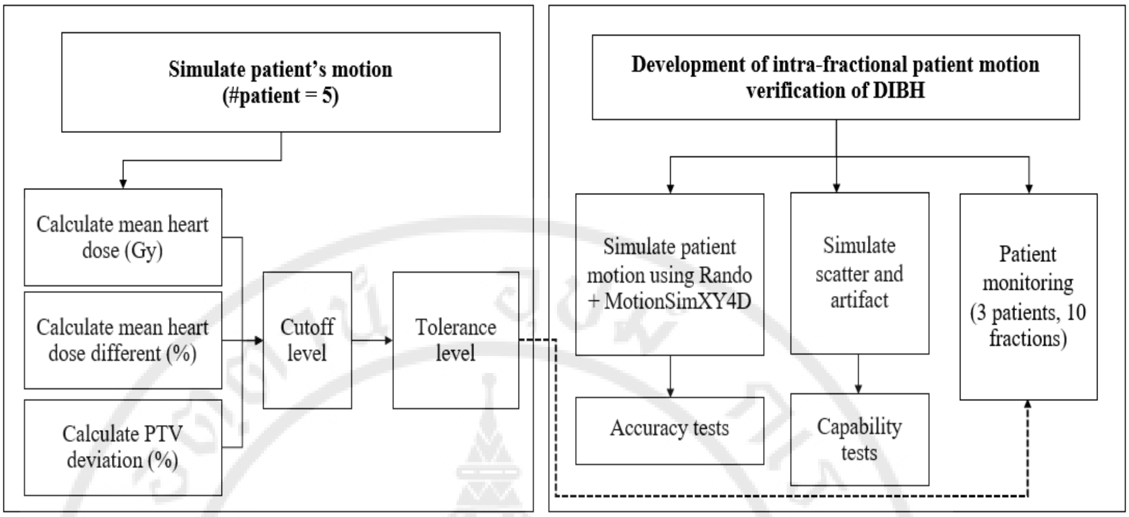

Figure 3.5 The system overview of this experiment.

Five patients with left breast cancer treated by the DIBH technique at Chulabhorn Hospital from January - October 2019 were selected for tolerance level determination. Besides, three more patients treated from December 2019 to February 2020 were selected for the breath-hold assessment.

All patients underwent a DIBH CT scan with an RPM system, then the treatment plans for FIF technique were done using the Eclipse treatment planning system version 13.6 with 95.0% target coverage and 7 Gy MHD limit. In the treatment room, the patients held their breath using audio coaching from therapists and visual feedback from goggles. The therapists controlled radiation delivery by observing from the RPM system. The radiation was on when the patient held the breath in the gating window level within 2 mm and off when the patient breath-hold exceeds the limit.

3.2.1 Tolerance level determination

The treatment planning data of the patients were exported from the Eclipse planning system to RaySeach version 8B. Furthermore, the chest wall was delineated on the planning CT and simulated for chest wall movement with ±3 mm to ±15 mm in AP direction, as presented in Figure 3.6. Moreover, the MHD was calculated for determining the optimal tolerance level of patient breath-hold by comparing MHD with the cardiac toxicity from Darby's study [5] and based on Chulabhorn Hospital protocol, which is used for deciding option to use FB or DIBH techniques.

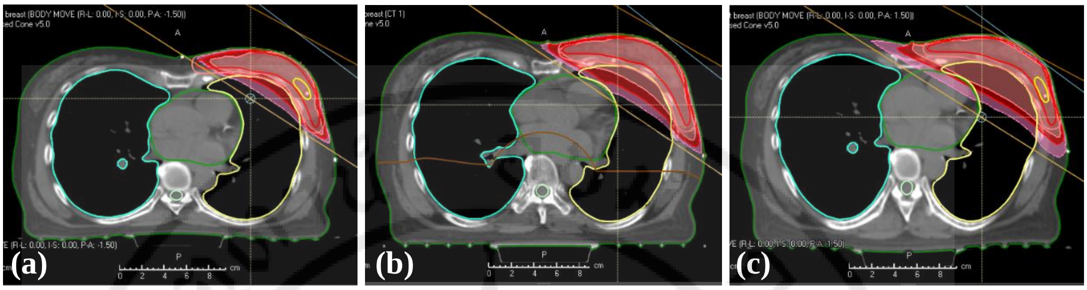

Figure 3.6 The simulated breathing motion at (a)-1.5 cm, (b) 0 cm, (c) 1.5 cm

3.2.2 Automated DIBH instability assessment algorithm

The automated EPID-based DIBH evaluation tool was developed using MATLAB/SIMULINK version 2018b. Cine EPID images were obtained during treatment delivery. After patients were treated, the cine EPID images were saved in the ARIA database. Then, the images were analyzed the results by the in house MATLAB. In the first step, the cine images were used for an input image that is converted to a double grayscale. Thus the Canny edge detection of MATLAB code was written and used a Gaussian smoothing filter, which removed the majority of image artifacts yet preserved the chest wall boundary. Besides, every image was rotated to zero degrees, and the median filter and Wiener filter were applied. Next, the program displays the edges image. Finally, the line profile was built at the center of the image along the horizontal direction. The distance of lung depth was measured from the peak. The processes of in house MATLAB are shown in Figure 3.7.

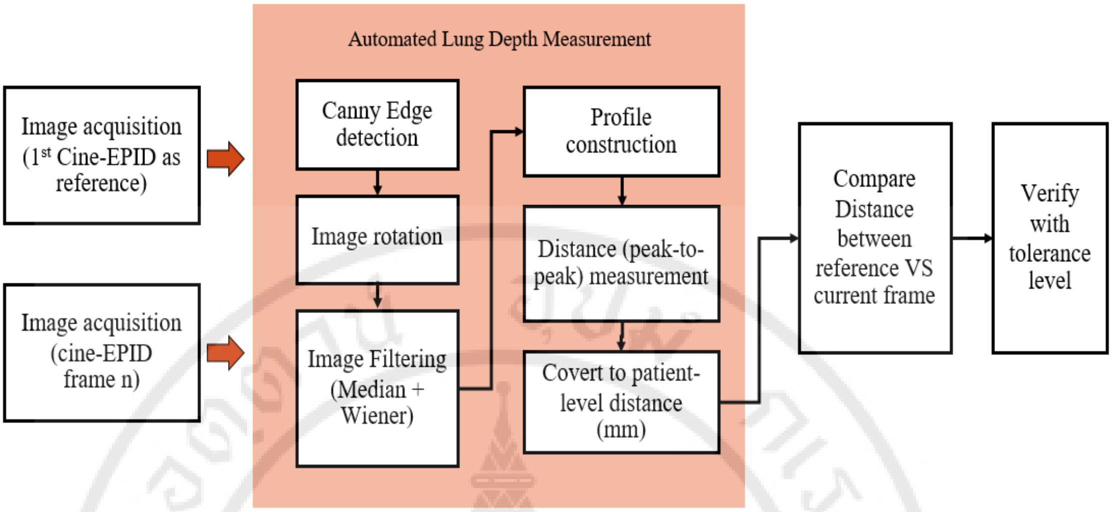

Figure 3.7 The system overview of automated lung depth measurement.

3.2.2.1 CT image acquisition

The experiment was performed using Rando phantom combined with MotionSim-4D/XY to acquired CT images. Due to the limitation of MotionSim-4D/XY that can move in the lateral (x) and longitudinal (y) direction. However, the purpose of this experiment is to test in the vertical (z) direction. So Rando phantom was flip 90° as Figure 3.8 when the MotionSim-4D/XY move in a lateral direction, which means the Rando phantom move in a vertical direction. In the CT scanning process, the phantom was scanned without moving for expressive to the patient can successfully breath-hold. Then, this CT imaging was planned in the 3D technique by using Eclipse TPS. Also, the angle of the tangential radiation field was 239 and 39 degrees that were not opposing field due to the limitation of the electronic part. Thus, the CT images (3D) were reconstructed into DRR image (2D) for verification of the position before treatment, as presented in Figure 3.9.

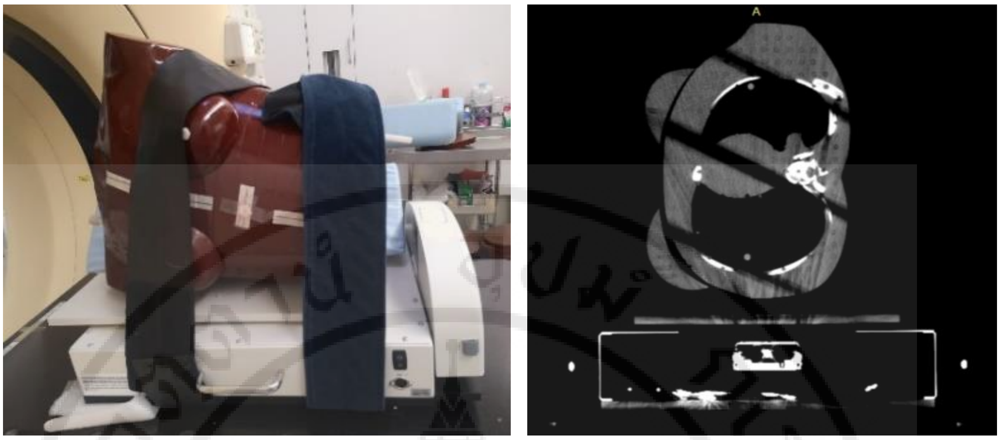

(a) (b)

Figure 3.8 (a) Setup Rando phantom with MotionSim-4D/XY on CT simulator and (b) CT images for planning.

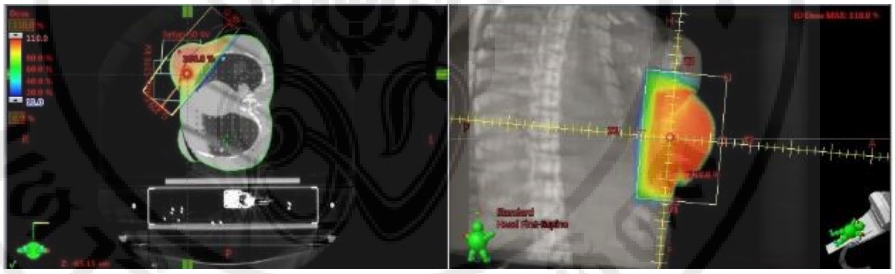

Figure 3.9 3D Treatment planning of left side breast cancer.

3.2.2.2 Cine image acquisition

Before the acquired cine image in this experiment, the imager was calibrated with a dark field and flood field. Then, the Rando phantom and MotionSim-4D/XY was set on the couch of the LINAC machine in the same position with CT-simulation as shown in Figure 3.10. Before delivery radiation, the EPID was used to verify and adjust the position of the phantom by comparing it with the DRR image. Formerly, the cine images were acquired during radiation delivery by using EPID. The phantom was moved the different motion that parameter setting from amplitude and speed time then acquired cine images. The pattern of motion can be separated into eight groups, as presented in Table 3.1. Besides, the cine imaging was used for assessing the performance of MATLAB in house programs, including accuracy and capability.

Figure 3.10 Setting the Rando phantom with MotionSim-4D/XY on LINAC.

Table 3.1 The pattern of phantom motion.

Group	Gantry angle (º)	Amplitude (mm)	Time (second)
1	239	0	0
2	239	2.5	1
3	239	2.5	0.5
4	239	5.0	1
5	39	0	0
6	39	2.5	1
7	39	2.5	0.5
8	39	5.0	1

3.2.2.3 Applying Canny edge algorithm

The Canny edge algorithm was applied in this in house MATLAB. The process of the algorithm had several steps as presented in Figure 3.11. A Gaussian filter was applied to remove noise from the image because it can lead to misunderstanding the result in the finding edges. The pixel values of the data input were convolved with a convolution mask and were created as an intermediate image. Then, the algorithm is finding edges where the intensity of the greyscale changes to the maximum value. Besides, 3x3 Sobel edge detection was performed on both the horizontal and vertical, to find the intensity gradients. The edge strength G is

$$|G| = |Gx| + |Gy| \tag{3.1}$$

The direction of the edge was computed using the gradient in the x and y directions as

$$\theta = \arctan(Gy/Gx) \tag{3.2}$$

The edge orientation was resolved to one of four angles 0, 45, 90, or 135 degrees. Next, non-maximum suppression was applied that was used to find the edge in the many directions and suppress any pixel value, and the result is thinner edge lines. Some edge might be caused by noise or color variations, such as the rough surface. So, we can apply thresholding for stronger edges. For final edges, the function Hysteresis Thresholding modifies the weak edge to a sharp edge [53].

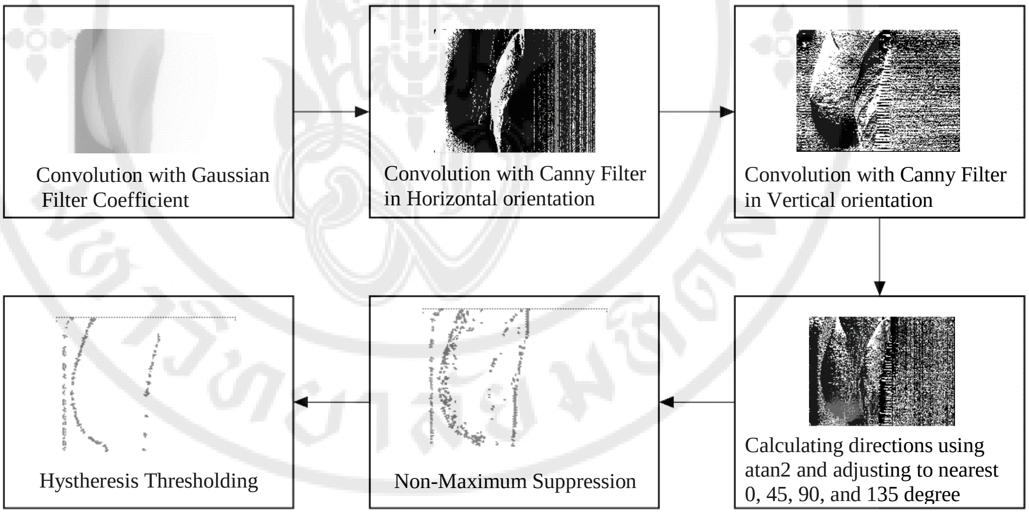

Figure 3.11 The process of applying canny edge detection.

Also, the image was rotated to a straight image if the collimator was tilted. For the right anterior oblique field (RAO), the image was rotated to 0 degrees as figure 3.12 (a). On the contrary, the image of the left posterior oblique field (LPO) was rotated to 180 degrees as figure 12 (b). Also, the median and Wiener filters were applied to reduce noise and deblur.

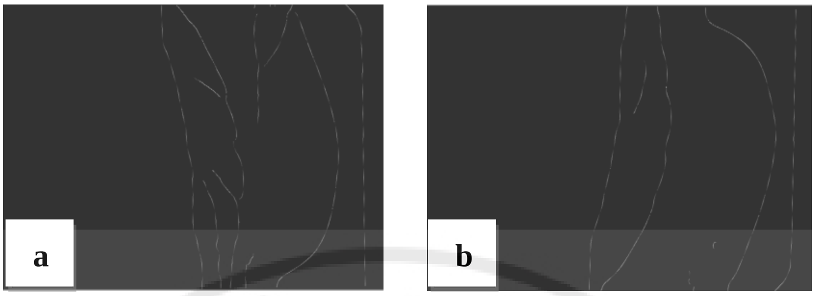

Figure 3.12 The example of canny edge image in (a) RAO and (b) LPO field.

3.2.2.4 Automated Lung Depth Measurement

The distance of lung depth in each cine image was measured for evaluating the intrafraction motion. The profile was built along a horizontal line at the center of the image that retrieves the intensity values of pixels along a line. Thus, the peaks were used to find the distance of lung depth by subtraction the pixel values of peak one to peak two as figure 3.13. Then, the pixel value was corrected with pixel spacing and magnification of the image. The lung depth in each cine image was compared with the first cine image in each fraction.

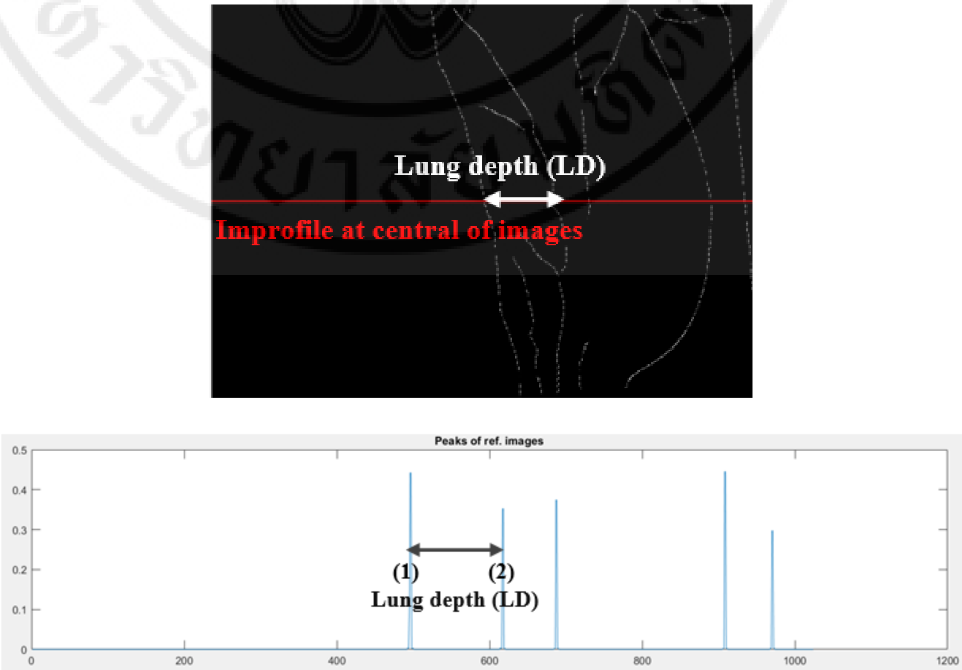

Figure 3.13 The profile along a horizontal line at the center of the image (upper), and the profile retrieves the intensity values of pixels along a line (lower).

3.2.1.5 Testing the performance of the assessment tool

A. Accuracy test

All cine images of phantom motion were used to verify the accuracy of the DIBH assessment tool. After the image was analyzed by in house MATLAB program, the results were shown the distance of lung depth. Then the data were compared with the prediction value that was calculated from the sine wave equation as Equation 3.3

$$X = Acos\frac{2\pi}{T}t \tag{3.3}$$

Where x means displacement value, capital T is the time period accurately describes the relationship of such an oscillating body, and t is time to the acquired image.

Then, the lung depth distance was calculated to rescale value compared with the prediction data from Equation 3.4

$$\text{Xnormalized} = (b-a)\left(\frac{x-min(x)}{max(x)=min(x)}\right)+a \tag{3.4}$$

Where Min(x) denotes the minimum of the range of measurement

Max(x) denotes the maximum of the range of measurement

Capital a denotes the minimum of the range of desired target scaling

Capital b denotes the maximum of the range of desired target scaling

Root Mean Square Error (RMSE) was also calculated that was used to measure the error of a model in predicting quantitative data. Formally it is defined as follows

$$\text{RMSE} = \sqrt{\sum_{i=1}^{n}\frac{(\hat{y}_i - y_i)^2}{n}} \tag{3.5}$$

Where $\hat{y}$ is a predicted value

y is an observed value

n is the number of observations

B. Capability test

In this experiment, the cine images have been introduced an error to test the ability to analyze the results of the program in abnormal conditions that were divided into three scenarios consist of simulated the blurring images, added Gaussian noise, and salt and pepper noise. Moreover, each scenario also had three levels. For scenario 1, the blurring or degradation of the image can be approximately described by equation 3.5. The images are different point spread function (PSF) consists of blurring 7, 10, blurring 10, 10, and blurring 15, 15, as shown in Figure 3.14.

$$g = Hf + n \tag{3.6}$$

Where
- g is the blurred image
- H is the distortion operator, also called PSF
- f is the original image
- n is Additive noise, introduced during image acquisition, that corrupts the image

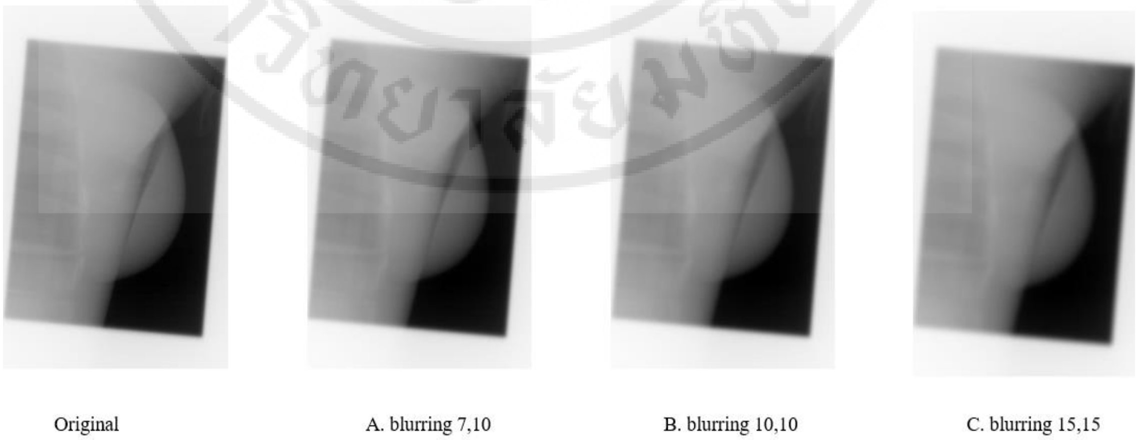

Figure 3.14 The image from different PSF.

For scenario 2, the Gaussian noise was introduced into an image in different values consist of 0.000001, 0.00001, 0.000025, as demonstrated in Figure 3.15. Gaussian noise is a random variable N that has a normal distribution, denoted as N~ N (μ, σ^2), where μ the mean and σ^2 is the variance.

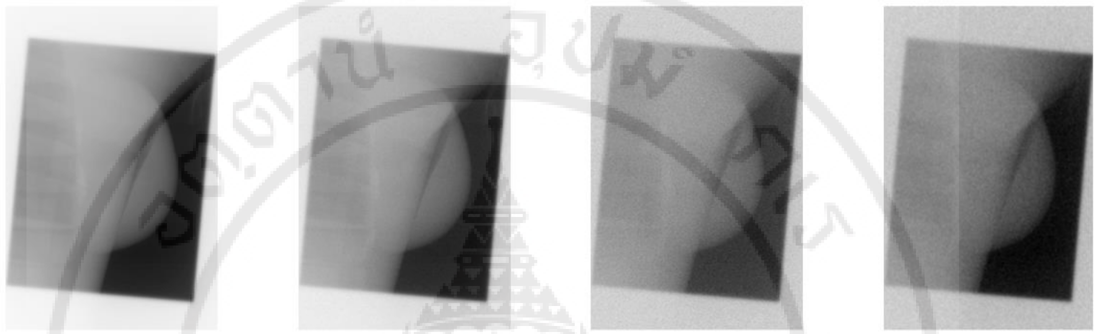

Original A. Gaussian 0.000001 B. Gaussian 0.00001 C. Gaussian 0.000025

Figure 3.15 The image from different Gaussian noise.

For scenario3, the salt and pepper noise was also added into the image. This type of noise consists of random pixels being set to black or white. The parameter set consists of 0.0005, 0.001, and 0.002, as presented in Figure 3.16.

Original A. Noise 0.0005 B. Noise 0.001 C. Noise 0.002

Figure 3.16 The image from different salt and pepper noise**.**

C. Applying in clinical

The cine image of three patients left side breast cancer without SPC who were treated with DIBH technique was selected in this study for evaluating the stability of DIBH. The number of the fraction was ten, and the number of cine images was used for analysis is 115. In each patient have a different character. The first, the patient, has large breast conservative surgery. Second, breast mastectomy is both with and without a bolus plan: the last, the small breast conservative surgery, as shown in Figure 3.17. The images were analyzed by a measured distance of lung depth in each field. Then the results were used to evaluate the intrafraction motion in each fraction to consider 'stable' or 'unstable.' of breath-hold.

Figure 3.17 The cine images of each patient.

CHAPTER IV

RESULTS

4.1 Tolerance level determination

For this study, the median patient age was 59 years (range 47 to 68 years). The average MHD is 4.594 Gy (range 2.73 to 6.46 Gy). The breathing motion and MHD in all motion determined the tolerance level of DIBH, as shown in Figure 4.1. The minimum and maximum MHD from simulated breathing motion from RaySeach treatment planning at a range between ±3 to ±15 mm were 1.89±1.50 Gy (or MHD reducing 58.42%) for breathing motion -15 mm and 9.60±2.45 Gy (or MHD reducing 108.88%) for breathing motion +15 mm as shown in Figure 4.2. Also, breathing motion -15 mm found that the PTV is reduced up to 5.6%, as presented in Figure 4.3.

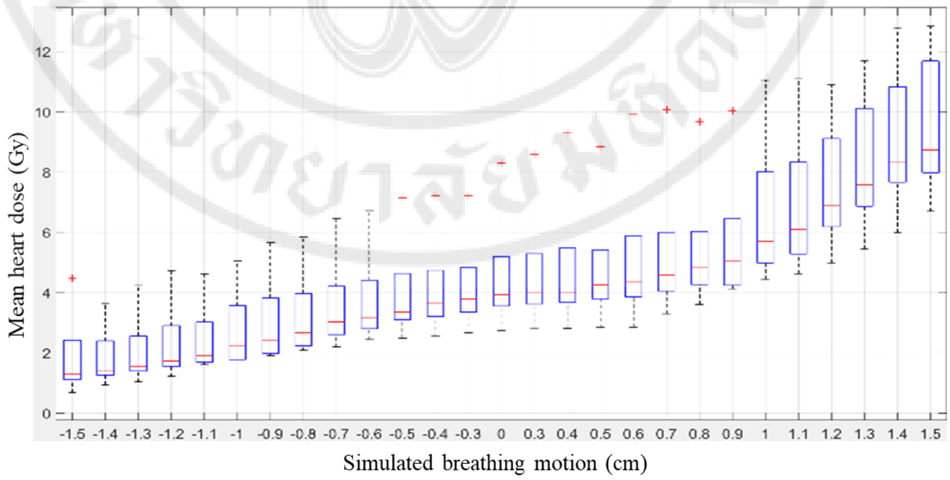

Figure 4.1 The average and range of the breathing motion and MHD for determined the tolerance level of DIBH.

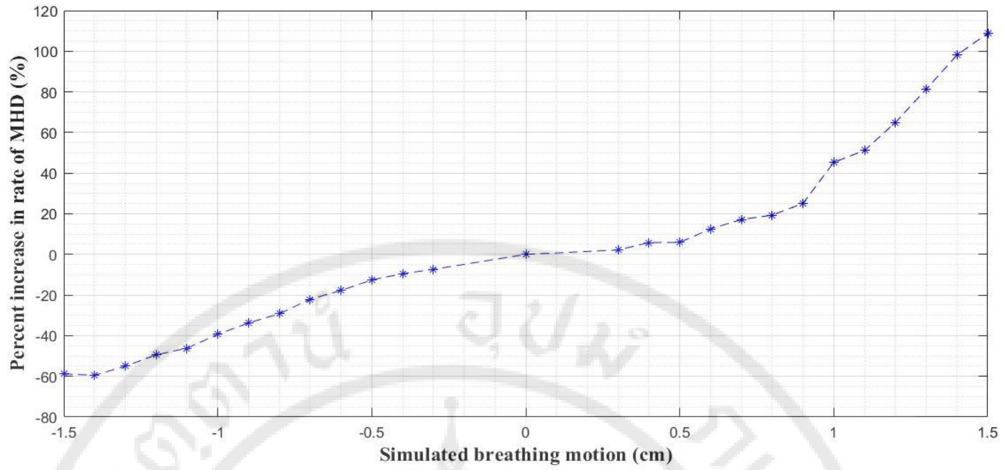

Figure 4.2 The rate of MHD change (%) as compared with the breathing motion (cm).

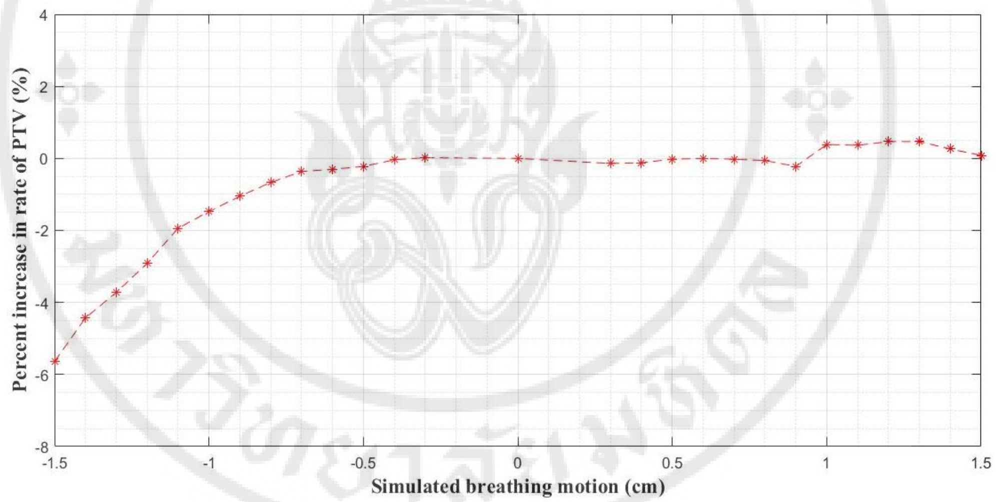

Figure 4.3 The rate of PTV change (%) as compared with the breathing motion (cm).

4.2 Automated DIBH instability assessment algorithm

A. Accuracy test

All eight series of cine imaging were used for assessing the accuracy of the automated DIBH instability assessment algorithm. The results were compared between prediction value and measurement value in each pattern of motion. The results are shown in Table 4.1.

Table 4.1 The results of testing the accuracy of the assessment tool.

Group	Gantry angle (°)	Amplitude (mm)	Time (second)	Maximum difference (mm)	RMSE (mm)
1	239	0.0	0.0	-0.300	0.195
2	239	2.5	1.0	0.934	0.444
3	239	2.5	0.5	0.686	0.366
4	239	5.0	1.0	-0.807	0.385
5	39	0.0	0.0	0.500	0.264
6	39	2.5	1.0	-0.996	0.353
7	39	2.5	0.5	-0.989	0.425
8	39	5.0	1.0	-0.714	0.395
	Absolute mean difference			0.741	0.353
	SD			0.246	0.084

For phantom move with amplitude 0 mm and time 0 second, the maximum difference values are -0.3 mm for gantry angle 239º and 0.50 mm for gantry angle 39º. Then, the RSME in gantry angle 239º and 39º are 0.195 mm and 0.264 mm, respectively, as shown in Figure 4.4 and Figure 4.5.

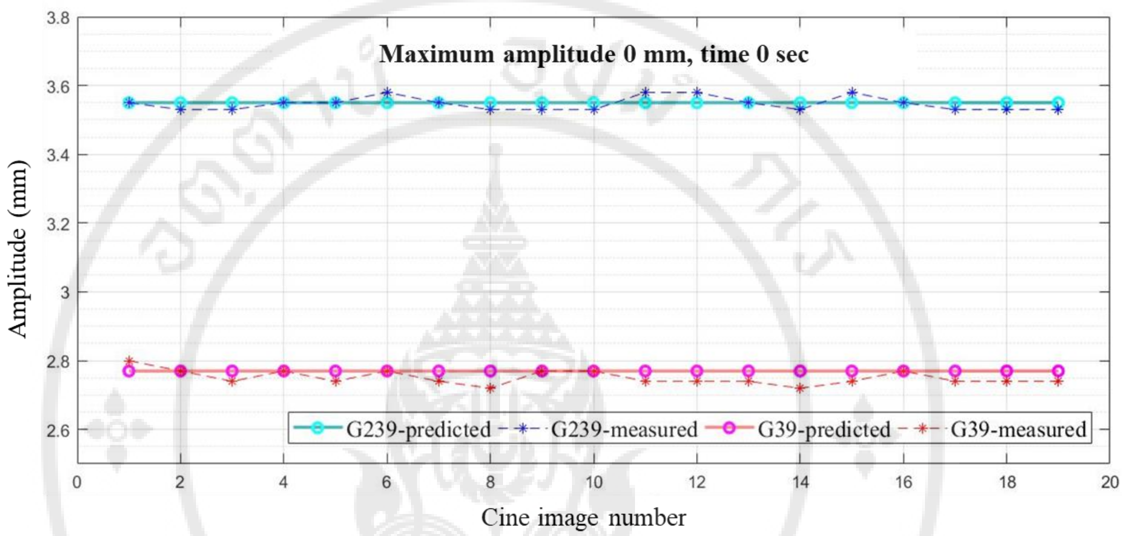

Figure 4.4 Testing accuracy from the cine images of phantom moving with amplitude 0 mm and time 0 second in gantry angle 239º and 39º.

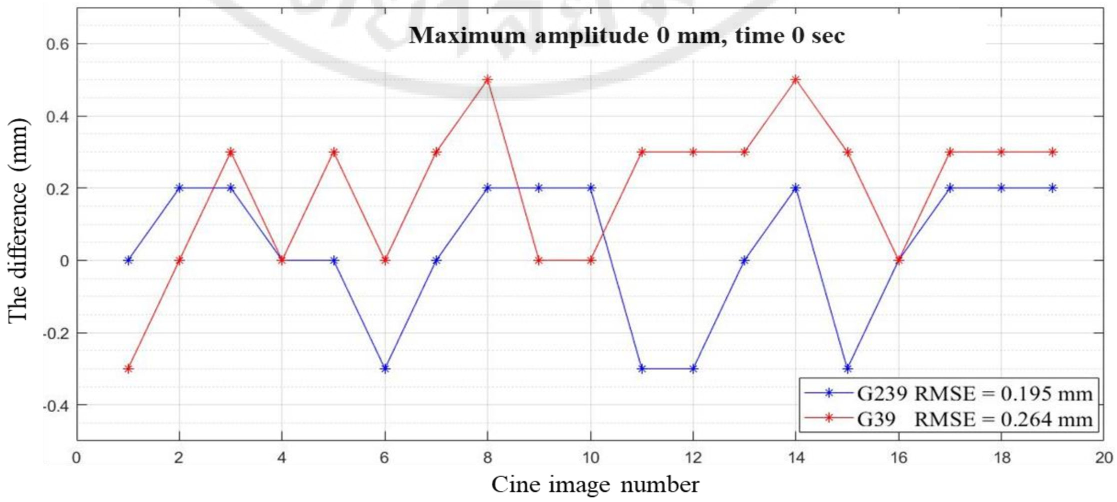

Figure 4.5 The different values between prediction and measurement from the cine images of the phantom with amplitude 0 mm and time 0 second.

For the pattern of phantom movement with amplitude 2.5 mm and time 1 second, the maximum difference values are 0.934 mm for gantry angle 239º and -0.996 mm for gantry angle 39º. The RSME in gantry angle 239º and 39º are 0.444 mm and 0.353 mm, respectively, as presented in Figure 4.6 and Figure 4.7.

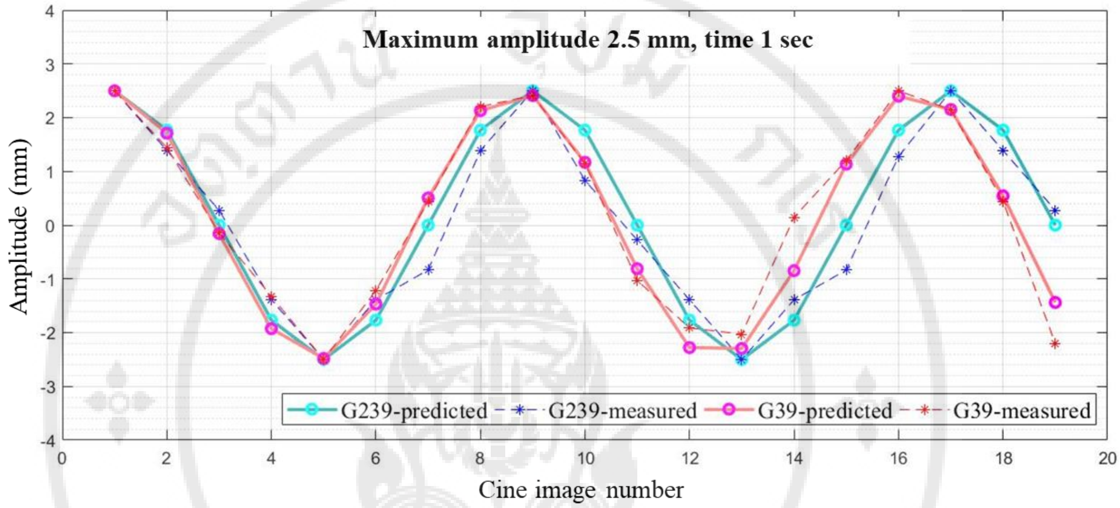

Figure 4.6 Testing accuracy from the cine images of phantom moving with amplitude 2.5 mm and time 1 second in gantry angle 239º and 39º.

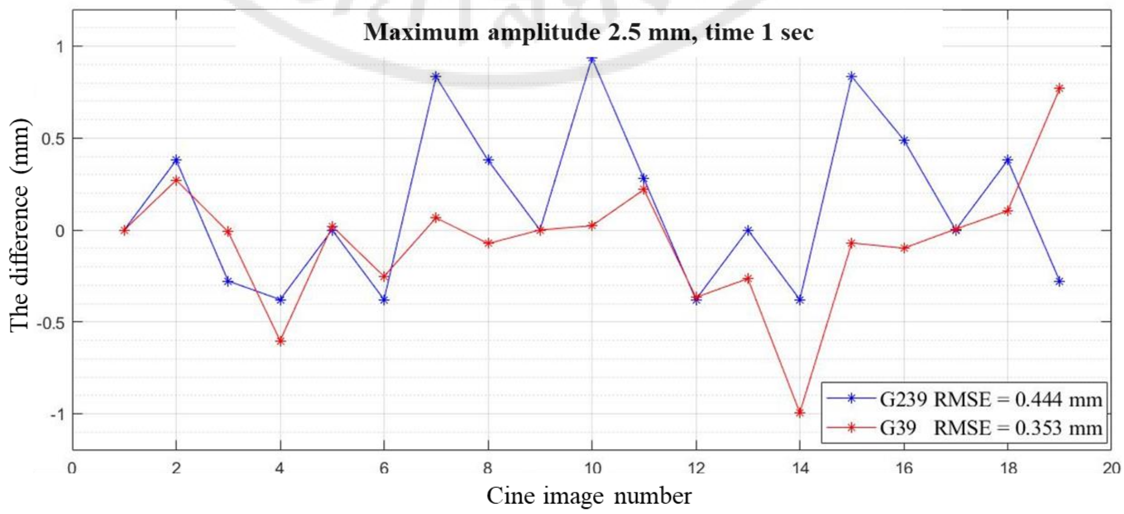

Figure 4.7 The different values between prediction and measurement from the cine images of the phantom with amplitude 2.5 mm and time 1 second.

Furthermore, the phantom motion faster with time 0.5 second, found that the maximum difference values are 0.686 mm for gantry angle 239º and -0.989 mm for gantry angle 39º. The RSME in gantry angle 239º and 39º are 0.366 mm and 0.425 mm, respectively, as shown in Figure 4.8 and Figure 4.9.

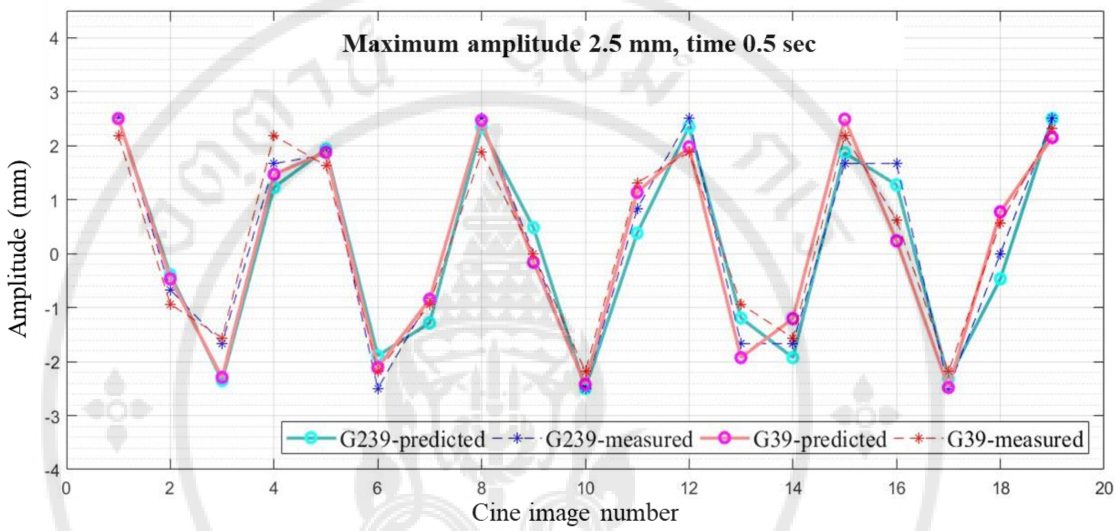

Figure 4.8 Testing accuracy from the cine images of phantom moving with amplitude 2.5 mm and time 0.5 seconds in gantry angle 239º and 39º.

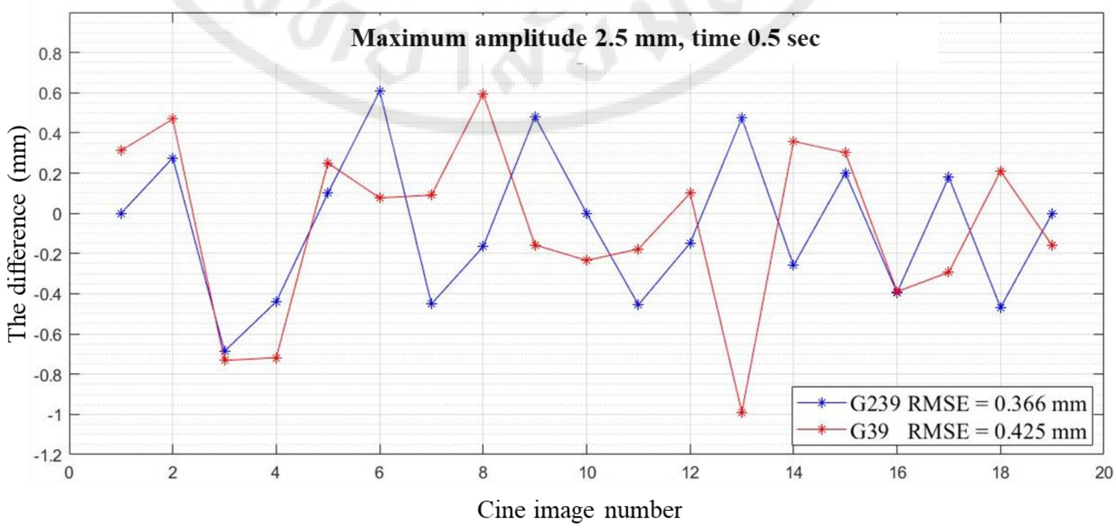

Figure 4.9 The different values between prediction and measurement from the cine images of the phantom with amplitude 2.5 mm and time 0.5 seconds.

Additionally, the phantom motion was an increased range of amplitude to 5 mm with time 1 second. The maximum difference values are -0.714 mm for gantry angle 239º and -0.807 mm for gantry angle 39º. The RSME in gantry angle 239º and 39º are 0.385 mm and 0.395 mm, respectively, as shown in Figure 4.18 and Figure 4.11.

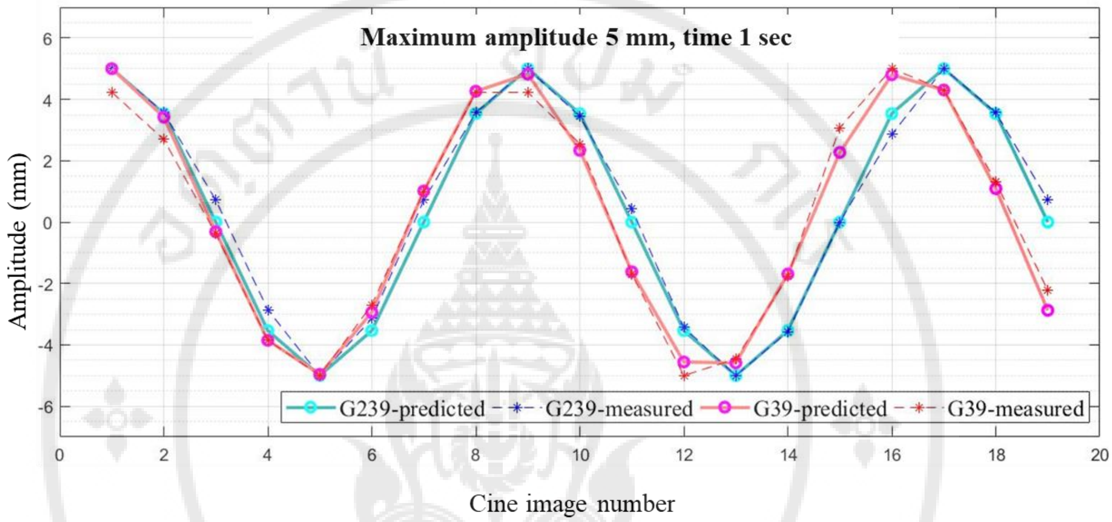

Figure 4.10 Testing accuracy from the cine images of phantom moving with amplitude 5 mm and time 1 second in gantry angle 239º and 39º.

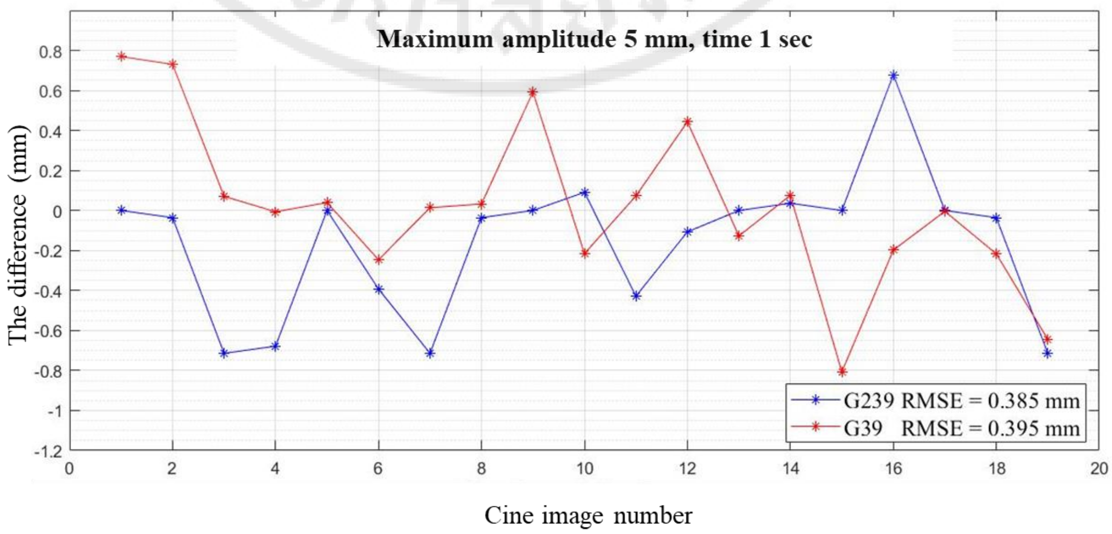

Figure 4.11 The different values between prediction and measurement from the cine images of the phantom with amplitude 5 mm and time 1 second.

B. Capability test

All eight series of cine imaging were used for assessing the capability of the DIBH instability assessment algorithm by introduced an error to images that were divided into three scenarios consist of simulated the blurring images, added Gaussian noise, and salt and pepper noise. The result is shown in Table 4.2.

Table 4.2 The testing capability of the assessment tool.

GROUP	Maximum difference (mm)			RMSE (mm)		
	PSF	Gaussian noise	Salt and pepper	PSF	Gaussian noise	Salt and pepper
1	0.30	14.10	55.20	0.25	3.50	32.87
2	0.50	14.10	34.50	0.26	4.57	28.60
3	0.30	35.60	35.80	0.21	28.27	32.46
4	0.30	36.90	36.30	0.25	30.04	30.47
5	-1.40	-35.80	-41.80	0.59	23.42	30.66
6	0.80	-44.70	-73.20	0.40	22.48	27.79
7	-1.30	37.20	-35.80	0.57	20.18	18.90
8	-1.00	-44.10	-54.60	0.31	23.61	20.62
Absolute mean difference	0.74	32.81	45.90	0.36	19.51	27.80
SD	0.46	12.08	13.89	0.15	10.06	5.27

For scenario1, to simulate the blurring images by vary PSF—the results of phantom move with amplitude 0 mm and time 0 second found that the maximum difference is -1.4 mm and the maximum RMSE is 0.59 mm in the image of gantry angle 39º with PSF 15,15 as shown in Figure 4.12.

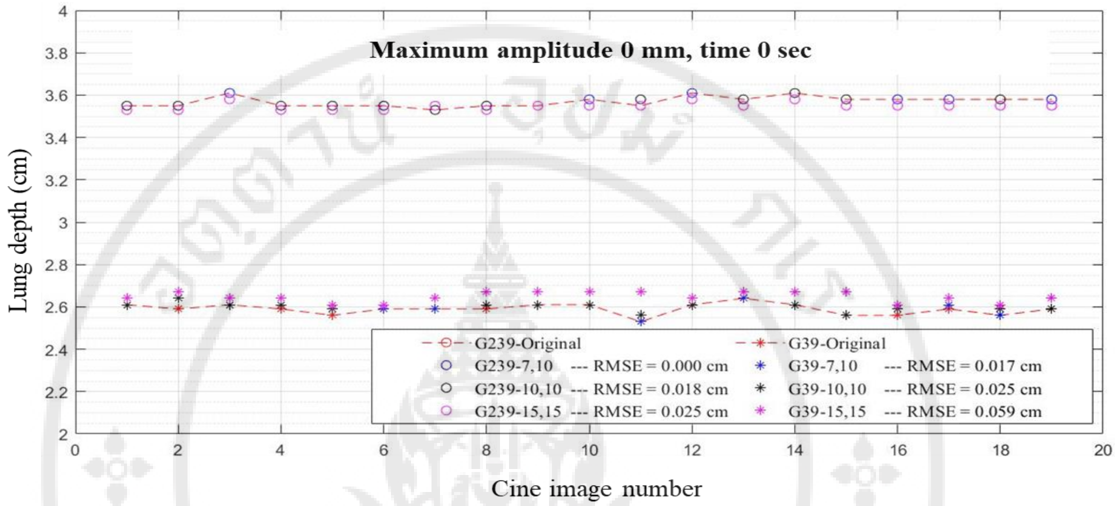

Figure 4.12 Testing capability by added blurring in cine images of phantom move with amplitude 0 mm and time 0 second in gantry angle 239º and 39º.

For phantom move with amplitude 2.5 mm and time 1 second, the maximum difference and RMSE are 0.8 mm and 0.40 mm, respectively, in the image of gantry angle 39º with PSF 10, 10 as presented in Figure 4.13.

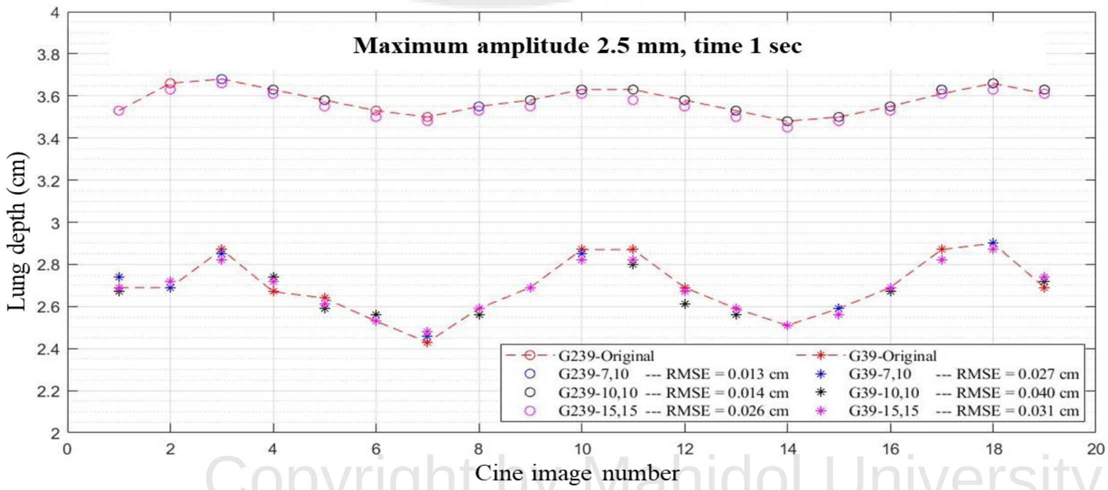

Figure 4.13 Testing capability by added blurring in cine images of phantom move with amplitude 2.5 mm and time 1 second in gantry angle 239º and 39º.

For phantom move with amplitude 2.5 mm and time 0.5 seconds, the maximum difference is -1.3 mm with PSF 7,10, and the maximum RMSE is 0.57 mm in gantry angle 39º with PSF 10,10 and 15,15 in gantry 39º as shown in Figure 4.14.

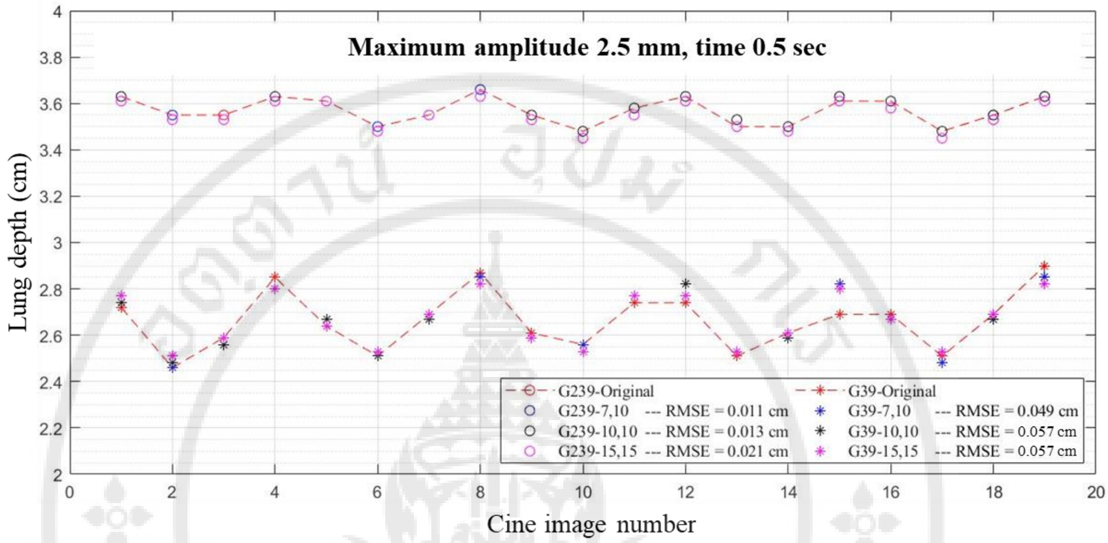

Figure 4.14 Testing capability by added blurring in cine images of phantom move with amplitude 2.5 mm and time 0.5 seconds in gantry angle 239º and 39º.

The last motion of blurring the image, The maximum difference is -1 mm, and the maximum RMSE is 0.31 mm in the image of gantry 39º with PSF 15,15, as shown in Figure 4.15.

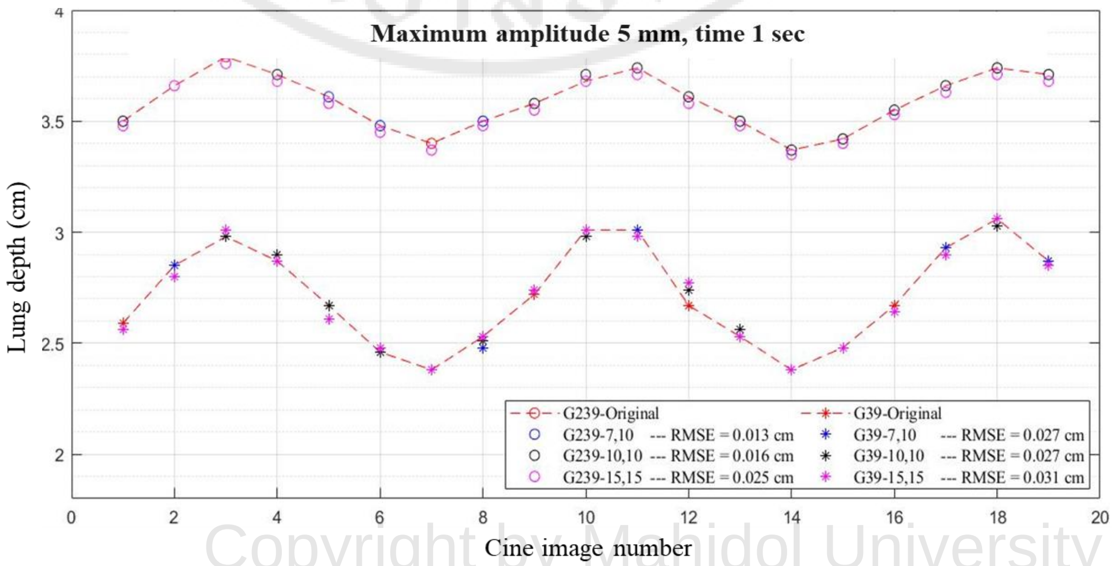

Figure 4.15 Testing capability by added blurring in cine images of phantom move with amplitude 5 mm and time 1 second in gantry angle 239º and 39º.

Scenario 2, Gaussian noise was introduced to the image. The outcomes, as presented in Figure 4.16 -4.19. The results show that in house programs can reduce noise vary the poor. The range of RMSE is 0. 21 – 30.04 mm. Moreover, the different maximum value is -44.7 mm.

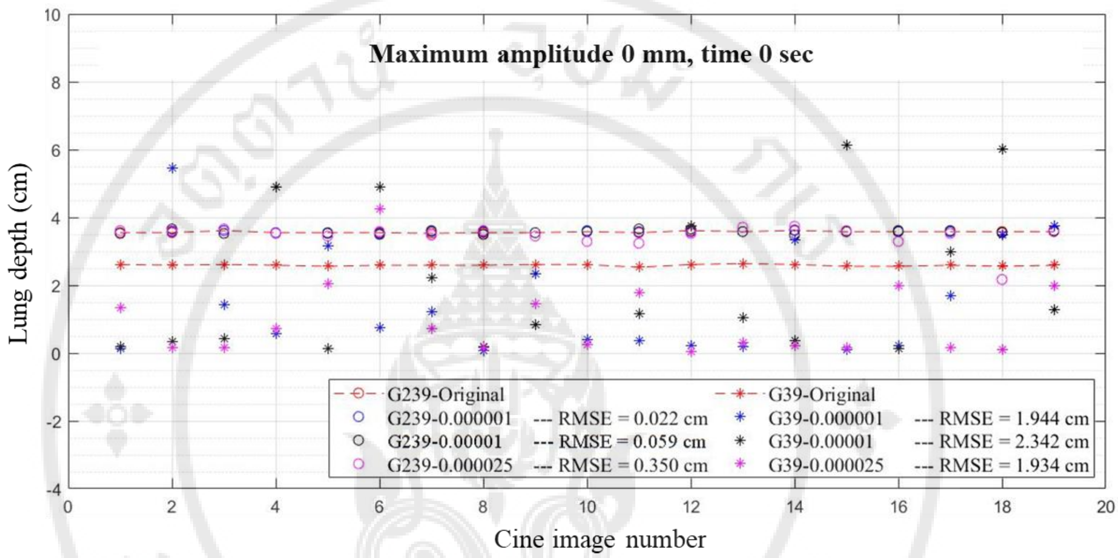

Figure 4.16 Testing capability by added Gaussian noise in cine images of phantom move with amplitude 0 mm and time 0 second in gantry angle 239º and 39º

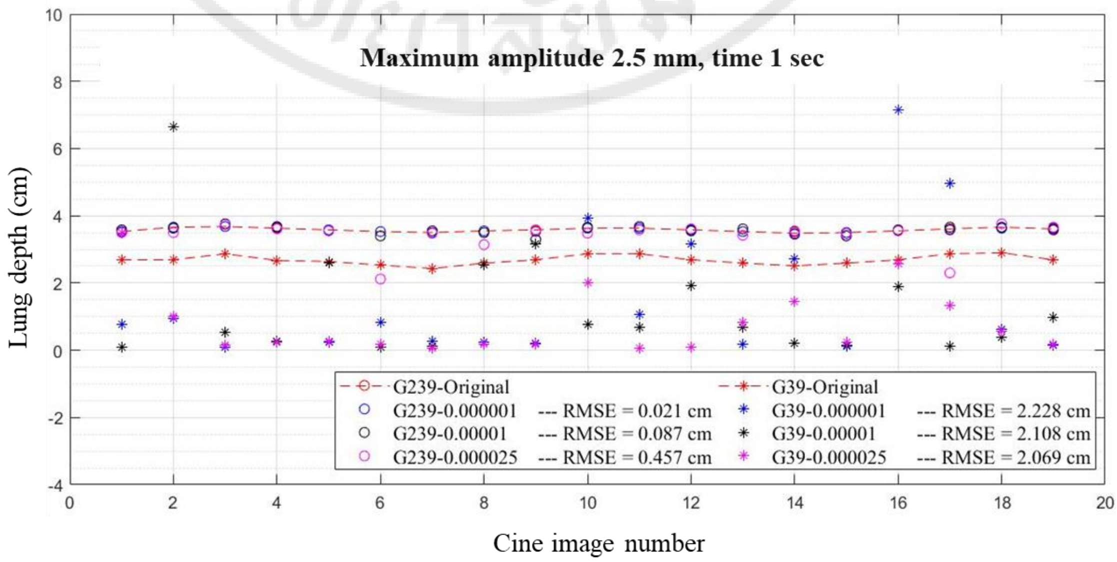

Figure 4.17 Testing capability by added Gaussian noise in cine images of phantom move with amplitude 2.5 mm and time 1 second in gantry angle 239º and 39º

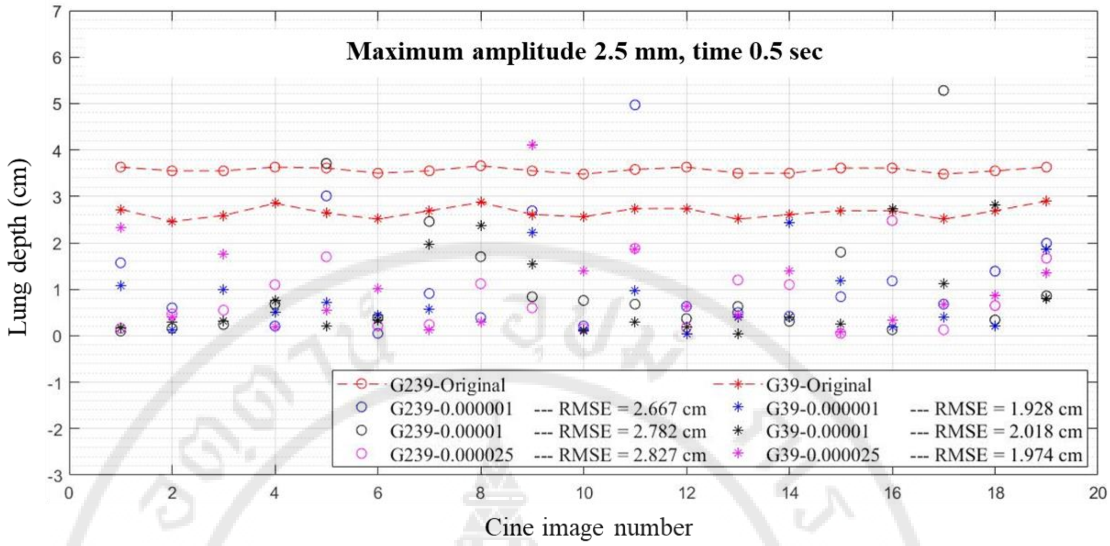

Figure 4.18 Testing capability by added Gaussian noise in cine images of phantom move with amplitude 2.5 mm and time 0.5 second in gantry angle 239º and 39º

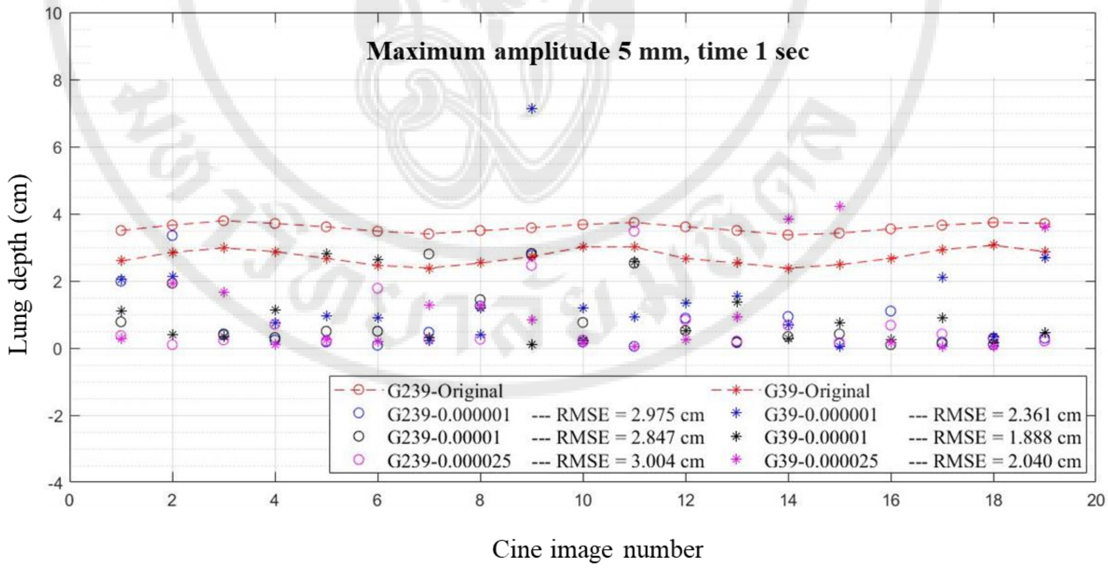

Figure 4.19 The result of test capability by added Gaussian noise in the image of phantom move with amplitude 5 mm and time 1 second.

Last, scenario 3 to simulate the noise images by added salt and pepper noise**.** The outcomes, as presented in Figure 4.20 - Figure 4.23. The results also can reduce noise very poorly. The range of RMSE is 9.49 – 32.46 mm and the maximum difference is -73.2 mm.

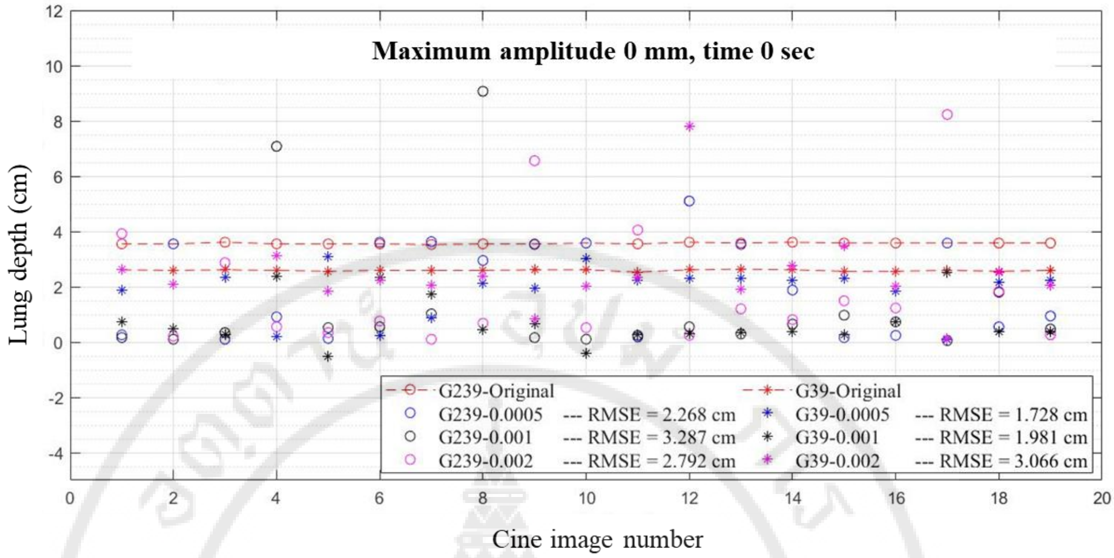

Figure 4.20 Testing capability by added salt and pepper noise in cine images of phantom move with amplitude 0 mm and time 0 second in gantry angle 239º and 39º

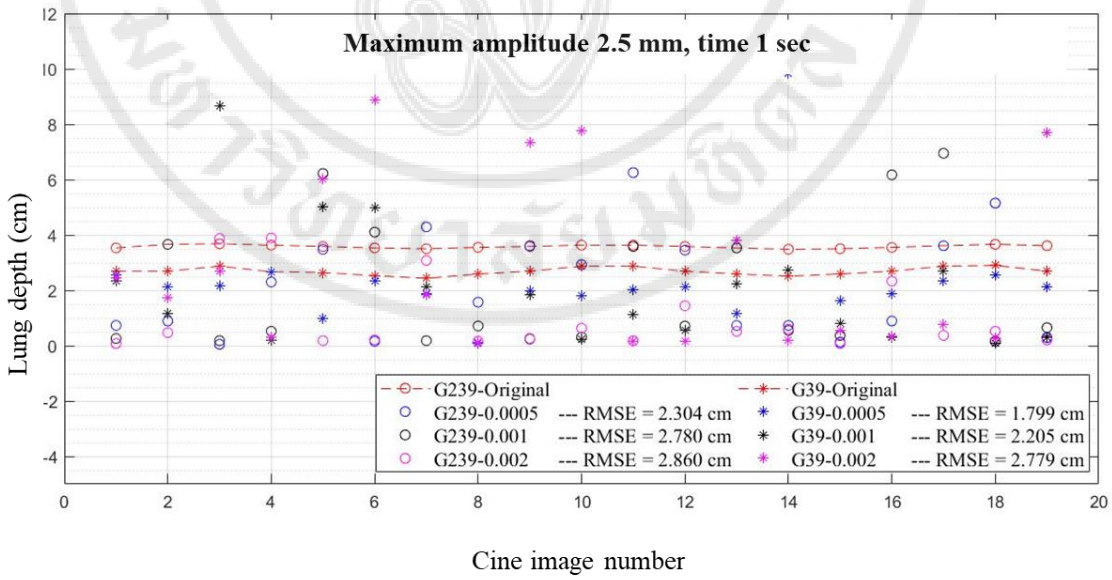

Figure 4.21 Testing capability by added salt and pepper noise in cine images of phantom move with amplitude 2.5 mm and time 1 second in gantry angle 239º and 39º

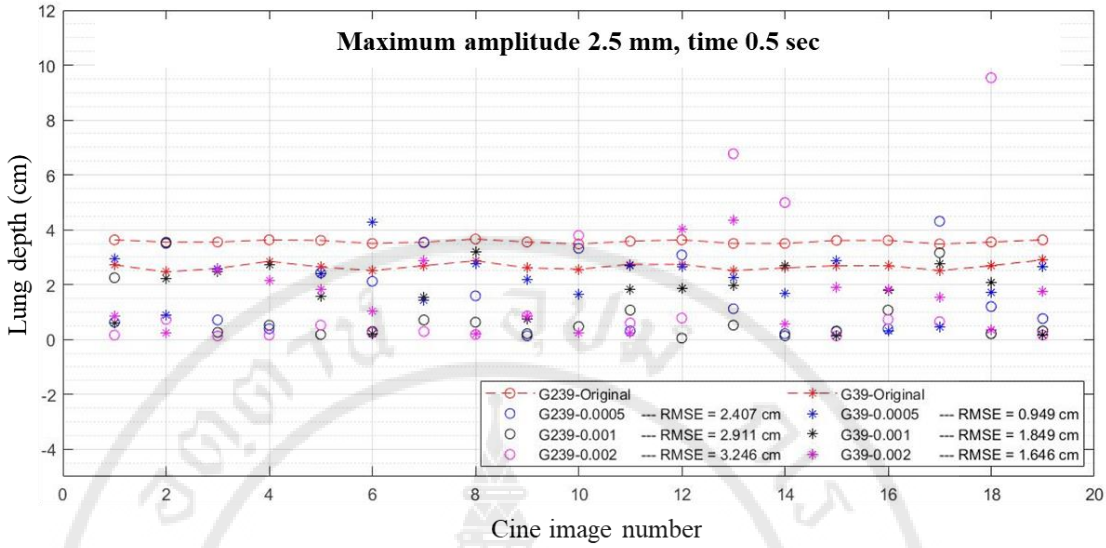

Figure 4.22 Testing capability by added salt and pepper noise in cine images of phantom move with amplitude 2.5 mm and time 0.5 second in gantry angle 239º and 39º

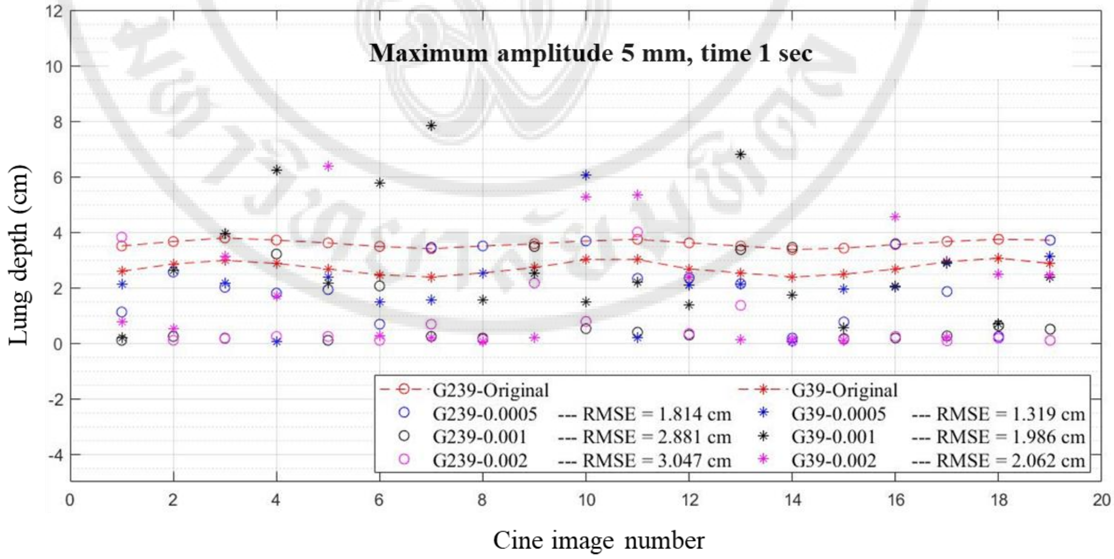

Figure 4.23 Testing capability by added salt and pepper noise in cine images of phantom move with amplitude 5 mm and time 1 second in gantry angle 239º and 39º

C. Applying in clinical

The cine images of the patient were analyzed in this study consist of 3 patients that have a different character. The first, the patient, has large breast conservative surgery. Second, breast mastectomy is both with and without bolus treatment planning. The last, the small breast conservative surgery. The results of detecting the stability of the DIBH technique as shown in Figure 4.25.

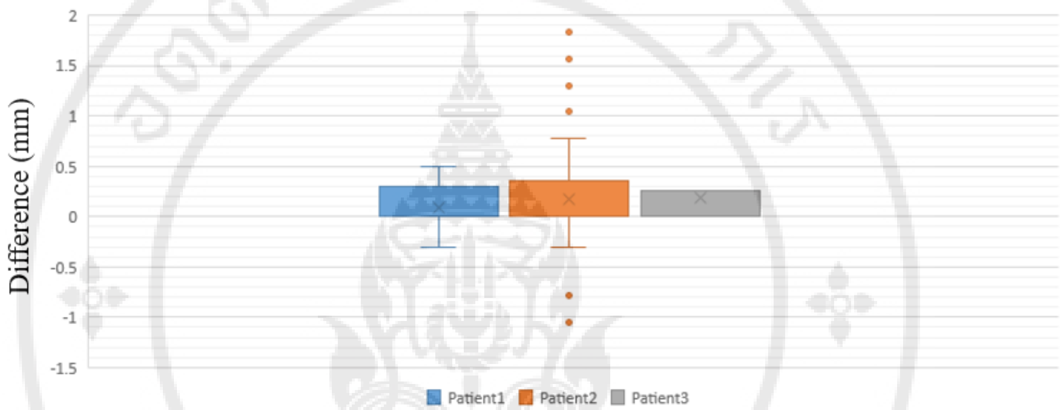

Figure 4.24 The difference in measuring the stability of breath-hold in patients who treat with the DIBH technique.

CHAPTER V
DISCUSSIONS

The cine images of the DIBH technique were acquired during beam delivery and were analyzed the stability of the BH during treatment by using in house MATLAB program with Canny's edge detection algorithm. It can reduce the number of false edges and create a better starting point for a farther process like Hough Transformation due to 2 steps. The first, non-maximum suppression process; the image is scanned along the edge direction. It discards any pixel value that is not considered to be an edge, which will result in a thin line in the output image. Moreover, the hysteresis process - weak edges were linked with sharp edges that were included in the output image [55, 56].

Before using in clinical, the in house MATLAB was tested the performance from Rando phantom and MotionSim XY/4D by varying amplitude and time. For testing accuracy, the maximum difference from prediction is -0.996±0.246 mm in gantry angle 39º with amplitude 2.5 mm and time 1 second. This error is according to the study by Jensen [10] using MATLAB algorithms to apply with the Canny filter with a reported error of 1.2–1.5 mm. The uncertainty of this in house program may be caused by a low frame rate of cine image that is 2 frames per second. Using a low frame rate, it may lead to a lack of image motion as the study by Yip [64] motion blurring in the images with frame rates below 4.29 Hz can significantly reduce the accuracy. However, using a high frame rate, it wasted space for data storage that causing slow processing and may incur additional costs. In addition, this in house was applied with 3 filters consisting of Gaussian filter, median filter, and Wiener filter that was resulted in degrading the information of images. The canny algorithm used Gaussian smoothing- the location of the edges might be off, and blur leads to harder to detect. Also, the corner pixels look in the wrong directions for their neighbors, leaving open-ended edges, and missing junctions. Moreover, the EPID maybe occur a ghosting effect as the study by Alshanqity [65]. The effect of ghosting is present at the beginning of irradiation delivery established as a decreased total integrated signal per MU at low dose range (1–10 MU) and due to hardware limitations. The last, the distance of lung depth was measured from only one line profile, which will result in a systematic error from a subpixel error.

Furthermore, the capability testing consists of blurring and noise images; this in house program can detect the blurring image quite high accuracy due to Wiener filter with the maximum RMSE is 0.59 mm and the maximum difference is 1.4 mm. The Wiener filter is the MSE optimal stationary linear filter for images degraded by additive noise and blurring. Normally, the blurring image can occur from movement during the image capture process. However, in the noise image found that this program cannot detect accuracy with a maximum difference of 73.2 mm for 'salt and pepper noise' and 44.1 mm for 'Gaussian noise'. Thirumavalavan [66] studied the performance under noisy environment and found that the Canny edge is distorted and deviate widely from the true edges with Gaussian and impulse noises. For the salt and pepper noise is a random pixel being set to black or white such as dead pixels from EPID that can occur from the electronic part. It can be found rarely owing to calibrated regularly. For Gaussian noise, it is statistical noise that is scattered from EPID, patient, and treatment head. In this study, setting too many noises that effect to program are unable to get rid of it.

After the test program from the phantom, it was appied in the clinical usage. That analyzed the images data from 3 patients who treated with the DIBH technique. The standard gating window of 2 mm was used for all patients [12]. Each day in the same patient will have different amplitudes, which will depend on the position of the patient. As a result, an offline review of cine images was analyzed and seem to be quite stable result of BH. However, it has just an image over a limitation of 2 mm. Manual hold RT may cause readability over 2 mm if the patient breathes more than the setting of amplitude, which may be pressed delay time. Alternatively, it may be caused by the error of the program at almost 1 mm. Nevertheless, this experiment cannot use DRR for reference images but use the first cine image as a reference image due to the setting amplitude by the radiation therapist. The study by Jensen [10], also uses the first image of each beam to be the reference image. Thomsen [11] and Lutz [12] use DRR as the reference image by manually registering with portal images. The limitation of this program only use in the tangential breast without the SPC field because the image acquires full-field so the whole lune can be imaged but if the SPC field also included, only the upper lung can be imaged.

Many researchers have studied and developed strategies to minimize the mean heart dose, which may impact the patient's long term complications for left breast cancer radiotherapy [4-6]. DIBH is considered one of the effective techniques that able to reduce cardiac and lung doses [7-9]. Part of our studies, five patients of left breast cancer were randomly selected to simulate the effect of radiation towards the tolerance level determination. Our finding shows the maximum MHD with 9.60±2.45 Gy of motion 15 mm. However, in the case of motion -15 mm, the coverage of PTV was reduced to 5.64%, with the reference criteria for cut off based on Darby [5]. This study uses the MHD cut off value with 7 Gy for determining the tolerance level to switch from DIBH to FB delivery in this study. The tolerance level to switch from DIBH to FB delivery should be within ±11.00 mm in AP direction from the reference position. Besides, this should be considered from the MHD received from each patient. If the patient received MHD near 7 Gy should be more careful about the tolerance level. Furthermore, the use of treatment techniques is also affected to MHD. For an advance technique such as IMRT is to receive heart dose more than the 3DCRT technique.

However, there are no studies to date that were conducted on the impact on MHD in unstable BH cases; this study by simulation of motion from RaySearch may be the starting point for further studies.

CHAPTER VI
CONCLUSION

The cine EPID images were used to measure the stability of DIBH by using in house MATLAB program with Canny's edge detection algorithm. The evaluation of the accuracy of the in house MATLAB assessment tool from the phantom found that the maximum difference from prediction is less than 1 mm. Also, the in house MATLAB program has good repeatability. Testing capability with added blurring in the image, this program can be analyzed quite accurately with a maximum difference of 1.4 mm but reduce noise very poorly with a maximum difference of 73.2 mm. However, the in house MATLAB program was used to detect the stability of breath-hold in patients which found that the results correspond amplitude setting from the treatment room. The in-house automated MATLAB program with EPID based is suitable for clinical treatment with a millimeter error. The system of automated EPID-based DIBH instability evaluation tool was developed and can be implemented as an additional trigger to assess the patient's breath-hold capability towards efficient treatment delivery and the tolerance level to switch from DIBH to FB delivery should be within ±11.00 mm in AP direction from the reference position.

REFERENCES

1. World Health Organization. Latest global cancer data: Cancer burden rises to 18.1million new cases and 9.6 million cancer deaths in 2018 [Internet]. 2018 [cited 2018 Dec 5]. Available from: https://www.iarc.fr/wp-content/uploads/2018/09/pr263_E.pdf
2. Miller, K. D., et al. "Cancer treatment and survivorship statistics, 2019." CA: a cancer journal for clinicians 69.5 (2019): 363.
3. Latty D, Stuart KE, Wang W, Ahern V. Review of deep inspiration breath-hold techniques for the treatment of breast cancer. Journal of medical radiation sciences. 2015;62(1):74-81.
4. Taylor CW, Nisbet A, McGale P, Darby SC. Cardiac exposures in breast cancer radiotherapy: 1950s–1990s. International Journal of Radiation Oncology* Biology* Physics. 2007;69(5):1484-95.
5. Darby SC, Ewertz M, McGale P, Bennet AM, Blom-Goldman U, Bronnum D, et al. Risk of ischemic heart disease in women after radiotherapy for breast cancer. N Engl J Med. 2013;368(11):987-98.
6. Beaton L, Bergman A, Nichol A, Aparicio M, Wong G, Gondara L, et al. Cardiac death after breast radiotherapy and the QUANTEC cardiac guidelines. Clinical and Translational Radiation Oncology. 2019;19:39-45.
7. Nissen HD, Appelt AL. Improved heart, lung and target dose with deep inspiration breath hold in a large clinical series of breast cancer patients. Radiotherapy and Oncology. 2013;106(1):28-32.
8. Sung K, Lee KC, Lee SH, Ahn SH, Lee SH, Choi J. Cardiac dose reduction with breathing adapted radiotherapy using self respiration monitoring system for left-sided breast cancer. Radiation oncology journal. 2014;32(2):84.
9. Bruzzaniti V, Abate A, Pinnarò P, D'Andrea M, Infusino E, Landoni V, et al. Dosimetric and clinical advantages of deep inspiration breath-hold (DIBH) during radiotherapy of breast cancer. Journal of Experimental & Clinical Cancer Research. 2013;32(1):88.

10. Jensen C, Urribarri J, Cail D, Rottmann J, Mishra P, Lingos T, et al. Cine EPID evaluation of two non-commercial techniques for DIBH. Medical physics. 2014;41(2).
11. Thomsen MS, Harrov U, Fledelius W, Poulsen PR. Inter-and intra-fraction geometric errors in daily image-guided radiotherapy of free-breathing breast cancer patients measured with continuous portal imaging. Acta Oncologica. 2014;53(6):802-8.
12. Lutz CM, Poulsen PR, Fledelius W, Offersen BV, Thomsen MS. Setup error and motion during deep inspiration breath-hold breast radiotherapy measured with continuous portal imaging. Acta Oncologica. 2016;55(2):193-200.
13. Barrett A, Morris S, Dobbs J, Roques T. Practical Radiotherapy Planning Fourth Edition: CRC Press; 2009.
14. Bartlett FR, Colgan RM, Carr K, Donovan EM, McNair HA, Locke I, et al. The UK HeartSpare Study: randomised evaluation of voluntary deep-inspiratory breath-hold in women undergoing breast radiotherapy. Radiotherapy and Oncology. 2013;108(2):242-7.
15. Haydaroglu A, Ozyigit G. Principles and practice of modern radiotherapy techniques in breast cancer: Springer Science & Business Media; 2012.
16. Joshi SC, Khan FA, Pant I, Shukla AN. Role of Radiotherapy in Early Breast Cancer: An Overview. International journal of health sciences. 2007;1(2):259.
17. Radiation therapy for breast cancer: Mayo clinic; [cited 2018 Dec 12]. Available from: https://www.mayoclinic.org/tests-procedures/radiation-therapy-for-breast-cancer/about/pac-20384940
18. Breast Brachytherapy: Cet center cancer; [cited 2018 Dec 12]. Available from: http://www.cetmc.com/breasthdrbrachytherapy.html
19. Skowronek J, Chicheł A. Brachytherapy in breast cancer: an effective alternative. Przeglad menopauzalny= Menopause review. 2014;13(1):48.
20. Herron B, Herron A, Howell K, Chin D, Roads L. A review of radiation therapy's role in early-stage breast cancer and an introduction to electronic brachytherapy. Cancer Treatment-Conventional and Innovative Approaches: IntechOpen; 2013.

21. Smith BD, Bellon JR, Blitzblau R, Freedman G, Haffty B, Hahn C, et al. Radiation therapy for the whole breast: Executive summary of an American Society for Radiation Oncology (ASTRO) evidence-based guideline. Pract Radiat Oncol. 2018;8(3):145-52.
22. Lo Y-C, Yasuda G, Fitzgerald TJ, Urie MM. Intensity modulation for breast treatment using static multi-leaf collimators. International Journal of Radiation Oncology* Biology* Physics. 2000;46(1):187-94.
23. Michalski A, Atyeo J, Cox J, Rinks M. Inter-and intra-fraction motion during radiation therapy to the whole breast in the supine position: a systematic review. Journal of medical imaging and radiation oncology. 2012;56(5):499-509.
24. Rudra S, Al-Hallaq HA, Feng C, Chmura SJ, Hasan Y. Effect of RTOG breast/chest wall guidelines on dose-volume histogram parameters. Journal of applied clinical medical physics. 2014;15(2):127-37.
25. Wiersma RD, Liu X. A concept study on real-time adaptive radiation therapy optimization. arXiv preprint arXiv:181103665. 2018.
26. http://www.rtog.org/ClinicalTrials/ProtocolTable.aspx (2011). Accessed 20/11/2011.
27. Dogan N, Cuttino L, Lloyd R, Bump EA, Arthur DW. Optimized dose coverage of regional lymph nodes in breast cancer: the role of intensity-modulated radiotherapy. International Journal of Radiation Oncology* Biology* Physics. 2007;68(4):1238-50.
28. Keall PJ, Mageras GS, Balter JM, Emery RS, Forster KM, Jiang SB, et al. The management of respiratory motion in radiation oncology report of AAPM Task Group 76 a. Medical physics. 2006;33(10):3874-900.
29. What is a normal respiratory rate?: Medical News Today; [cited 2019 Dec 22]. Available from: https://www.medicalnewstoday.com/articles/324409
30. Jensen CA, Acosta Roa AM, Lund J-Å, Frengen J. Intrafractional baseline drift during free breathing breast cancer radiation therapy. Acta Oncologica. 2017;56(6):867-73.

31. Tezcanli EK, Goksel EO, Yildiz E, Garipagaoglu M, Şenkesen Ö, Kucucuk H, et al. Does radiotherapy planning without breath control compensate intra-fraction

heart and its compartments' movement? Breast cancer research and treatment. 2011;126(1):85-92.

32. Schubert LK, Gondi V, Sengbusch E, Westerly DC, Soisson ET, Paliwal BR, et al. Dosimetric comparison of left-sided whole breast irradiation with 3DCRT, forward-planned IMRT, inverse-planned IMRT, helical tomotherapy, and topotherapy. Radiotherapy and Oncology. 2011;100(2):241-6.
33. Comsa D, Barnett E, Le K, Mohamoud G, Zaremski D, Fenkell L, et al. Introduction of moderate deep inspiration breath hold for radiation therapy of left breast: initial experience of a regional cancer center. Practical radiation oncology. 2014;4(5):298-305.
34. Mast ME, van Kempen-Harteveld L, Heijenbrok MW, Kalidien Y, Rozema H, Jansen WPA, et al. Left-sided breast cancer radiotherapy with and without breath-hold: Does IMRT reduce the cardiac dose even further? Radiotherapy and Oncology. 2013;108(2):248-53.
35. Czeremszyńska B, Drozda S, Górzyński M, Kępka L. Selection of patients with left breast cancer for deep-inspiration breath-hold radiotherapy technique: Results of a prospective study. Reports of Practical Oncology & Radiotherapy. 2017;22(5):341-8.
36. Bartlett FR, Donovan EM, McNair HA, Corsini LA, Colgan RM, Evans PM, et al. The UK HeartSpare Study (Stage II): multicentre evaluation of a voluntary breath-hold technique in patients receiving breast radiotherapy. Clinical Oncology. 2017;29(3):e51-e6.
37. Bartlett FR, Colgan RM, Donovan EM, McNair HA, Carr K, Evans PM, et al. The UK HeartSpare Study (Stage IB): randomised comparison of a voluntary breath-hold technique and prone radiotherapy after breast conserving surgery. Radiotherapy and Oncology. 2014;114(1):66-72.
38. Hjelstuen MHB, Mjaaland I, Vikström J, Dybvik KI. Radiation during deep inspiration allows loco-regional treatment of left breast and axillary-, supraclavicular-and internal mammary lymph nodes without compromising target coverage or dose restrictions to organs at risk. Acta Oncologica. 2012;51(3):333-44.

39. Estoesta RP, Attwood L, Naehrig D, Claridge-Mackonis E, Odgers D, Martin D, et al. Assessment of voluntary deep inspiration breath-hold with CINE imaging for breast radiotherapy. Journal of medical imaging and radiation oncology. 2017;61(5):689-94.

40. Boda-Heggemann J, Knopf A-C, Simeonova-Chergou A, Wertz H, Stieler F, Jahnke A, et al. Deep inspiration breath hold—based radiation therapy: a clinical review. International Journal of Radiation Oncology* Biology* Physics. 2016;94(3):478-92.

41. Cole AJ, Hanna GG, Jain S, O'Sullivan JM. Motion management for radical radiotherapy in non-small cell lung cancer. Clinical Oncology. 2014;26(2):67-80.

42. Bartlett FR, Colgan RM, Donovan EM, Carr K, Landeg S, Clements N, et al. Voluntary breath-hold technique for reducing heart dose in left breast radiotherapy. Journal of visualized experiments: JoVE. 2014(89).

43. Tamburella C, Guibert G, Cruz OS, Weber P, Tsousou P. Volumetric Modulated Arc Therapy (VMAT) combined with deep inspiration breath hold (DIBH) technique for adjuvant irradiation for cancer of the left breast. arXiv preprint arXiv:170606867. 2017.

44. Betgen A, Alderliesten T, Sonke JJ, van Vliet-Vroegindeweij C, Bartelink H, Remeijer P. Assessment of set-up variability during deep inspiration breath hold radiotherapy for breast cancer patients by 3D-surface imaging. Radiother Oncol. 2013;106(2):225-30.

45. Lemanski C, Thariat J, Ampil FL, Bose S, Vock J, Davis R, et al. Image-guided radiotherapy for cardiac sparing in patients with left-sided breast cancer. Front Oncol. 2014;4:257.

46. Topolnjak R, Sonke J-J, Nijkamp J, Rasch C, Minkema D, Remeijer P, et al. Breast patient setup error assessment: comparison of electronic portal image devices and cone-beam computed tomography matching results. International Journal of Radiation Oncology* Biology* Physics. 2010;78(4):1235-43.

47. Image Guided Radiation Therapy: Radiation Oncology Associates; [cited 2018 Dec 12]. Available from: https://www.virginiaradiation.com/treatments/image-guided-radiation-therapy/

48. Kron T, Lee C, Perera F, Yu E. Evaluation of intra-and inter-fraction motion in breast radiotherapy using electronic portal cine imaging. Technology in cancer research & treatment. 2004;3(5):443-9.
49. de Boer HC, van den Bongard DJ, van Asselen B. Automated daily breath hold stability measurements by real-time imaging in radiotherapy of breast cancer. Radiother Oncol. 2016;119(1):61-4.
50. Gierga DP, Riboldi M, Turcotte JC, Sharp GC, Jiang SB, Taghian AG, et al. Comparison of target registration errors for multiple image-guided techniques in accelerated partial breast irradiation. International Journal of Radiation Oncology* Biology* Physics. 2008;70(4):1239-46.
51. Lirette A, Pouliot J, Aubin M, Larochelle M. The role of electronic portal imaging in tangential breast irradiation: a prospective study. Radiotherapy and Oncology. 1995;37(3):241-5.
52. Fein DA, McGee KP, Schultheiss TE, Fowble BL, Hanks GE. Intra-and interfractional reproducibility of tangential breast fields: a prospective on-line portal imaging study. International Journal of Radiation Oncology* Biology* Physics. 1996;34(3):733-40.
53. Joshi M, Vyas A. Comparison of Canny edge detector with Sobel and Prewitt edge detector using different image formats.
54. Patil PHPRP. Image Edge Detection Techniques using MATLAB Simulink. Int J Eng Res Technol. 2014;3(6):2149-53.
55. Chandwadkar R, Dhole S. Comparison of Edge Detection Techniques2013.
56. Maini R, Aggarwal H. Study and comparison of various image edge detection techniques. International journal of image processing (IJIP). 2009;3(1):1-11.
57. Anas R, Elhadi HA, Ali ES. Impact of Edge Detection Algorithms in Medical Image Processing. World Scientific News. 2019;118:129-43.
58. C T Scan Machines: Indiamart; [cited 2019 Dec 25]. Available from: https://www.indiamart.com/radio-graphics/c-t-scan-machines.html#philips-big-bore-rt-ct-scanner

59. Wiersma RD, Mao W, Xing L. Combined kV and MV imaging for real-time tracking of implanted fiducial markers a. Medical physics. 2008;35(4):1191-8.

60. Trilogy® System | Radiation Therapy Technologies: MHP Radiation oncology institute; [cited 2018 Dec 12]. https://mhpradiation.21co.com/radiation-therapy/technologies/varian-trilogy
61. MotionSim XY/4D: @MED; [cited 2018 Dec 12]. https://med.eizojoho.co.jp/soran/product?cid=66&pid=60
62. Kleck JH, Smathers JB, Holly FE, Myers LT. Anthropomorphic radiation therapy phantoms: a quantitative assessment of tissue substitutes. Medical physics. 1990;17(5):800-6.
63. The Alderson Radiation Therapy Phantom; [cited 2018 Dec 12]. Available from: http://rsdphantoms.com/radiation-therapy/the-alderson-radiation-therapy-phantom/
64. Yip S, Rottmann J, Berbeco R. The impact of cine EPID image acquisition frame rate on markerless soft-tissue tracking. Medical physics. 2014;41(6Part1):061702.
65. .Alshanqity M, Duane S, Nisbet A. A simple approach for EPID dosimetric calibration to overcome the effect of image-lag and ghosting. Applied Radiation and Isotopes. 2012;70(7):1154-7.
66. Thirumavalavan S, Jayaraman S. An improved teaching–learning based robust edge detection algorithm for noisy images. Journal of Advanced Research. 2016;7(6):979-89.

APPENDICES

APPENDIX A

Accuracy test of the assessment tool

This results shown the overall difference distribution of accuracy test in each pattern motion of phantom.

(a)

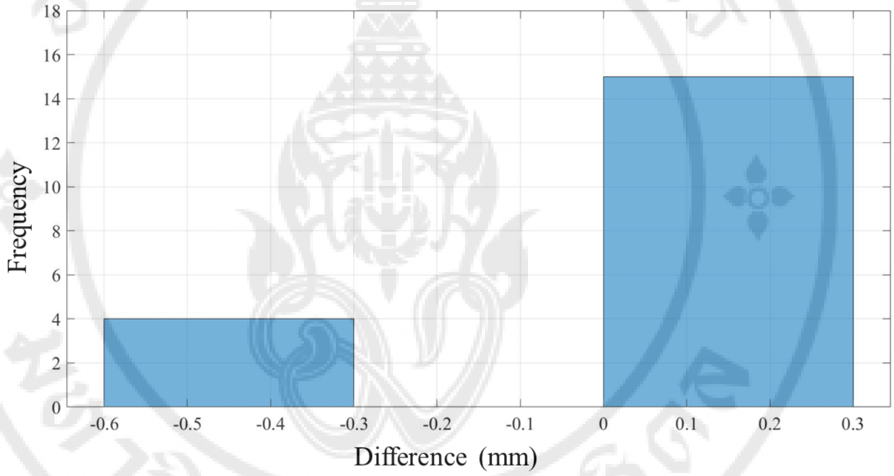

(b)

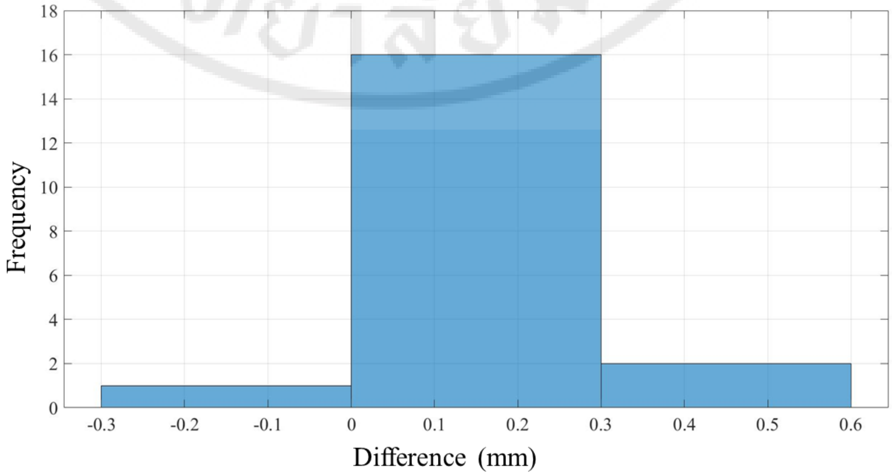

Figure 1A The overall difference distribution of accuracy test in cine images of phantom move with amplitude 0 mm and time 0 second in (a) gantry angle 239º and (b) gantry angle 39º.

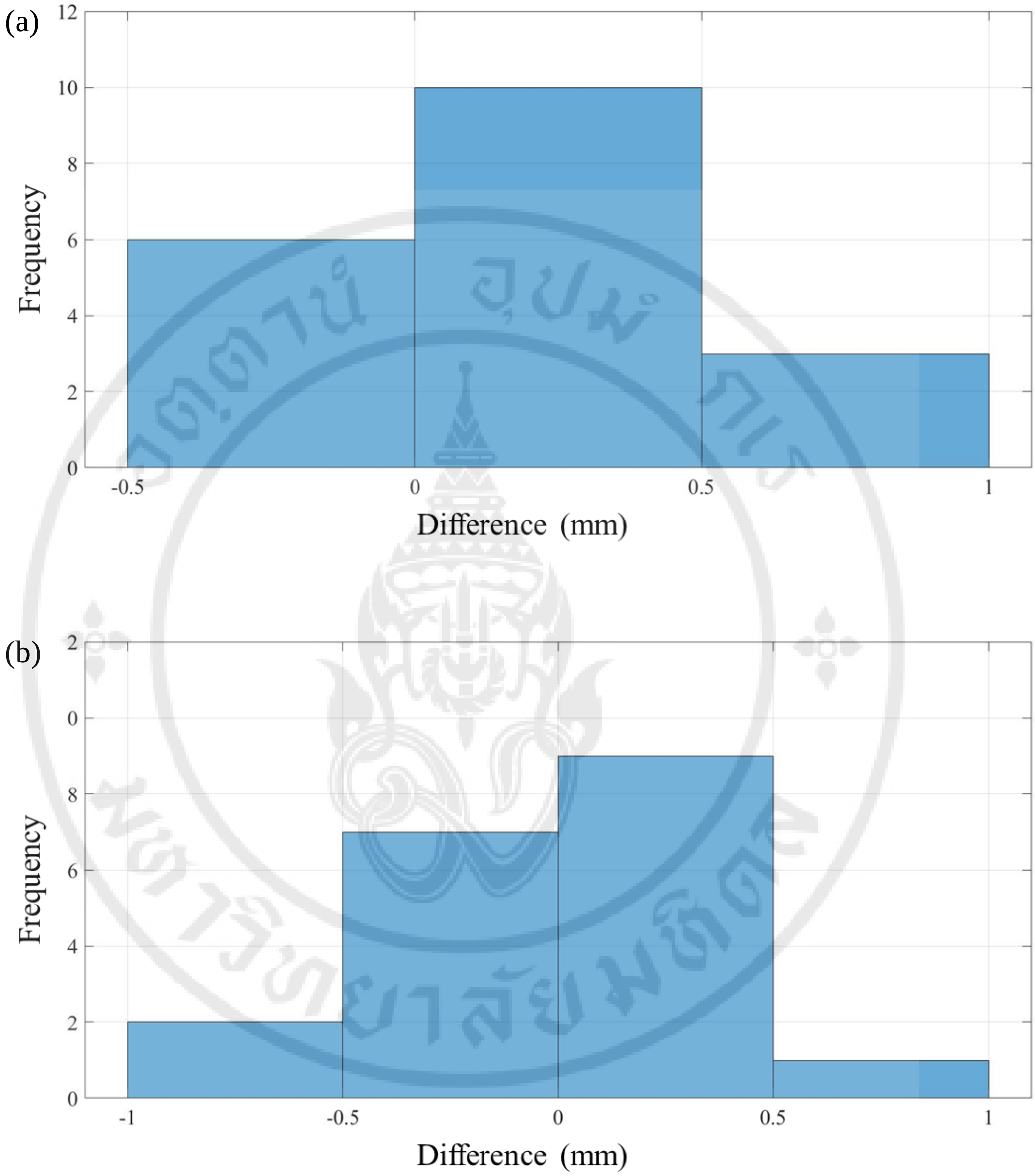

Figure 2A The overall difference distribution of accuracy test in cine images of phantom move with amplitude 2.5 mm and time 1 second in (a) gantry angle 239º and (b) gantry angle 39º.

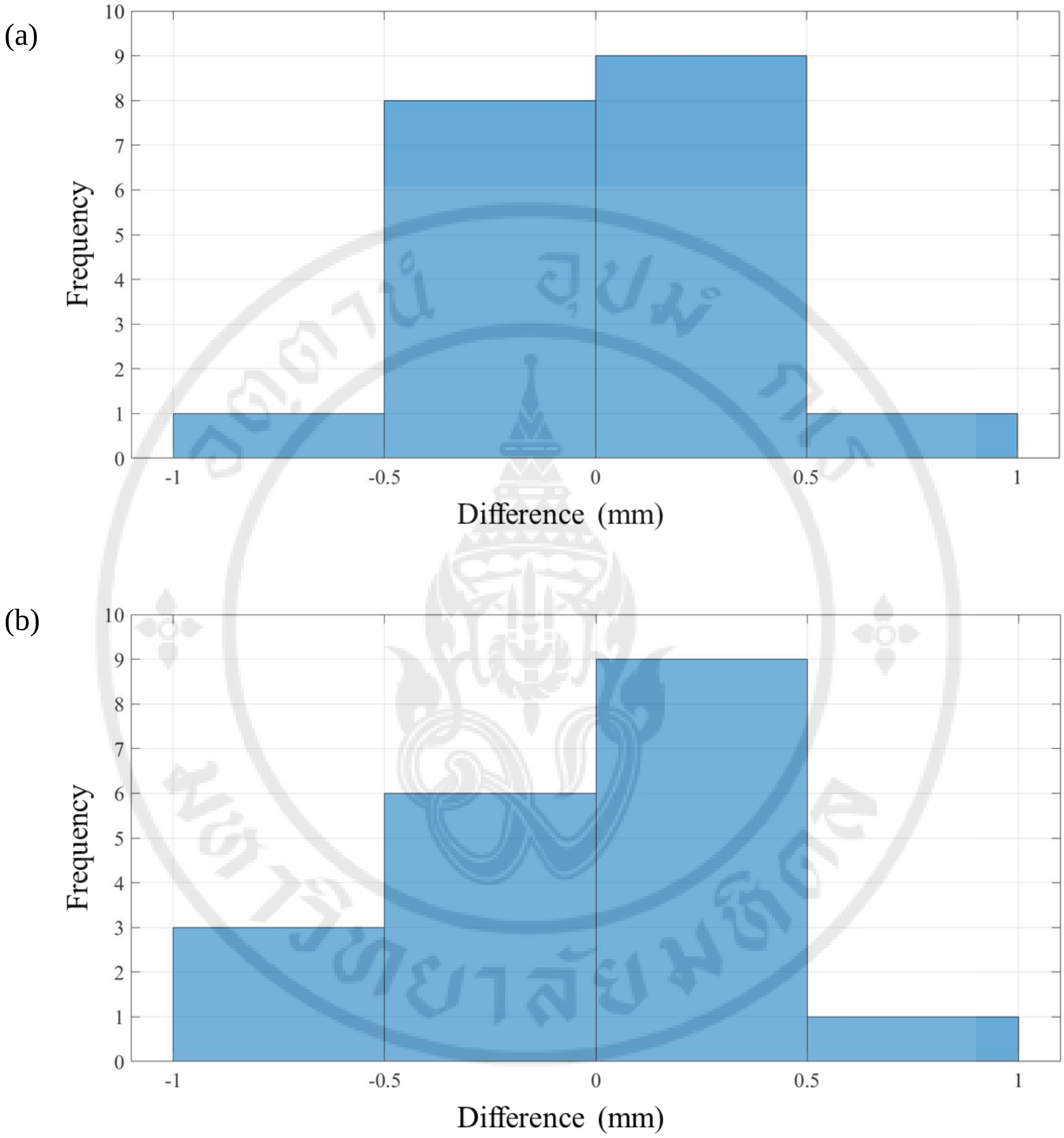

Figure 3A The overall difference distribution of accuracy test in cine images of phantom move with amplitude 2.5 mm and time 0.5 second in (a) gantry angle 239º and (b) gantry angle 39º.

(a)

(b)

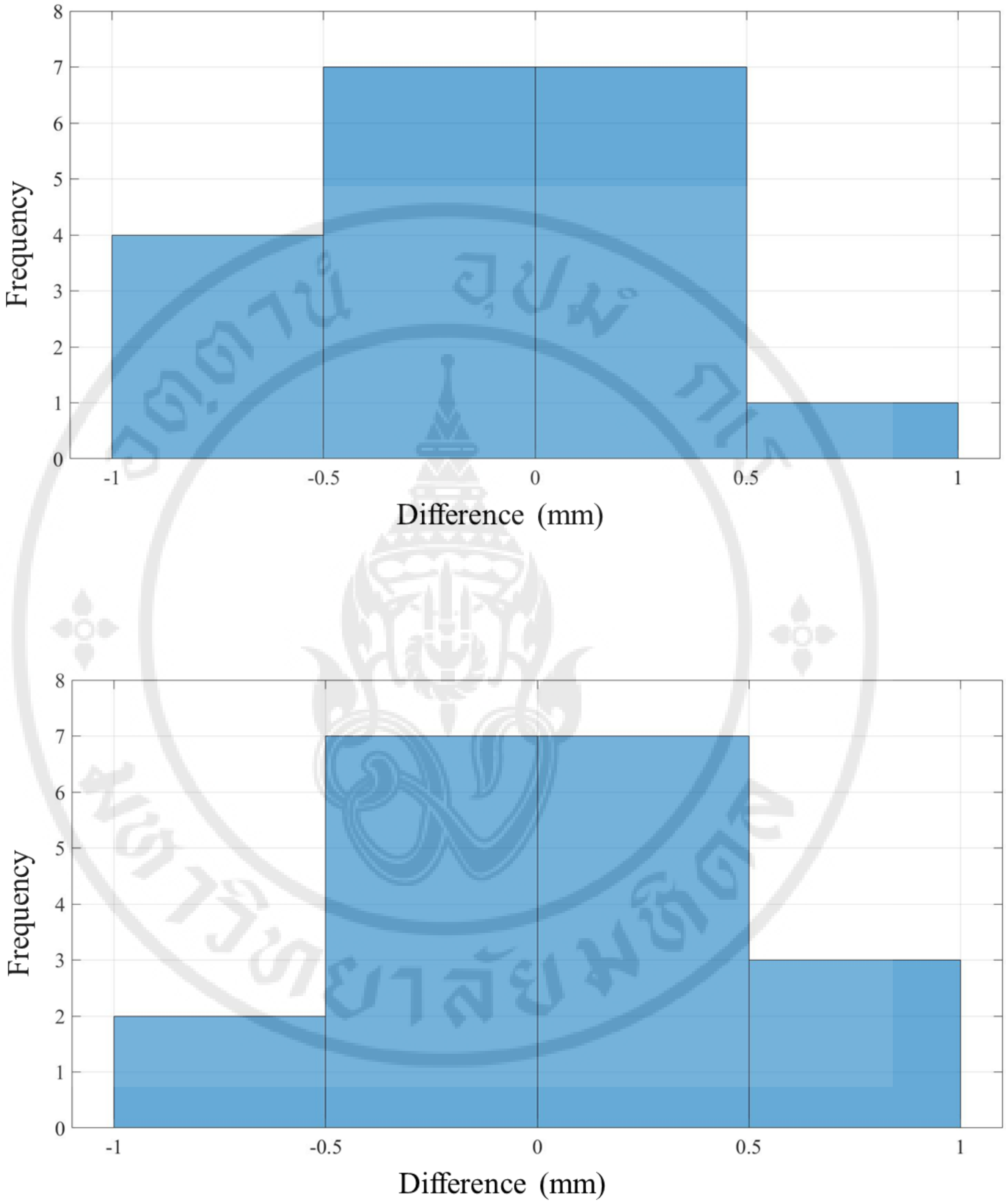

Figure 4A The overall difference distribution of accuracy test in cine images of phantom move with amplitude 5 mm and time 1 second in (a) gantry angle 239º and (b) gantry angle 39º.

APPENDIX B

Capability test of the assessment tool

For scenario1, to simulate the blurring images by vary PSF, this results shown the overall difference distribution of capability test in each pattern motion phantom.

(a)

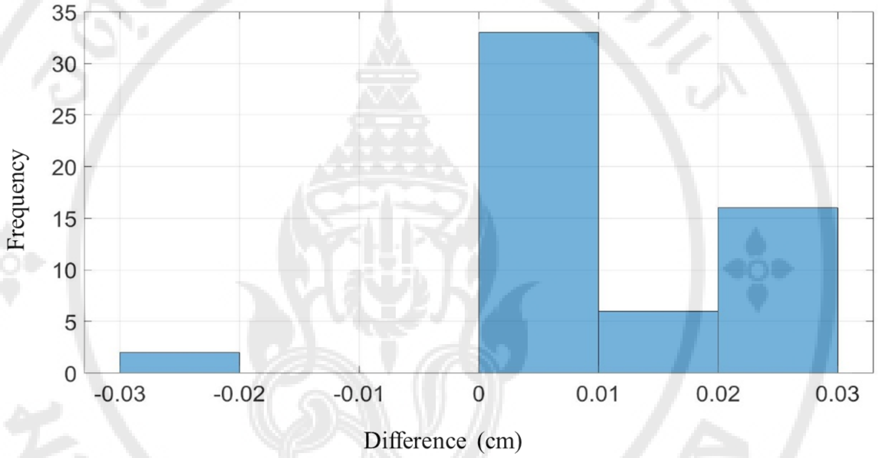

(b)

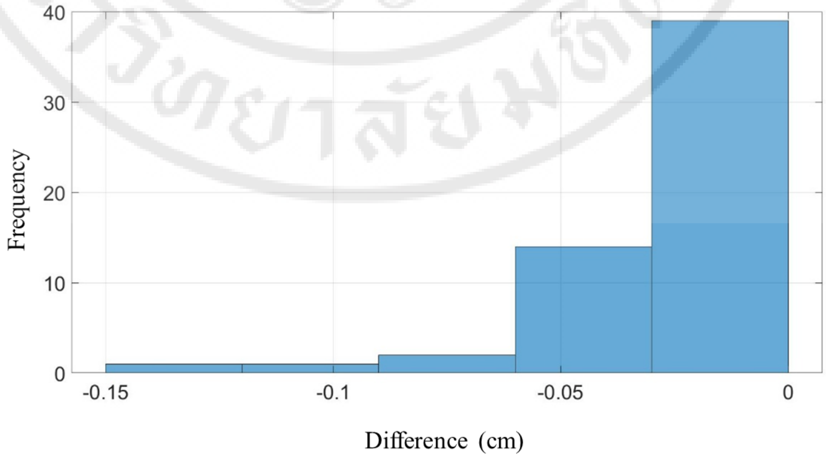

Figure 1B The overall difference distribution of capability test by adding blur in cine images of phantom move with amplitude 0 mm and time 0 second in (a) gantry angle 239º and (b) gantry angle 39º.

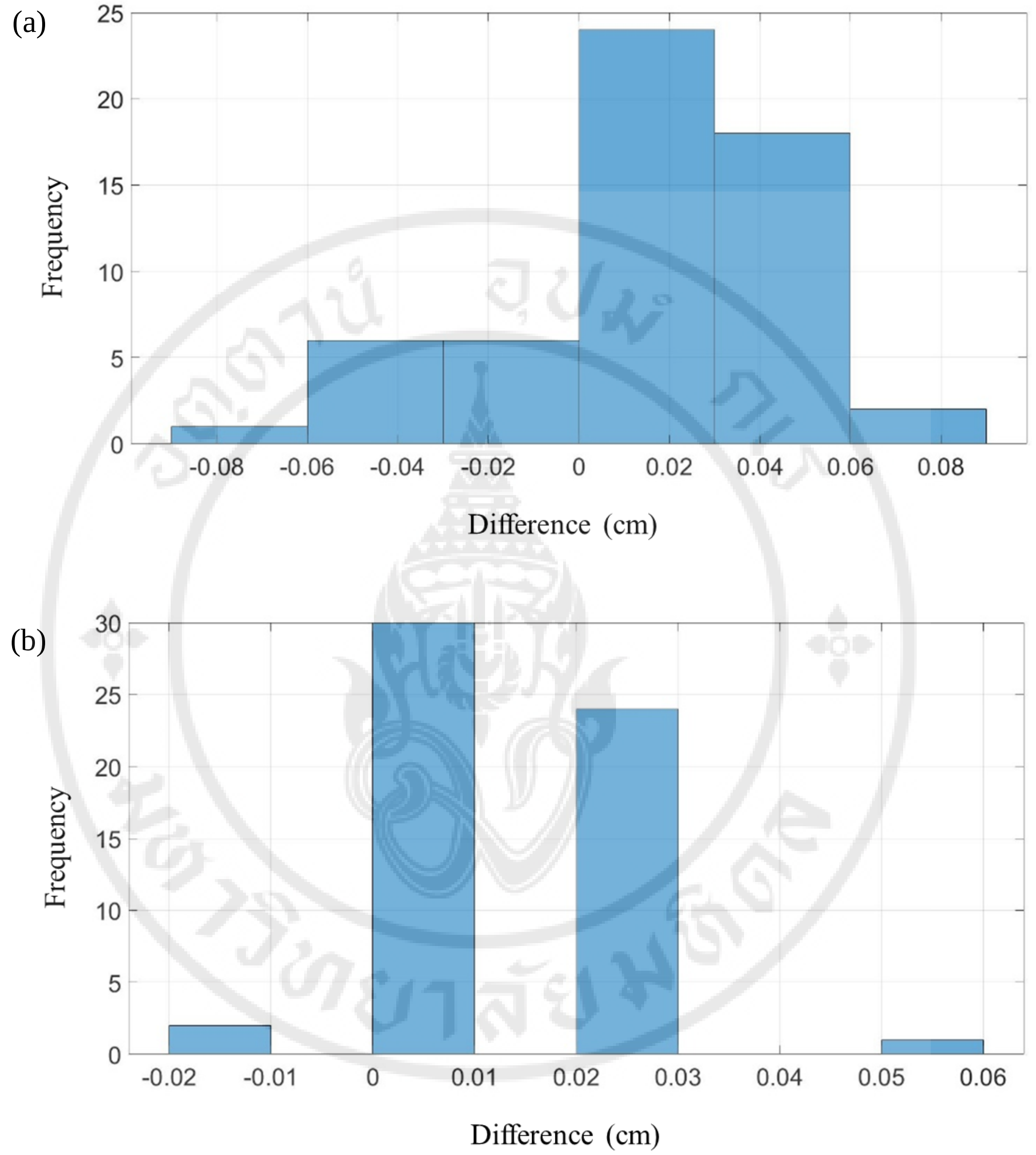

Figure 2B The overall difference distribution of capability test by adding blur in cine images of phantom move with amplitude 2.5 mm and time 1 second in (a) gantry angle 239º and (b) gantry angle 39º.

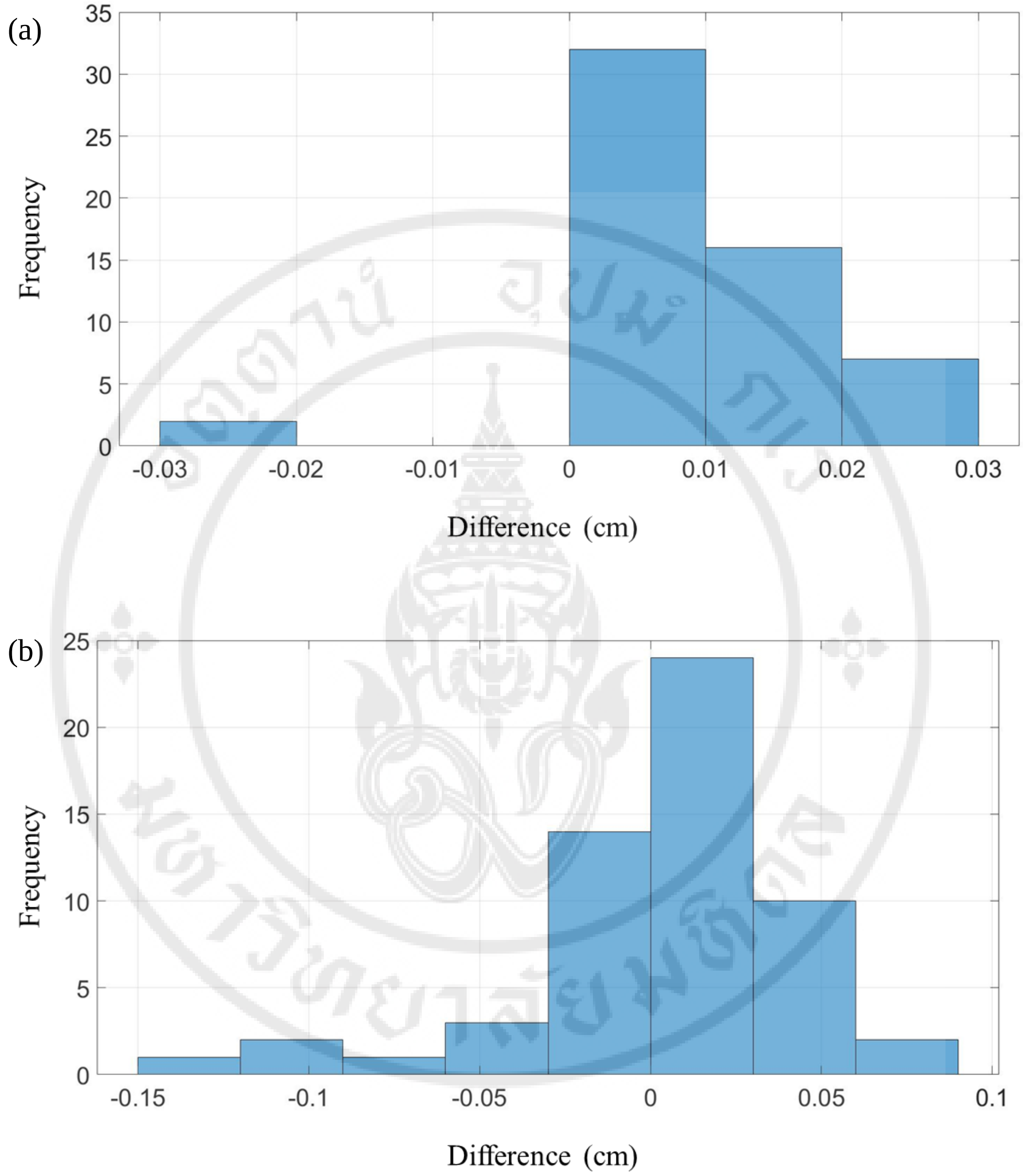

Figure 3B The overall difference distribution of capability test by adding blur in cine images of phantom move with amplitude 2.5 mm and time 0.5 second in (a) gantry angle 239º and (b) gantry angle 39º.

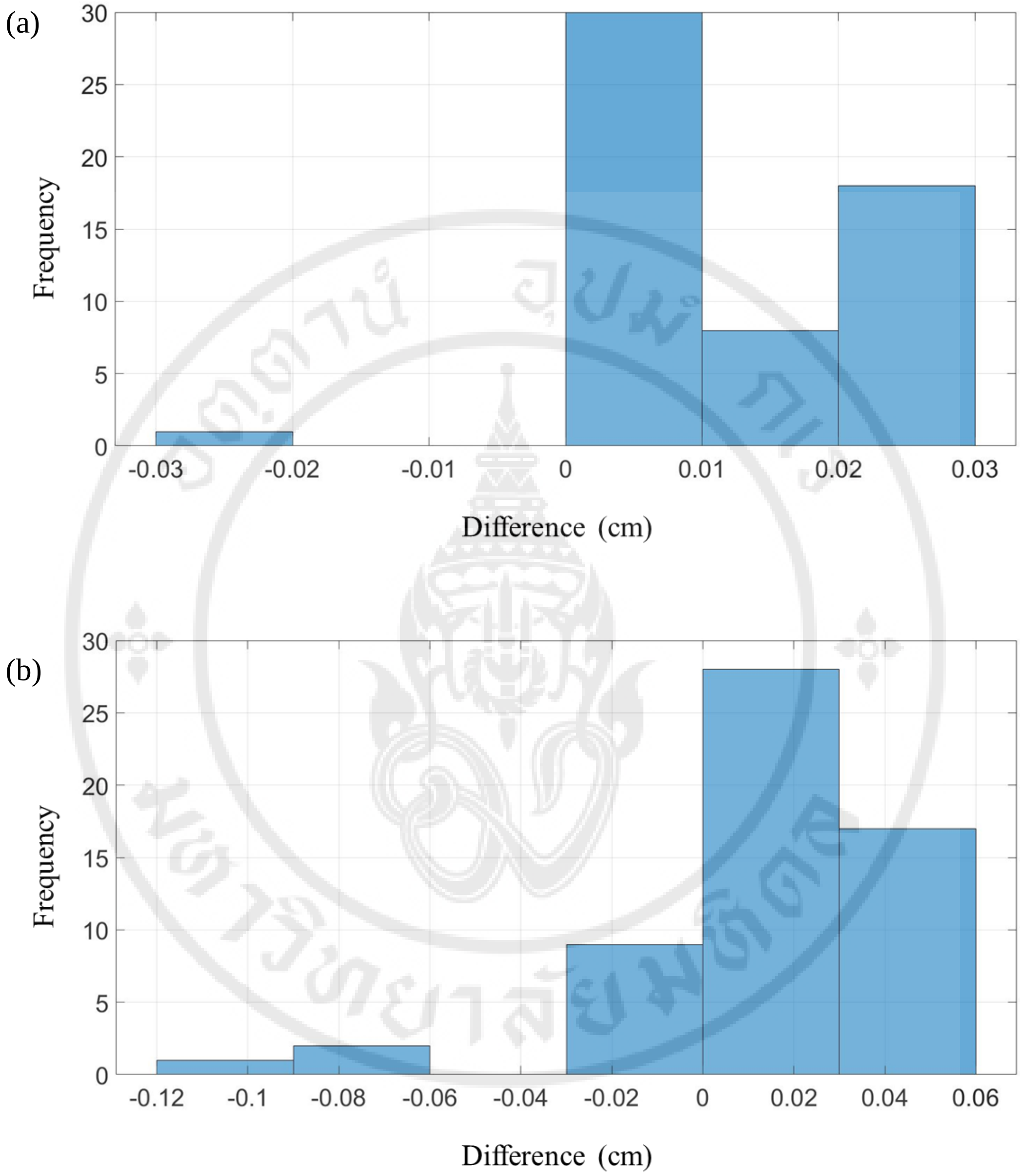

Figure 4B The overall difference distribution of capability test by adding blur in cine images of phantom move with amplitude 5 mm and time 1 second in (a) gantry angle 239º and (b) gantry angle 39º.

Scenario2: Simulated the noise images by adding Gaussian noise

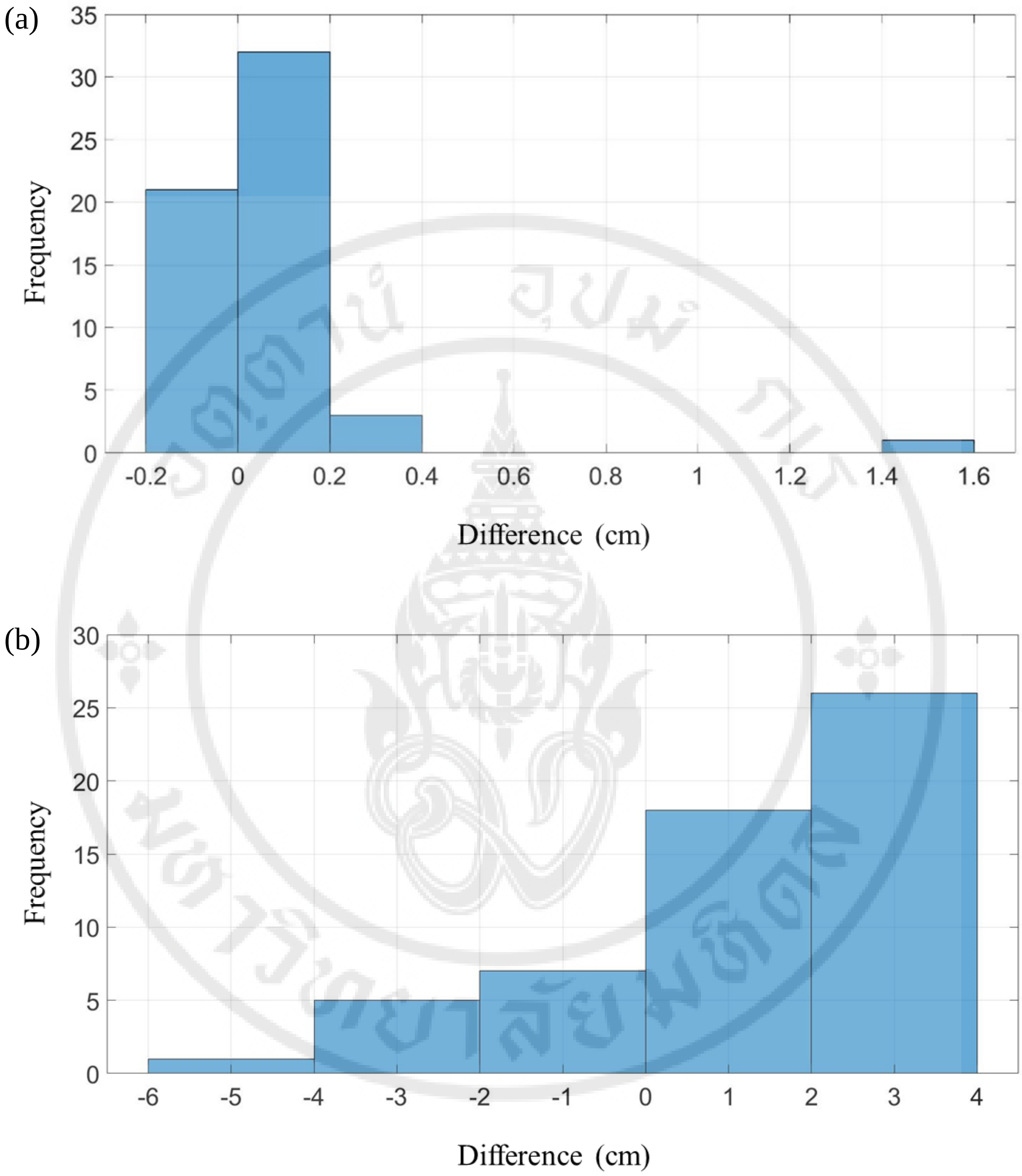

Figure 5B The overall difference distribution of capability test by adding Gaussian noise in cine images of phantom move with amplitude 0 mm and time 0 second in (a) gantry angle 239º and (b) gantry angle 39º.

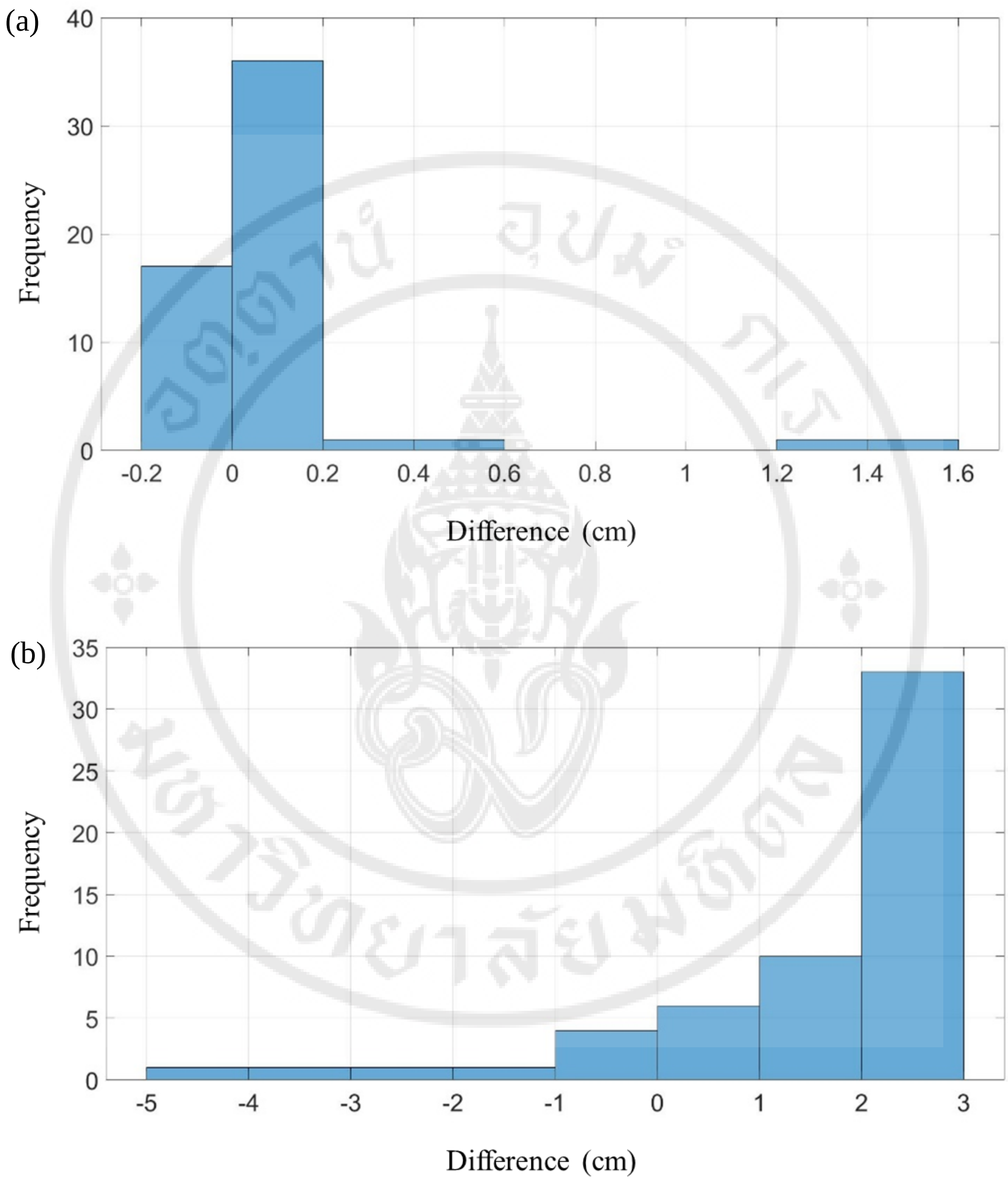

Figure 6B The overall difference distribution of capability test by adding Gaussian noise in cine images of phantom move with amplitude 2.5 mm and time 1 second in (a) gantry angle 239º and (b) gantry angle 39º.

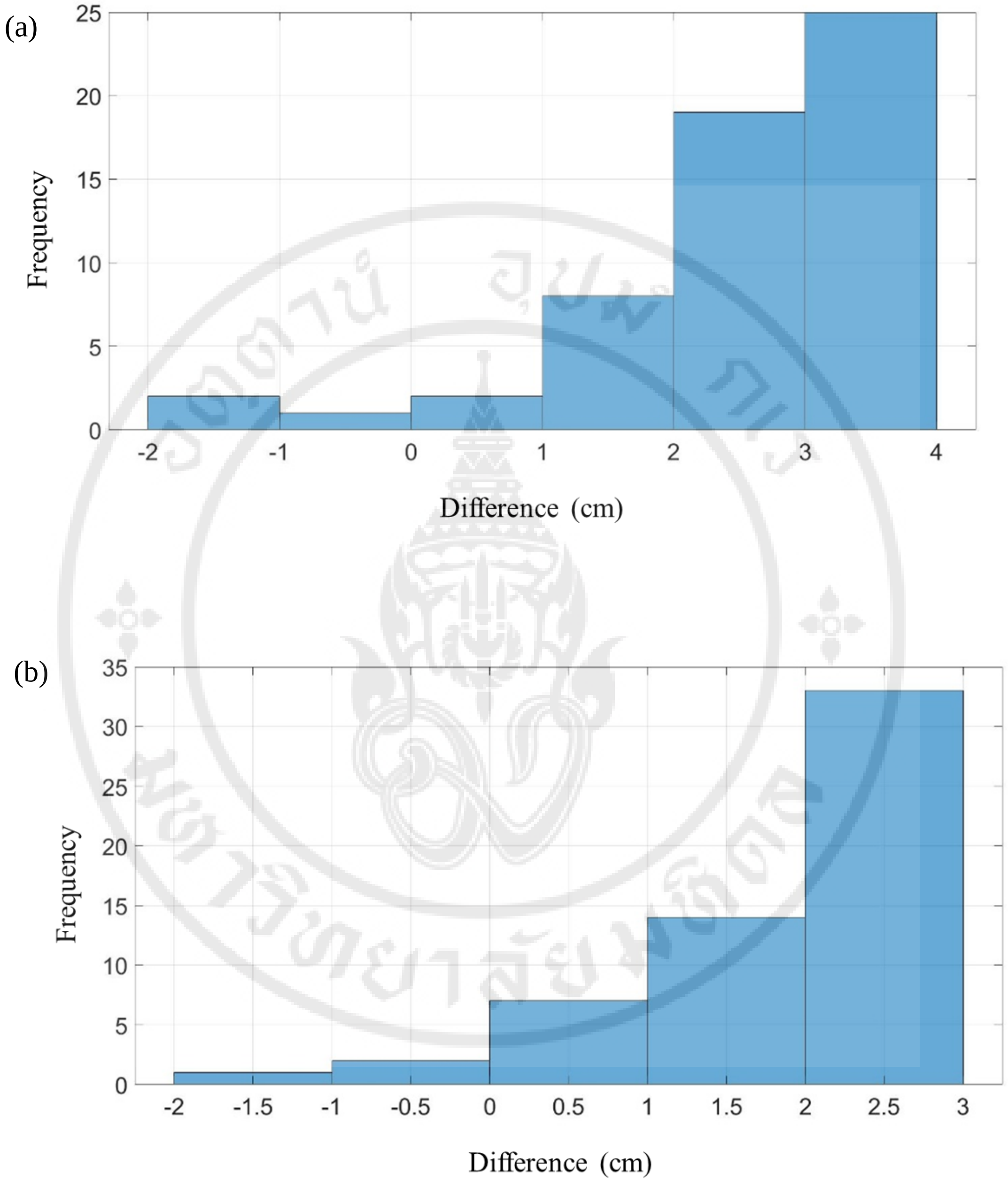

Figure 7B The overall difference distribution of capability test by adding Gaussian noise in cine images of phantom move with amplitude 2.5 mm and time 0.5 second in (a) gantry angle 239º and (b) gantry angle 39º.

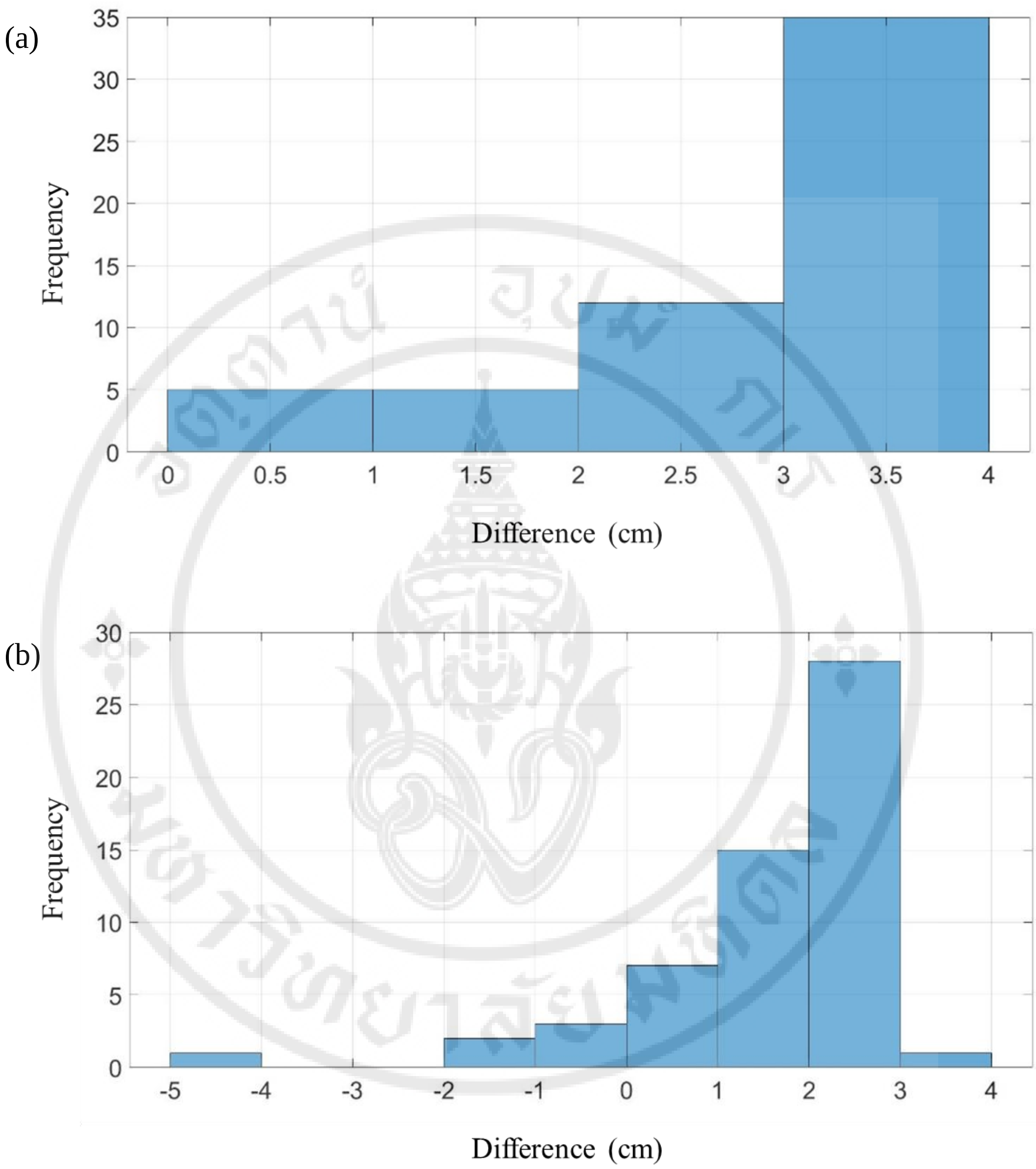

Figure 8B The overall difference distribution of capability test by adding Gaussian noise in cine images of phantom move with amplitude 5 mm and time 1 second in (a) gantry angle 239º and (b) gantry angle 39º.

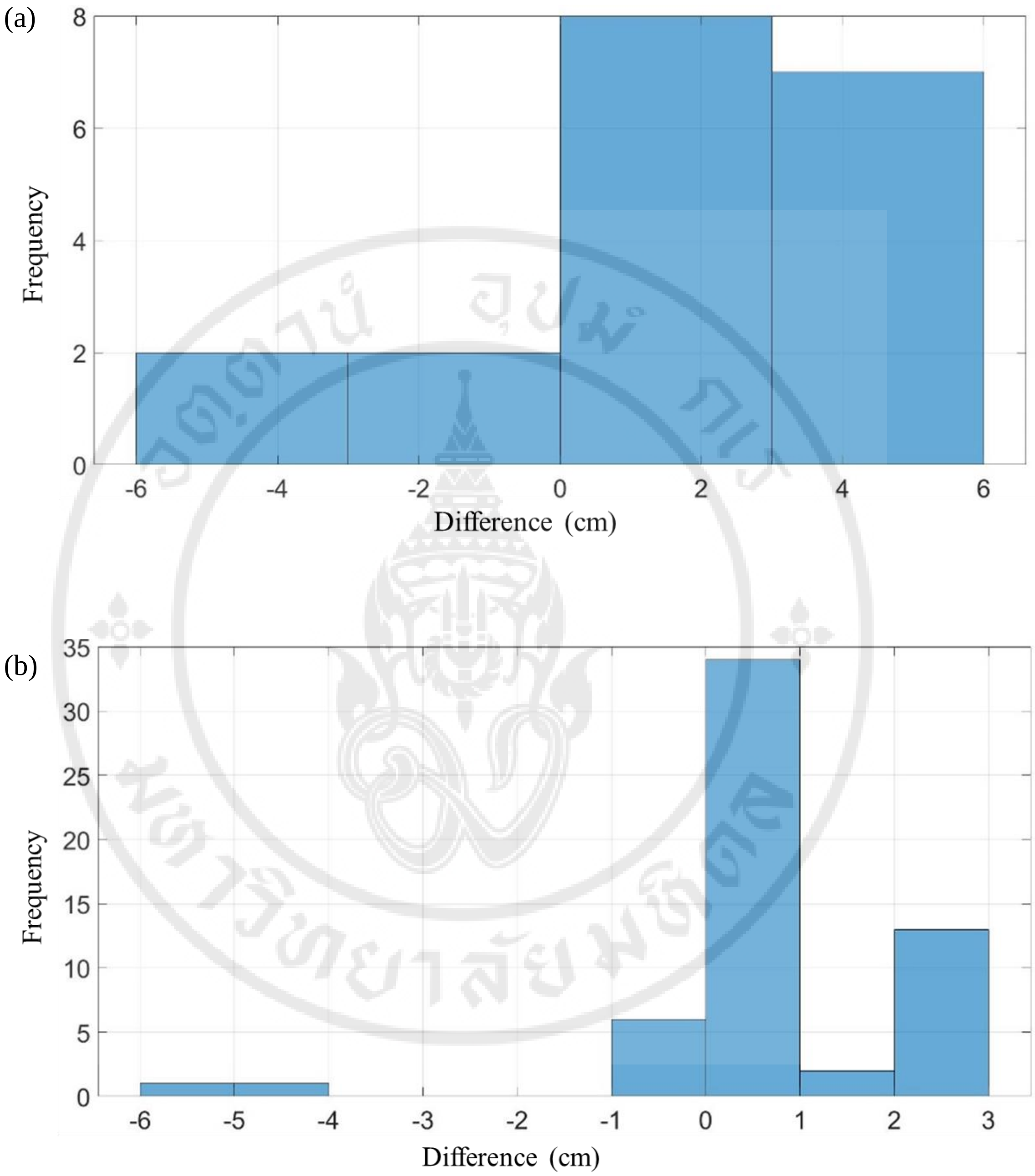

Figure 9B The overall difference distribution of capability test by adding salt and pepper noise in cine images of phantom move with amplitude 0 mm and time 0 second in (a) gantry angle 239º and (b) gantry angle 39º.

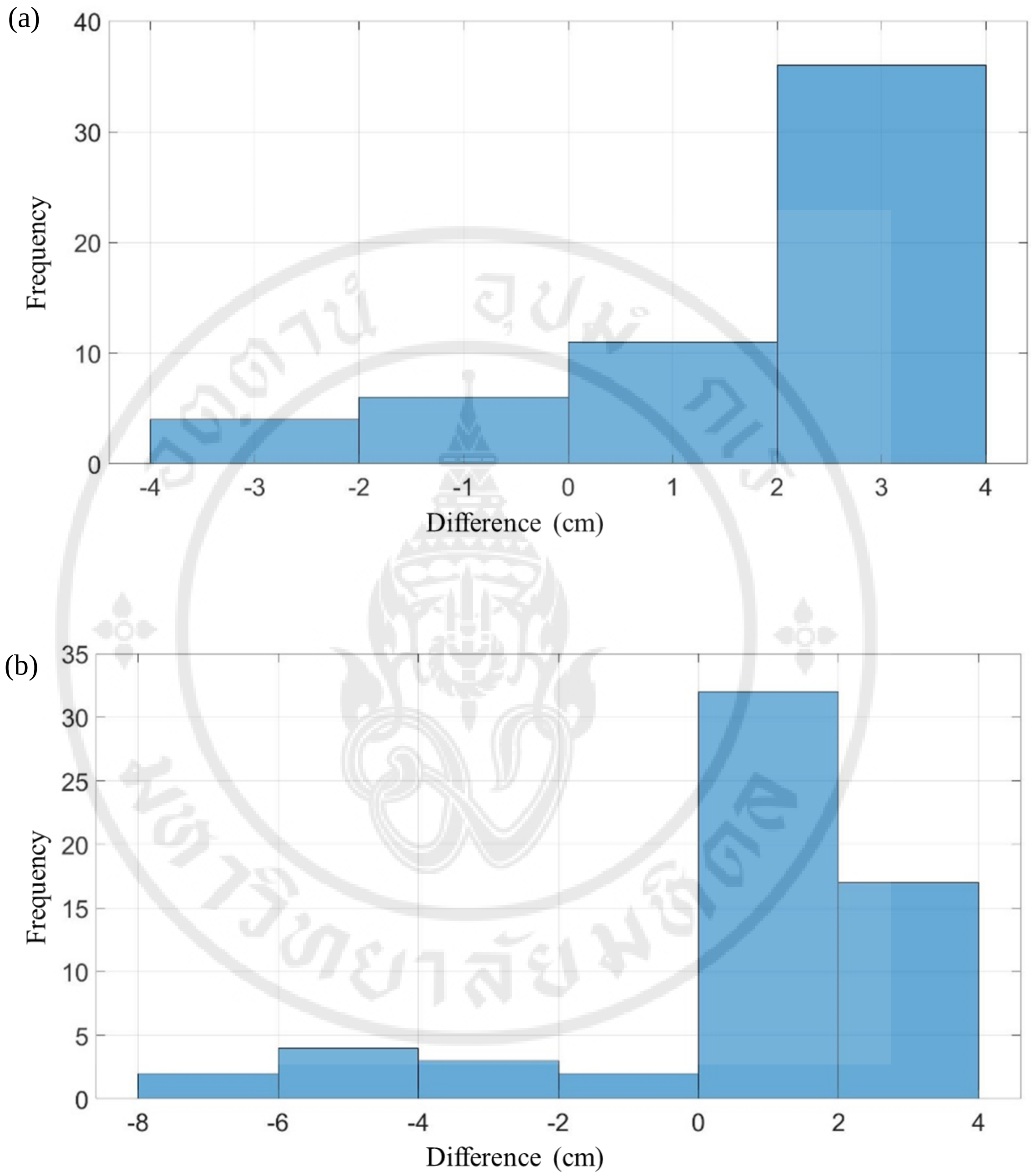

Figure 10B The overall difference distribution of capability test by adding salt and pepper noise in cine images of phantom move with amplitude 2.5 mm and time 1 second in (a) gantry angle 239º and (b) gantry angle 39º.

(a)

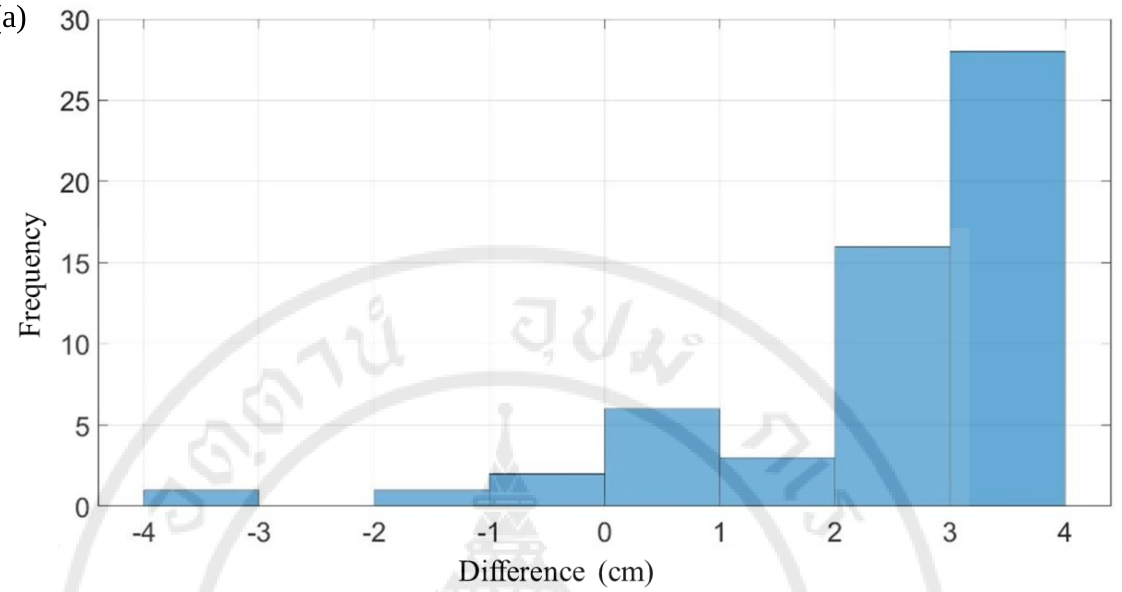

(b)

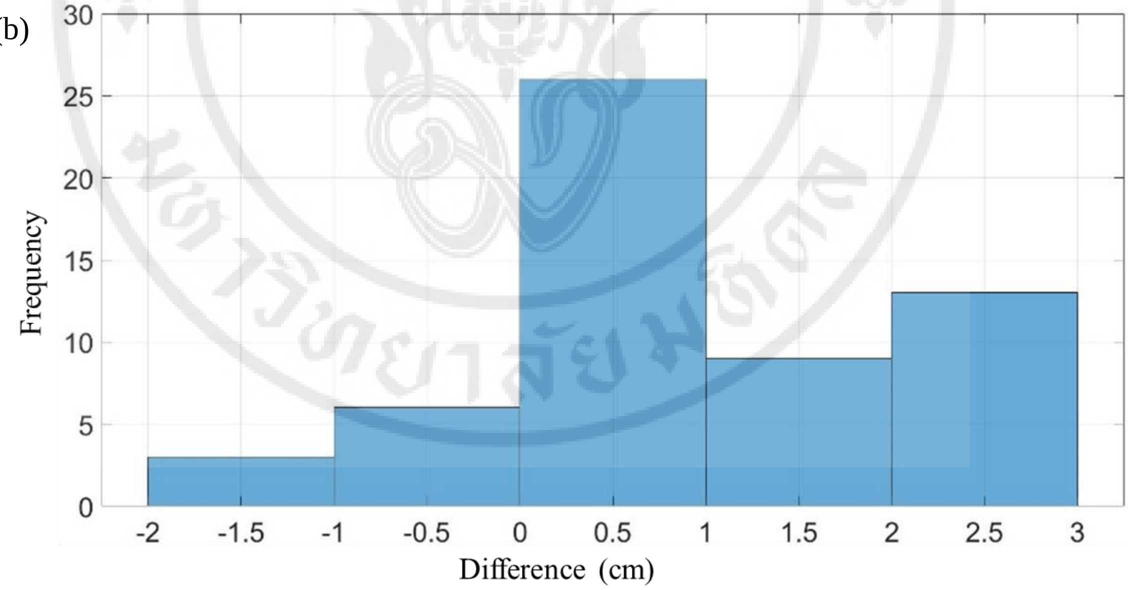

Figure 11B The overall difference distribution of capability test by adding salt and pepper noise in cine images of phantom move with amplitude 2.5 mm and time 0.5 second in (a) gantry angle 239º and (b) gantry angle 39º.

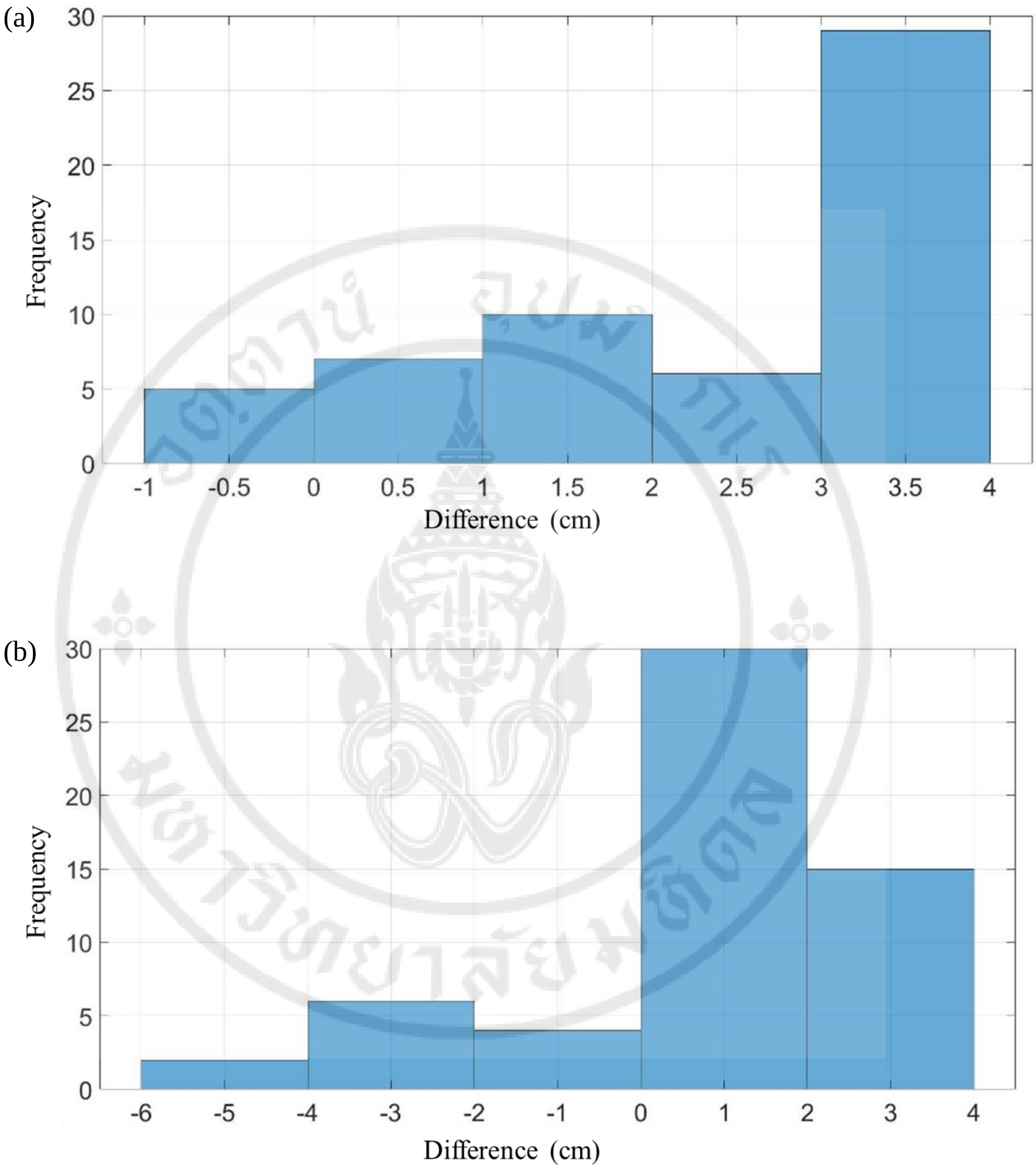

Figure 12B The overall difference distribution of capability test by adding salt and pepper noise in cine images of phantom move with amplitude 5 mm and time 1 second in (a) gantry angle 239º and (b) gantry angle 39º.

APPENDIX C

Applying in clinical

The cine images of the patient were analyzed in this study consist of 3 patients that have a different character, the data as show in Table 1C. The results show overall difference distribution in each patient as presented in Figure 1C – 3C.

Table 1C The characteristic of patient

Parameter	Age (year)	Treatment technique	Volume of PTV (cm^3)	Cine capture (fraction)
Patient 1	60	FIF	2071.7	5
Patient 2	53	FIF	449.2	4
Patient 3	48	FIF	883.8	1

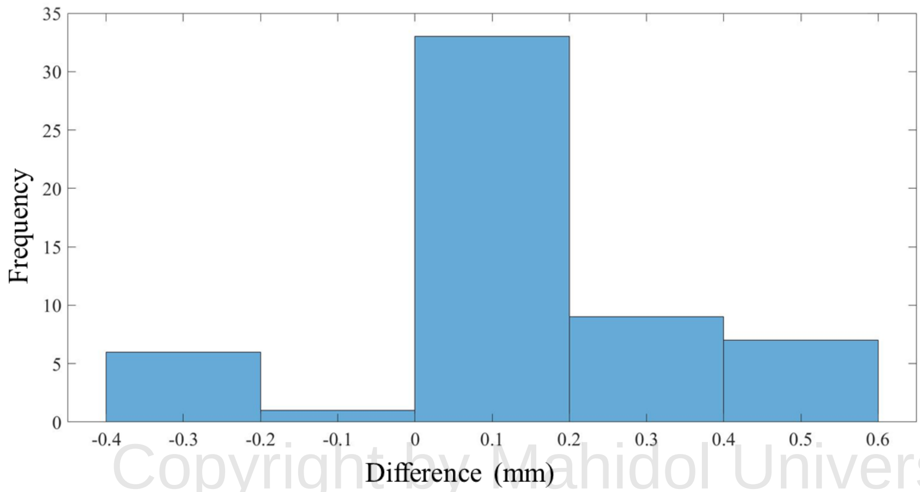

Figure 1C The overall difference distribution of patient 1.

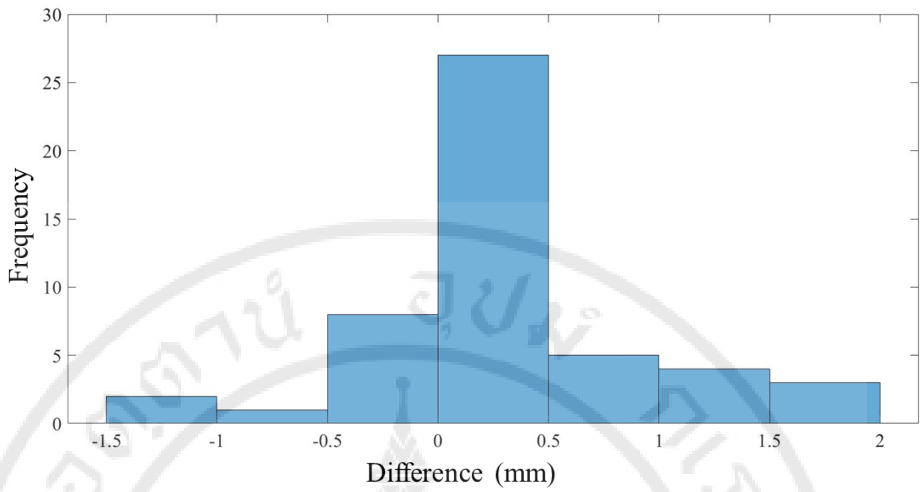

Figure 2C The overall difference distribution of patient 2.

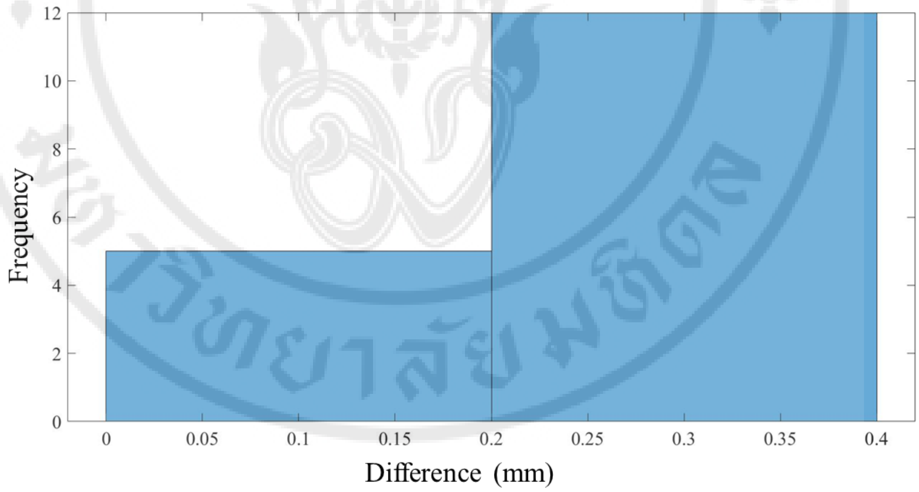

Figure 3C The overall difference distribution of patient 3.

BIOGRAPHY

NAME	Aphisara Deeharing
DATE OF BIRTH	January 30, 1992
PLACE OF BIRTH	Buriram, Thailand
INSTITUTIONS ATTENDED	Mahidol University, 2010-2013 Bachelor of Science (Radiological Technology)
HOME ADDRESS	1/30 Moo3 , Cherngnern, Muang, Rayong, Thailand 21000
EMPLOYMENT ADDRESS	906 Kamphaeng Phet 6 Rd, Talat Bang Khen, Lak Si, Bangkok 10210
PUBLICATION/PRESENTATION	The 28th Annual Thai Society of Radiological Technologists Conference at Lotus Pang Suan Keaw Hotel Chiang Mai, Thailand (15 – 17 January 2020)